



**AN INFRARED CAMERA SIMULATION FOR ESTIMATING
SPATIAL TEMPERATURE PROFILES AND SIGNAL-TO-NOISE
RATIOS OF AN AIRBORNE LASER-ILLUMINATED TARGET**

THESIS

David F. Orth

AFIT/GEO/ENP/07-01

**DEPARTMENT OF THE AIR FORCE
AIR UNIVERSITY**

AIR FORCE INSTITUTE OF TECHNOLOGY

Wright-Patterson Air Force Base, Ohio

APPROVED FOR PUBLIC RELEASE; DISTRIBUTION UNLIMITED.

The views expressed in this thesis are those of the author and do not reflect the official policy or position of the United States Air Force, Department of Defense, or the United States Government.

AFIT/GEO/ENP/07-01

AN INFRARED CAMERA SIMULATION FOR ESTIMATING SPATIAL
TEMPERATURE PROFILES AND SIGNAL-TO-NOISE RATIOS OF AN
AIRBORNE LASER-ILLUMINATED TARGET

THESIS

Presented to the Faculty
Department of Engineering Physics
Graduate School of Engineering and Management
Air Force Institute of Technology
Air University
Air Education and Training Command
In Partial Fulfillment of the Requirements for the
Degree of Master of Science in Electrical Engineering

David F. Orth, B.S.E.E.

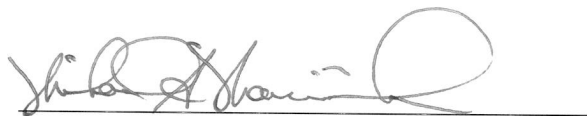
June 2007

APPROVED FOR PUBLIC RELEASE; DISTRIBUTION UNLIMITED.

INFRARED CAMERA SIMULATION FOR ESTIMATING
TEMPERATURES AND SIGNAL-TO-NOISE RATIOS OF AN AIRBORNE
LASER-IRRADIATED TARGET

David F. Orth, B.S.E.E.

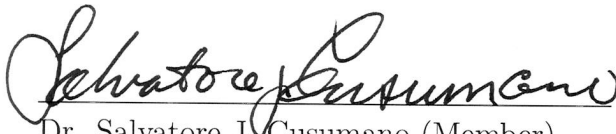
Approved:



Dr. Michael A. Marciniak (Chairman)

23 May 07

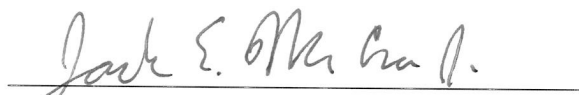
Date



Dr. Salvatore J. Cusumano (Member)

23 May 07

Date



Col. Jack McCrae Ph.D (Member)

23 May 07

Date

Abstract

As the Airborne Laser (ABL) becomes an operational weapon system, the ability to measure the system's energy-delivering capability in an operational testing scenario is necessary. An effort is currently underway between the Air Force Institute of Technology and Directed Energy Test and Evaluation Capability office to explore the requirements for a measurement system that will remotely observe a target's high-energy laser-induced thermal emission. The desired result of this exploration will be a method by which the ABL's performance can be measured and evaluated. The presented research aids that effort by: 1) developing a spectrally-based infrared camera simulation to explore how the target surface's specular and diffuse reflectivities affect the observed signal-to-noise ratio (SNR) and 2) estimate of the target's temperature in the laser spot. This simulation provides for the observed irradiance, scaled by atmospheric absorption, to consist of the target's self-emission, the target's reflected background emission, and the path emission from the observer to the target. The observed irradiance is scaled and distributed onto a focal plane array (FPA) by way of a simulated optical system. The effects induced by the optical system parameters, including aperture size, focal length, detector pixel size, and detector sampling, are described by modulation transfer functions. Based on the photovoltaic detector's quantum efficiency, the observed irradiance will be converted to a current signal. As for detector noise quantities, values computed in the simulation include photon noise, dark current noise, and other noise contributions inherent to FPA technology. Using the simulation, a study is conducted to investigate the effects that detector integration time and waveband choice has on the observed SNR as the target's specular and diffuse reflectivities are independently varied. Additionally, a least-squares optimization is evaluated for estimating the temperature within the laser spot using the simulation data computed in two different wavebands. The results of this study show

that the observed SNR is strongly dependent upon the target's specular and diffuse reflectivities, but the hottest parts of the laser-induced thermal emission will be very detectable in the mid-wave infrared band (*i.e.*, 3.4-4.2 μm) for total reflectivities up to 0.9 with the additional advantage of small background contributions. In the long-wave infrared band (*i.e.*, 8.5-12 μm), the thermal emission is also very detectable, but a significant background contribution comes from earthshine. Based on the study results, the mid-wave infrared band is the best choice for observing the laser-induced thermal emission. The choice of a 0.125- or 1-msec integration time had little effect on the overall results. As for estimating temperature in the laser spot, the least-squares method proved unsuccessful in estimating temperature. The main source of error in the temperature estimation was the optical system's point spread function since it controls how optical energy is distributed onto the image plane via diffraction.

Acknowledgements

First and foremost, I must express my sincerest thanks to my committee for making this thesis the best experience of my AFIT education. I have learned so much through this process that I am particularly indebted to Dr. Marciniak for all his support, time, and guidance given to me as I worked on this thesis. I feel incredibly fortunate to have him as my thesis advisor. I must say thank you to Dr. Cusumano for allowing my thesis work tie into DIAT development and for his time spend on my committee. I also sincerely appreciate the time given by Col McCrae to sit on my committee and evaluate my work.

As for fellow DIAT team members, I must thank Lt Col Fiorino, Dr. Bailey, Becky Beauchamp, and Paul Mattie for supplying my thesis research with critical data. Finally, I would like to thank Brian Birkmire for his time in helping me generate data for my thesis study, which required many executions of my simulation.

Once again, thank you everyone!

David F. Orth

Table of Contents

	Page
Abstract	iv
Acknowledgements	vi
List of Figures	x
List of Tables	xiv
List of Abbreviations	xvi
I. Introduction	1
1.1 Measuring High-Energy Laser Performance	1
1.2 Problem Definition	3
1.3 Previous Research and Development	4
1.4 Thesis Overview	5
II. Background Theory	7
2.1 Basic Radiometry	7
2.1.1 Definition of Terms	7
2.1.2 Blackbody Radiation	10
2.1.3 Emissivity	12
2.1.4 Radiometric Measures of Temperature	13
2.2 Infrared Optical System	15
2.2.1 Transmission Functions (Atmospheric, Optical, and Spectral Filter)	15
2.2.2 Modulation Transfer Functions	18
2.2.3 Detector Response	24
2.3 Summary	28

	Page
III. Model Development	29
3.1 Modeling Methodology	29
3.1.1 Spectral Model	29
3.1.2 Scaling in the Object, Aperture, and Image Planes	29
3.2 Modeling the Radiometry	32
3.2.1 Radiometric Assumptions	33
3.2.2 Temperature Distribution	34
3.2.3 Self-Emission	36
3.2.4 Path Radiance	38
3.2.5 Specular Background Reflection	39
3.2.6 Diffuse Background Reflection	41
3.2.7 Total Spectral Irradiance at the Image Plane	43
3.3 Modeling the Modulation Transfer Functions	43
3.3.1 Optical MTF	43
3.3.2 Detector MTF	45
3.3.3 Sampling MTF	47
3.3.4 Atmospheric MTF	48
3.3.5 System MTF	49
3.4 Modeling the Detector Response	49
3.4.1 Computing the Detector Signal	50
3.4.2 Detector Materials	53
3.4.3 Noise Sources	55
3.5 Summary	59
IV. Temperature and SNR Analyses	60
4.1 Analysis Scenario and Simulation Parameter Definitions	60
4.2 SNR Data	67
4.2.1 SNR Discussion	76
4.3 Temperature Estimation Via Least Square Optimization	79
4.3.1 Ideal Radiometric Case	80
4.3.2 Estimation Using Simulation Data	81
4.3.3 Temperature Estimation Discussion	85
4.4 Summary	93

	Page
V. Conclusions and Recommendations	95
5.1 Major Contributions	95
5.2 Recommendations for Future Research	96
5.3 Conclusion	97
Appendix A. Lambertian Source/Fractional Specularity Justification . . .	99
Bibliography	110

List of Figures

Figure		Page
2.1.	Ideal blackbody curves at various temperatures.	11
2.2.	Example atmospheric transmission profile for a 1-km path length. . .	16
2.3.	Absorbing molecules that affect the atmospheric transmission in the IR spectrum.	17
2.4.	Diffraction-limited Airy disk pattern produced by a circular pupil. . .	19
2.5.	Generalized definition of a spatial-domain irradiance distribution. . .	20
2.6.	Modulation transfer function effects on the modulation depth as spatial frequency increases.	21
2.7.	Characteristic current-voltage curve for a photodiode.	26
2.8.	Quantum efficiency for InSb at 300K.	27
3.1.	Reflectance data for the bare aluminum surface.	35
3.2.	HEL-induced missile body temperatures.	35
3.3.	A comparison showing little difference between observer-to-target and observer-to- ∞ path radiances.	39
3.4.	Geometry defining the radiance contribution from the reflected specular background.	40
3.5.	Geometry defining the diffuse-background spectral-irradiance com- putation.	42
3.6.	Optical MTFs for various IR wavelengths.	45
3.7.	At the detector spatial cutoff frequency $f_X = 1/w$, the modulation depth is zero.	46
3.8.	MTF of a 25- μm FPA pixel.	47
3.9.	Demonstration of the shift variance of a sampled, image-forming system.	48
3.10.	Overall system MTF of imaging system.	50
3.11.	Photon flux distribution across the MCT FPA showing pixel bound- aries in the 8.5-to-12- μm waveband, 0.125 msec integration time. . .	51

Figure	Page
3.12. Spatially-integrated photon flux incident on each MCT FPA pixel in the 8.5-to-12- μm waveband, 0.125 msec integration time.	52
3.13. Quantum efficiency of $\text{Hg}_{0.2}\text{Cd}_{0.8}\text{Te}$ at 80 K with a measured cutoff wavelength, λ_c , of 13.78 μm	54
3.14. Quantum efficiency of InSb at 77 K with a cutoff wavelength, λ_c , of 5.5 μm	55
3.15. Plots of RA products for various β -valued $\text{Hg}_{1-\beta}\text{Cd}_\beta\text{Te}$ detectors. . .	58
4.1. Atmospheric transmission function defined for a 15.8-km slant range at Vandenberg AFB on July 14, 2007 at 12:00 local time.	61
4.2. Observer-to-target and observer-to-infinity spectral path radiances used to provide background sources.	62
4.3. Spectral radiance incident onto target body as seen from the specular angle, 28.4 degrees from zenith, with a path from the target to infinity.	64
4.4. Spectral radiances incident onto target body used to compute the diffuse reflected background as seen from angles 0, 45, 90, 135, and 180 degrees from zenith, with a path from the target to infinity. . . .	64
4.5. Diffuse spectral irradiance incident on the missile body.	68
4.6. Computed SNR from a 256×256 InSb FPA in the 3.4-4.2 μm waveband: Integration Time: 0.125 msec, $\rho_{spec} = 0.2$, $\rho_{diff} = 0.5$. Optic: $D_{opt} = 0.6$ m, $F\# = 10$	70
4.7. Computed SNR from a 256×256 MCT FPA in the 8.5-12 μm waveband: Integration Time: 0.125 msec, $\rho_{spec} = 0.2$, $\rho_{diff} = 0.5$. Optic: $D_{opt} = 0.6$ m, $F\# = 10$	70
4.8. Image of estimated variable space showing where the least square is located: $T_{eff} = 567$ K and $\epsilon' = 0.74$	82
4.9. How the estimation residual varied in terms of temperature and emissivity separately.	82
4.10. Spectral radiance contributions in the 3.4-to-4.2- μm waveband; atmospheric transmission is included.	83
4.11. Spectral radiance contributions in the 8.5-to-12- μm waveband; atmospheric transmission is included.	83

Figure	Page
4.12. Estimated temperature profiles for various specular and diffuse reflectivities along the axis of the missile, 0.125 msec integration time.	84
4.13. Estimated emissivity profiles for various specular and diffuse reflectivities along the axis of the missile, 0.125 msec integration time. . . .	84
4.14. Apparent temperatures using an ideal blackbody estimator for the 3.4-4.2- μm band, 8.5-12- μm , and the two-band cases.	86
4.15. Apparent temperatures using an ideal blackbody estimator scaled by $\tau_{atm}(\lambda)$ for the 3.4-4.2- μm band, 8.5-12- μm , and the two-band cases.	88
4.16. Apparent temperatures using an ideal blackbody estimator scaled by $\tau_{atm}(\lambda)$ and incorporating path radiance for the 3.4-4.2- μm band, 8.5-12- μm , and the two-band cases.	89
4.17. Photon flux incident on the InSb FPA in the 3.4-to-4.2- μm waveband, 0.125-msec integration time. Simulated source reflectivities: $\rho_{spec} = 0.2$, $\rho_{diff} = 0.3$	90
4.18. Number of electrons generated (atmospheric MTF included) in the MCT FPA in the 8.5-to-12- μm waveband, 0.125-msec integration time.	92
4.19. Number of electrons generated (atmospheric MTF not included) in the MCT FPA in the 8.5-to-12- μm waveband, 0.125 msec integration time.	92
4.20. Ideal image of temperature distribution which shows the average temperature within each projected pixel of the FPA.	93
A.1. Directional emissivity for an ideal blackbody (<i>i.e.</i> , $\varepsilon(\lambda) = 1$) with θ_r varying from zero to $\frac{\pi}{2}$ and b varying from zero to one.	100
A.2. Angular dependence of the total reflectance for three values of b . . .	101
A.3. Diffuse BRDF as a function of incident elevation angle, θ_i , and reflected elevation angle, θ_r , for $b = 0.05$ and $\rho_{diff}(\lambda) = 1$).	102
A.4. Diffuse reflectivity as a function of incident elevation angle, θ_i	102
A.5. Total BRDF of bare Al on a Cartesian plot. Sandford-Robertson parameters: $\varepsilon(\lambda) = 0.11$, $\rho_{diff}(\lambda) = 0.02$, $b = 0.05$, and $e = 0.0042$. .	105
A.6. Total BRDF of bare Al on a spherical plot. Sandford-Robertson parameters: $\varepsilon(\lambda) = 0.11$, $\rho_{diff}(\lambda) = 0.02$, $b = 0.05$, and $e = 0.0042$. .	105

Figure		Page
A.7.	Total BRDF of bare Al as a function of position on missile body at the 61.6-degree observation angle.	106
A.8.	Directional emissivity as a function of position on the missile body for bare Al.	107
A.9.	Directional diffuse reflectivity as a function of position on the mis- sile body for bare Al.	107
A.10.	Directional specular reflectivity as a function of position on the missile body for bare Al.	108

List of Tables

Table		Page
2.1.	Radiometric quantities and their units.	7
3.1.	Simulation sampling size considerations for different object plane spacings.	32
4.1	IR camera simulation inputs with their corresponding units, symbols, and default values.	65
4.2.	IR camera simulation outputs with their corresponding units.	69
4.3	Computed SNR for hottest pixel (129,129) using a 256×256 InSb FPA in the 3.4-4.2 μm waveband, Integration Time: 1 msec. Optic: $D_{opt} = 0.6$ m, $F\# = 10$	71
4.4	Computed SNR for hottest pixel (129,129) using a 256×256 InSb FPA in the 3.4-4.2 μm waveband, Integration Time: 0.125 msec. Optic: $D_{opt} = 0.6$ m, $F\# = 10$	71
4.5	Computed SNR for hottest pixel (129,129) using a 256×256 MCT FPA in the 8.5-12 μm waveband, Integration Time: 1 msec. Optic: $D_{opt} = 0.6$ m, $F\# = 10$	72
4.6	Computed SNR for hottest pixel (129,129) using a 256×256 MCT FPA in the 8.5-12 μm waveband, Integration Time: 0.125 msec. Optic: $D_{opt} = 0.6$ m, $F\# = 10$	72
4.7	Computed SNR for missile body pixel (92,129) using a 256×256 InSb FPA in the 3.4-4.2 μm waveband, Integration Time: 1 msec. Optic: $D_{opt} = 0.6$ m, $F\# = 10$	73
4.8	Computed SNR for missile body pixel (92,129) using a 256×256 InSb FPA in the 3.4-4.2 μm waveband, Integration Time: 0.125 msec. Optic: $D_{opt} = 0.6$ m, $F\# = 10$	73
4.9	Computed SNR for missile body pixel (92,129) using a 256×256 MCT FPA in the 8.5-12 μm waveband, Integration Time: 1 msec. Optic: $D_{opt} = 0.6$ m, $F\# = 10$	74
4.10	Computed SNR for missile body pixel (92,129) using a 256×256 MCT FPA in the 8.5-12 μm waveband, Integration Time: 0.125 msec. Optic: $D_{opt} = 0.6$ m, $F\# = 10$	74

Table		Page
4.11	Computed SNR for background pixel (92,92) using a 256×256 InSb FPA in the 3.4-4.2 μm waveband, Integration Time: 1 msec. Optic: $D_{opt} = 0.6$ m, $F\# = 10$	75
4.12	Computed SNR for background pixel (92,92) using a 256×256 InSb FPA in the 3.4-4.2 μm waveband, Integration Time: 0.125 msec. Optic: $D_{opt} = 0.6$ m, $F\# = 10$	75
4.13	Computed SNR for background pixel (92,92) using a 256×256 MCT FPA in the 8.5-12 μm waveband, Integration Time: 1 msec. Optic: $D_{opt} = 0.6$ m, $F\# = 10$	76
4.14	Computed SNR for background pixel (92,92) using a 256×256 MCT FPA in the 8.5-12 μm waveband, Integration Time: 0.125 msec. Optic: $D_{opt} = 0.6$ m, $F\# = 10$	76
4.15	Noise contributions in the InSb and MCT FPAs for integration times of 0.125 msec and 1 msec while observing a target with reflectivities of $\rho_{spec} = 0.2$ and $\rho_{diff} = 0.3$	78

List of Abbreviations

Abbreviation	Page
ABL	1
HEL	1
AFIT	1
DETEC	1
DIAT	1
IR	3
FPA	3
ROIC	3
SNR	4
MTF	7
FOV	8
PLEXUS	16
MODTRAN	17
OTF	20
PSF	23
I-V	26
InSb	27
BRDF	33
IFOV	46
HgCdTe	47
MCT	47
RA	57
CCD	57
CTE	57
MOSFET	59
LCAIR	97

AN INFRARED CAMERA SIMULATION FOR ESTIMATING SPATIAL TEMPERATURE PROFILES AND SIGNAL-TO-NOISE RATIOS OF AN AIRBORNE LASER-ILLUMINATED TARGET

I. Introduction

1.1 *Measuring High-Energy Laser Performance*

As the U.S. Air Force's Airborne Laser (ABL) program progresses toward the operational testing and evaluation phase, three fundamental questions arise concerning the testing of this weapon system.

- Is the ABL's high-energy laser (HEL) delivering the expected irradiance on the target?
- How can the expected irradiance be measured and verified?
- What testing instrumentation requirements must be specified in order to ensure accurate irradiance measurement?

Currently, the Air Force Institute of Technology (AFIT) is working with the Directed Energy Test and Evaluation Capability (DETEC) office to develop the Delivered Irradiance Analysis Tool (DIAT). This tool will provide a simulation and algorithm that will answer the above questions. But in order to attain accurate measurements, the development of DIAT must take into account factors dictated by the mission requirements of the test scenario that will complicate the irradiance measurement. These requirements and their associated effects on the measurement are as follows [4]:

1. Engagement geometry: This factor requires the irradiance measuring system to be positioned such that it observes and resolves the HEL strikepoint on the target.

2. Remote irradiance measurement: This factor insists that the measurement be non-invasive, which means that the target cannot be modified with sensors and associated equipment for direct measurement. Additionally, this mission requirement dictates a high degree of safety during testing.
3. High resolution imagery: This factor requires the optical system to be of sufficient performance such that the collected data produces an accurate irradiance result when it is put through the DIAT algorithm.
4. Uncertain parameters: This factor takes into account test parameters that may have high degrees of variability and are incapable of being controlled. These variabilities add to the uncertainty in the irradiance measurement. These variabilities may include transient temperature effects from the HEL heating the target and positional effects due the engagement geometry.

To incorporate these requirements, the simulation must describe the three main components that make up the entire engagement scenario. The first component is the ABL propagating laser energy through a turbulent atmosphere to the target. In the second component, the laser energy interacts with the target to produce two observable effects: an induced temperature distribution and reflected laser energy. The final component takes these two effects and treats them as sources for a remote observer to collect and measure their radiation. All three components are spatially defined by the engagement geometry.

The capabilities that are expected of DIAT [4] include:

1. Accurately convert reflected in-band and thermally-emitted target imagery into incident HEL irradiance on the target to support ABL engagement analysis.
2. Determine the accuracy achievable in the irradiance calculations for a given observer-to-target geometry, which includes the distance to target, observation angle with respect to the target, the target's orientation, and predefined spectral, spatial and temporal resolutions.

3. Determine the performance required of practical instrumentation in terms of spatial, spectral and temporal resolution, while operating with sensor platform jitter and atmospheric turbulence, to achieve the two previous capabilities.

1.2 Problem Definition

Given DIAT's immense scope and requirements, this thesis focuses on the remote observer and explores the requirements for a measurement system that will observe the target's laser-induced thermal emission. To begin this exploration, a spectral infrared (IR) camera simulation is developed that meets the requirements and expectations listed in the previous section. Three aspects of the simulation must be addressed in order to meet these expectations and to provide an accurate and robust simulation. First, all possible radiation sources must be accounted and modeled to produce an accurate signal. These sources include the target's self emission, reflected-background emission, and the observer-to-target atmospheric path emission. The second aspect involves the optical system and its effects on the collected irradiance; consequently, the simulation must model the blurring effects of the optics and a focal plane array (FPA) which samples the collected image. Lastly, the third aspect is the FPA detector material, which will convert the incident irradiance via the detector's quantum efficiency into an electronic signal. However, knowing the signal is not enough; the simulation must account for noise quantities inherent to photovoltaic detector technology and FPA read-out integrated circuitry (ROIC), which will mute the perceived signal strength.

All of the simulation's aspects have parameters associated with them that will affect how the irradiance is measured. With a completed IR camera simulation, a parametric study can begin to see how these measurement system parameters affect the measured irradiance. For this thesis, the initial parametric study will investigate the effects of three parameters: the target's reflectance, the detector's integration time, and the choice of waveband to collect IR radiation. However, a more significant contribution can be made from this initial study. The IR camera simulation can

help devise the methodology by which metrics are identified to quantify the ABL’s performance. The metric that this thesis attempts to ascertain is the accuracy to which temperatures in the target’s laser-induced hot spot can be estimated using two hot-spot thermal bands.

From this overall study, many fundamental questions concerning the test instrumentation can be answered:

- How will the target’s reflectivity affect the measured irradiance?
- What kind of signal-to-noise ratios (SNR) can be expected for different target reflectivity values?
- What waveband is the best choice for the irradiance measurement?
- Can the HEL-induced hot-spot temperatures be estimated?
- What factors contribute to the estimated temperature’s uncertainty?

1.3 Previous Research and Development

In researching the numerous topics associated with this thesis, a previous AFIT thesis titled, “Radiometric Analysis of Daytime Satellite Detection,” by Lilevjen provides the primary basis for this research [15]. Even though her model application is quite different from this thesis, she developed a simple “end-to-end” radiometric model that accounted for a source, the sun in her case, illuminating a planar, diffuse “satellite” whose reflected radiance would then be collected by an optic and ultimately a single-pixel detector [15:21]. She also incorporated many factors that attenuate the collected irradiance such as atmospheric transmission, optical transmission, and spectral filter transmission. For her computation of SNR, she incorporated the effects that an InGaAs photovoltaic detector have in producing the signal along with the photon, Johnson, and shot noises associated with photovoltaic technology [15:37].

Overall, Lilevjen’s model is a complete radiometric simulation for her scenario of observing satellites, but the question arises, “Does the model have sufficient fidelity

to simulate a DIAT scenario?” The answer is no; Lilevjen’s model is too simplistic to be useful for DIAT because of three assumptions made in her thesis. First, the assumption of planar satellite geometry [15:20] significantly reduces model fidelity since it removes the inherent ability of realistic geometry to redirect radiation accordingly. For a simulation to have credibility in its predictions, representative target geometries should always be modeled. For instance, the geometry that this thesis must incorporate is the cylindrical shape of the missile body. Second, Lilevjen’s model does not account for all possible sources for an observed signal. She is only looking at reflected and background radiation while ignoring the satellite’s self-emission contribution [15:21]. Given the desired fidelity for DIAT, this thesis must account all possible radiation sources. Last, Lilevjen treats the optical system simply as a light-gathering tool for a single detector in the creation of her signal. This assumption completely disregards the fact that the optical system is really an image-forming system which has its own ability to distribute optical radiation onto an image plane according to diffraction theory. This image will have spatial variations in the collected optical radiation. Using an FPA enables the detection of these spatial variations; while, a single-element detector ignores them. Also, the number of noise sources in a realistic system is more than the three Lilevjen assumed for photovoltaic detectors. This thesis incorporates the noise effects of the photovoltaic detector along with those from the ROIC.

1.4 Thesis Overview

This thesis is organized as follows:

- *Chapter I*: Provides an introduction to and motivation of the problem and details what this thesis attempts to accomplish.
- *Chapter II*: Reviews the necessary theoretical concepts that are used to develop the IR camera simulation.

- *Chapter III*: Discusses and details the implementation of the complete IR camera simulation and all its parameters.
- *Chapter IV*: Presents and analyzes the results of the parametric study and temperature estimation which were generated by the IR camera simulation.
- *Chapter V*: Provides conclusions to the analyses and recommends areas of continued research for the IR camera simulation.

II. Background Theory

This chapter provides the foundational theory that is the basis for the IR camera simulation. This theoretical discussion explores the three main areas which make up this IR camera simulation: the fundamentals of radiometry, which determine the amount of IR radiation emitted by a source and ultimately collected by an optic and detector; the modulation transfer function (MTF), which provides the means of simulating the effects of the optical system distributing the radiation onto the image plane; and the detector performance, which provides the means of detecting and measuring the amount of IR radiation.

2.1 Basic Radiometry

To understand how the HEL-induced hot spot on the missile can be observed and measured, an understanding of radiometry is required. The first step is to define the terms used in radiometry.

2.1.1 Definition of Terms. Radiometric quantities can be defined either in terms of energy units or photon units. Table 2.1 displays radiometric quantities and their associated units. As a means of differentiating between quantities, the energy-based units are subscripted with e ; the photon-based units are subscripted with q .

Table 2.1: Radiometric quantities and their units.

Quantity	Energy Units		Photon Units	
	Symbol	Units	Symbol	Units
Flux	ϕ_e	Watts	ϕ_q	photons/s
Intensity	I_e	Watts/sr	I_q	photons/($s \cdot sr$)
Irradiance	E_e	Watts/ cm^2	E_q	photons/ $cm^2 \cdot s$
Exitance	M_e	Watts/ cm^2	M_q	photons/ $cm^2 \cdot s$
Radiance	L_e	Watts/($cm^2 \cdot sr$)	L_q	photons/($cm^2 \cdot s \cdot sr$)

To translate between energy-based and photon-based units, use the relationship that defines the energy of a photon

$$E_{\text{photon}} = \frac{hc}{\lambda} \quad (2.1)$$

where h is Planck's constant ($6.626 \times 10^{-34} [J \cdot s]$), c is the speed of light ($2.998 \times 10^8 [m/s]$), and λ is the wavelength associated with the photon.

Before a full discussion can begin on the quantities described above, the concept of the solid angle (Ω) must be addressed since intensity and radiance incorporate this quantity with units of steradians $[sr]$. The solid angle is expressed as the ratio between an area on the surface of a sphere (A) and the sphere's radius (r):

$$\Omega = \frac{A}{r^2} \quad (2.2)$$

A sufficiently small, planar area ($A \ll r^2$) can also be viewed from some distance, r , and if it is observed from some angle, θ , defined by the surface normal and the line of sight, the solid angle subtended by that area would be defined by:

$$\Omega_{\text{tilted surface}} = \left(\frac{A}{r^2} \right) \cos \theta \quad (2.3)$$

The practical impact that the solid angle has on radiometric problems is that it defines either the solid angle through which the source emits radiation or the field of view (FOV) through which the detector collects radiation.

With solid angle defined, a discussion on the radiometric quantities in Table 2.1 can begin. Radiance is the first quantity discussed since it provides a general description for the source. Its textbook definition states that it is the amount of power radiated per unit projected source area per unit solid angle. Radiance is expressed in differential form by [5:45]:

$$L_e = \frac{\partial^2 \phi_e}{\partial A_s \cos \theta_s \partial \Omega_d} \quad (2.4)$$

where ϕ_e is the radiant flux [W], A_s is the area of the source, θ_s is the look angle with respect to the source normal and the detector, and Ω_d is the solid angle defined from the differential source element to a detector area that subtends it. The notation of equation (2.4) indicates that the radiance describes differential changes in the power with respect to differential changes in the projected source area and the detector's solid angle.

From this fundamental equation, all other radiometric quantities can be derived. Starting with radiant intensity, which is defined as the amount of radiant flux per unit solid angle, its value can be computed as:

$$I_e = \frac{\partial \phi_e}{\partial \Omega_d} = \int_{A_s} L_e \cos \theta_s dA_s. \quad (2.5)$$

Modifying (2.4) to provide radiant exitance, which is defined as the amount of radiant flux leaving a surface per unit surface area, yields:

$$M_e = \frac{\partial \phi_e}{\partial A_s} = \int_{\Omega_d} L_e \cos \theta_s d\Omega_d. \quad (2.6)$$

To find the radiant irradiance, which is the amount of radiant flux incident upon a surface per unit surface area, the solid angle of the detector of the form in (2.3) must be further defined with its differential form as

$$d\Omega_d = \left(\frac{dA_d}{r^2} \right) \cos \theta_d \quad (2.7)$$

where A_d is the area of the incident surface, r is the line-of-sight range from the incident surface to the source, and $\cos \theta_d$ is the angle from the line-of-sight range and the normal of the incident surface. Substituting (2.7) into (2.4) yields the definition of irradiance:

$$E_e = \frac{\partial \phi_e}{\partial A_d} = \int_{A_s} L_e \cos \theta_s \frac{\cos \theta_d}{r^2} dA_s. \quad (2.8)$$

The final radiometric quantity that needs to be computed is the total radiant flux. This value can be computed by simply integrating over the source area and either the solid angle of the detector or the detector area as is shown in the following equations, respectively:

$$\phi_e = \int_{\Omega_d} \int_{A_s} L_e \cos \theta_s dA_s d\Omega_d \quad (2.9)$$

$$\phi_e = \int_{A_d} \int_{A_s} L_e \cos \theta_s \frac{\cos \theta_d}{r^2} dA_s dA_d \quad (2.10)$$

2.1.1.1 Lambertian Surfaces. Often in basic radiometry, an implicit assumption is usually made about the type of sources that emit radiation: all surfaces are Lambertian radiators. Lambertian radiators are characterized as sources whose radiance is independent of view angle, θ_s . The main advantage of assuming a Lambertian radiator is in the relationship that exists between radiance and exitance under this assumption [5:47]:

$$M_e \left[\frac{W}{cm^2} \right] = L_e \left[\frac{W}{cm^2 \cdot sr} \right] \pi [sr] \quad (2.11)$$

The factor of π results from the integration of the solid angle in (2.6) over the entire hemisphere. In the real world, no sources are perfectly Lambertian.

2.1.2 Blackbody Radiation. A blackbody is a perfect radiator. As Dereniak states [5:55],

The blackbody radiates the maximum number of photons per unit time from a surface area in the wavelength interval that any body can radiate at a given kinetic temperature. No surface that is in thermodynamic equilibrium can radiate more photons.

Mathematically, blackbody radiation is described by the following equations, known as Planck's equations, in energy-based units and in photon-based units, respectively [5:66]:

$$L_{e,\lambda}(\lambda, T) = \frac{2hc^2}{\lambda^5 (e^{hc/\lambda k_B T} - 1)} \quad (2.12)$$

$$L_{q,\lambda}(\lambda, T) = \frac{2c}{\lambda^4 (e^{hc/\lambda k_B T} - 1)} \quad (2.13)$$

where k_B is Boltzmann's constant ($1.381 \times 10^{-23} [J/K]$) and T is the temperature [K]. These equations describe the spectral radiance that a source emits in terms of the temperature of that body. Figure 2.1 demonstrates the shape of blackbody curves for different temperatures across an IR waveband of 1-12 μm . As a note, the radiance

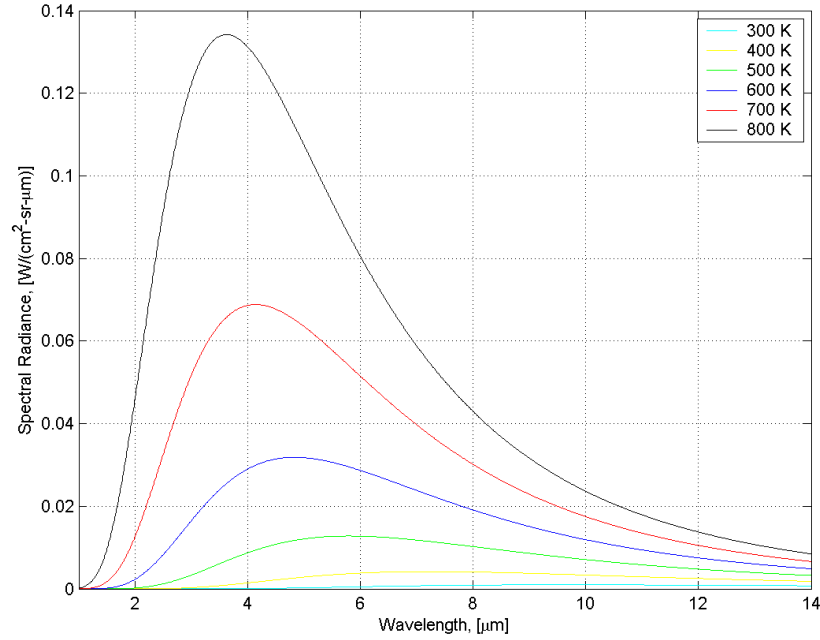


Figure 2.1: Ideal blackbody curves in terms of spectral radiance for the following temperatures: 300 K, 400 K, 500 K, 600 K, 700 K, and 800 K.

defined in equation (2.4) may be different than the spectral radiance defined here in that spectral radiance is defined as the radiance per unit wavelength. Typical units assigned to spectral radiance are $[W/(cm^2 \cdot sr \cdot \mu m)]$. Total radiance, as might be inferred in Section 2.1.1, results from the integration of the spectral radiance over a finite waveband:

$$L_e = \int_{\lambda_1}^{\lambda_2} L_{e,\lambda}(\lambda, T) d\lambda \quad (2.14)$$

One useful relationship that comes from Planck's equation is Wien's Displacement Law. Wien's Law is computed by taking the derivative of Planck's equation with respect to wavelength and setting it equal to zero to find the wavelength of peak spectral radiance as function of temperature. Using the energy-based Planck's equation (2.12), Wien's Displacement Law is described by:

$$\lambda_{max} = \frac{2898\mu m \cdot K}{T} \quad (2.15)$$

2.1.3 Emissivity. In the real world, no object is a perfect blackbody. As it is defined, a blackbody defines the upper limit of the spectral radiance produced by a source. Since no object is a perfect blackbody, a quantity needs to be defined by which the blackbody curve is scaled so that it represents what real objects radiate. This scaling is accomplished by defining an object's emissivity. Emissivity (ε) is defined as the ratio between the exitance of an actual source and the exitance of a blackbody, both of which are at the same temperature [5:72]:

$$\varepsilon(\lambda, T) = \frac{M_{e,source}(\lambda, T)}{M_{e,blackbody}(\lambda, T)} \quad (2.16)$$

In all cases, $\varepsilon \leq 1$.

Sources can be divided into several different classifications based on their emissivities. When a source has an emissivity of one, it is called a blackbody. If the emissivity is less than one and is the same value for all wavelengths, the source is classified as a graybody. In the case that the source's emissivity varies with wavelength, it is classified as a selective emitter. Selective emitters are the most accurate representation of emissivity.

2.1.3.1 Kirchhoff's Law. In order to understand what emissivity is fundamentally, a return to first principles is required. The law of conservation of

energy requires that [5:78]

$$\phi_{incident} = \phi_{reflected} + \phi_{transmitted} + \phi_{absorbed}. \quad (2.17)$$

If each term is normalized with respect to the incident flux, $\phi_{incident}$, a conservation expression develops that describes (2.17) in terms of reflectivity, ρ , transmissivity, τ , and absorptivity, α .

$$\rho + \tau + \alpha = 1 \quad (2.18)$$

Applying this conservation expression to an opaque body (*i.e.*, $\tau = 0$), incident flux is either reflected or absorbed, and (2.18) can be modified to represent the relationship between absorptivity and reflectivity.

$$\alpha = 1 - \rho \quad (2.19)$$

Furthermore, when a mass is in thermodynamic equilibrium with its surrounding environment, if it absorbs the incident radiation, it must re-radiate an equal amount of energy in order to remain in thermal equilibrium. This requirement is the crux of Kirchhoff's law; absorptivity equals emissivity:

$$\varepsilon = \alpha. \quad (2.20)$$

This conclusion applies to both integrated and spectral radiometric values. Applying this conclusion allows the following statement to be made: good absorbers are good emitters.

2.1.4 Radiometric Measures of Temperature. When observing an object radiometrically, as will be the case for this thesis, knowing its temperature is usually desired. The measured flux is a function of both the object's temperature and emissivity, which leads to a situation where there is one equation and two unknowns. If the object's emissivity is a known quantity, its true temperature can be determined

from the measured flux. However, if emissivity is an unknown quantity, methods and definitions exist that allow for temperatures to be estimated. Four such methods of estimation are radiation temperature, apparent temperature, brightness temperature, and color temperature.

2.1.4.1 Radiation Temperature. Radiation temperature, T_R , is defined as the blackbody source temperature that gives the same total exitance *over all wavelengths* as the measured exitance [16]. If a source is characterized as a graybody, the true temperature can be computed with the Stefan-Boltzmann law by the following:

$$M_{e,meas} = \varepsilon \sigma_e T^4 = \sigma_e T_R^4 \quad \text{which yields} \quad T = \frac{T_R}{\varepsilon^{1/4}} \quad (2.21)$$

where σ_e is the Stefan-Boltzmann's constant ($\frac{2\pi^5 k_B^4}{15h^3 c^2} \approx 5.676 \times 10^{-12} [W/(cm^2 \cdot K^4)]$).

2.1.4.2 Apparent Temperature. In the real world, collection of radiation over all wavelengths as described by the Stefan-Boltzmann law is impractical. Therefore, a quantity similar to radiation temperature, but defined as the blackbody source temperature that gives the same total exitance over a waveband, $\Delta\lambda$, is apparent temperature, T_A :

$$M_{e,meas} = \int_{\Delta\lambda} \varepsilon(\lambda) M_{e,BB}(\lambda, T) d\lambda = \int_{\Delta\lambda} M_{e,BB}(\lambda, T_A) d\lambda. \quad (2.22)$$

2.1.4.3 Brightness Temperature. Brightness temperature, T_B , is defined as the blackbody temperature of a source that gives the same exitance in a narrow spectral region, $\Delta\lambda$, about a central wavelength, λ_0 , as the measured exitance at λ_0 . If the emissivity of the object is known, the true temperature can found in the following expression, assuming a graybody:

$$M_e(\lambda_0, T_B) = \frac{2\pi h c^2}{\lambda_0^5 (e^{hc/\lambda_0 k T_B} - 1)} = \varepsilon \frac{2\pi h c^2}{\lambda_0^5 (e^{hc/\lambda_0 k T} - 1)} = M_{meas}(\lambda_0, T). \quad (2.23)$$

Solving for T yields the true temperature of the object [16]:

$$T = \frac{hc}{\lambda_0 k \ln [\varepsilon (e^{hc/\lambda_0 k T_B} - 1) + 1]} \quad (2.24)$$

2.1.4.4 Color Temperature. Color temperature, T_C , is defined as the blackbody temperature of a source that best matches the measured exitances in at least two spectral bands. This temperature is computed by taking the ratio of the measured exitances.

$$\frac{M_{e,meas}(\lambda_1, T)}{M_{e,meas}(\lambda_2, T)} = \frac{\varepsilon_1(\lambda_1)\lambda_2^5 (e^{hc/\lambda_2 k T} - 1)}{\varepsilon_2(\lambda_2)\lambda_1^5 (e^{hc/\lambda_1 k T} - 1)} = \frac{\lambda_2^5 (e^{hc/\lambda_2 k T_C} - 1)}{\lambda_1^5 (e^{hc/\lambda_1 k T_C} - 1)} \quad (2.25)$$

In the special case that the object can be modeled as a graybody, T_C is the true temperature of the object.

2.2 Infrared Optical System

With the fundamentals of radiometry defined, the next step is to develop the background theory behind the IR optical system which includes the optic and detector. This section of theory is important because it provides the basis for understanding how the radiometric signal is collected and generates an electronic signal.

2.2.1 Transmission Functions (Atmospheric, Optical, and Spectral Filter).

In a realistic scenario, the radiometric signal of an object, in spectral terms, observed by the optical system at some range is not the same signal originally emitted by the object. The signal experiences spectral attenuation from three sources. The first is naturally occurring because the attenuation is due to the atmosphere. The last two are based on choices made by the system designer which describe how much the optical system and a spectral filter spectrally attenuate the signal.

2.2.1.1 Atmospheric Transmission Functions. The atmospheric transmission function provides the means for describing how the atmosphere spectrally at-

tenuates the radiometric signal from the object to the observing optic. The function provides a scaling factor between zero and one as a function of wavelength which will weight the spectral components in a radiometric signal accordingly; one means that 100% of the spectral component was passed, and zero means the spectral component was completely blocked. An example of what an atmospheric transmission function looks like is shown in Figure 2.2. As is seen in Figure 2.2, specific spectral

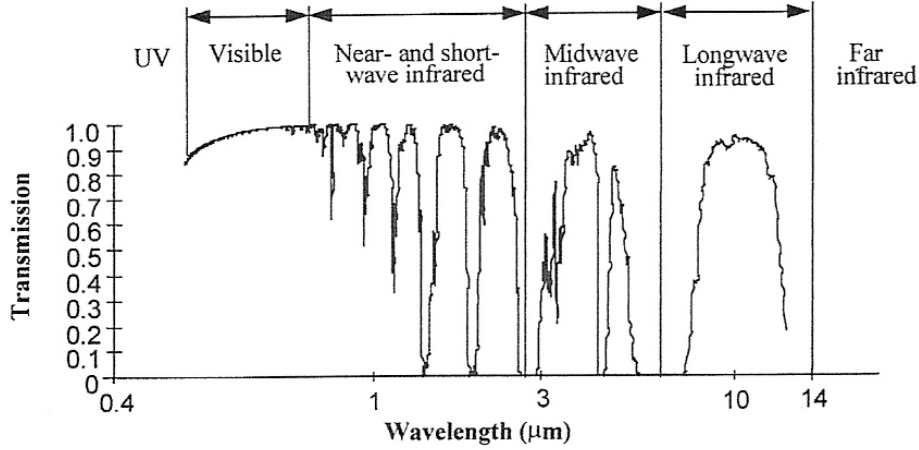


Figure 2.2: Example atmospheric transmission profile for a 1-km path length. [6:128].

regions, like 5-8 μm , allow for zero transmission. The reason for this phenomenon is that constituent molecules in the atmosphere, like H_2O and CO_2 , have the ability to absorb photons at these wavelengths. Figure 2.3 shows what wavelengths and primary atmospheric molecules contribute to the absorption in the IR spectral band. The amount of absorption experienced is highly dependent on the concentration of those absorbing molecules, so variables such as altitude and path length can have significant impacts on the amount of absorption experienced. The physics behind this phenomenon are not central to this thesis, but its effects must be accounted for in order to yield a high fidelity representation of the collected radiometric signal. In this thesis, this accounting is accomplished by using Phillips Laboratory Expert-assisted User Software (PLEXUS), which uses the Moderate Resolution Atmospheric Trans-

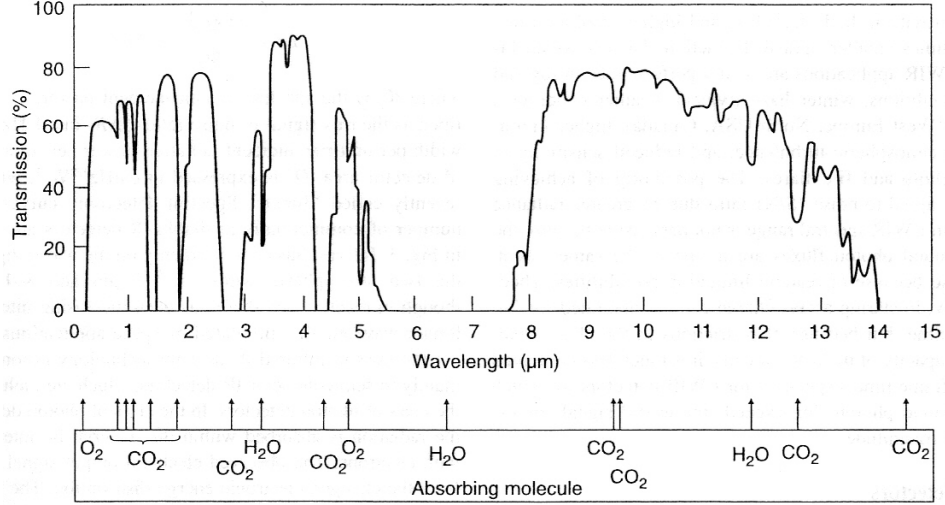


Figure 2.3: Absorbing molecules that affect the atmospheric transmission in the IR spectrum for a 6000 ft horizontal path at sea level. [20].

mission (MODTRAN) program to compute the atmospheric transmission function based on engagement geometry and meteorological parameters.

2.2.1.2 Optical Transmission Functions. The optical transmission function provides the means for describing how the optical system spectrally attenuates the observed radiometric signal as it passes through the optical system onto the spectral filter. The function provides a scaling factor between zero and one as a function of wavelength which will weight the spectral components in the observed radiometric signal accordingly; one means that 100% of the spectral component was passed, and zero means the spectral component was completely blocked. This attenuation is due to optical elements absorbing or reflecting small amounts of optical energy while allowing the remaining energy to be transmitted. The amount of attenuation is determined by the choice of materials used in creating the optical elements and the number of optical elements in the optical system. As an example, zinc selenide, which is used in optical elements for forward looking IR systems, has an average transmission of 0.70 in the 8-to-12- μm region [1, 13].

2.2.1.3 Spectral Filter Transmission Functions. The spectral filter transmission function provides the means for describing how the spectral filter spectrally attenuates the collected radiometric signal as it passes through the filter onto the detector. This function provides a scaling factor between zero and one as a function of wavelength which will weight the spectral components in the collected radiometric signal accordingly; one means that 100% of the spectral component was passed, and zero means the spectral component was completely blocked. The primary purpose of the spectral filter is to limit the spectral extent of the collected signal to a waveband of interest; the choice of that waveband is determined by a system designer. As with the optical transmission function, attenuation in the spectral filter is due to the filter material absorbing or partially reflecting certain wavelengths of optical energy while allowing others to be transmitted. Quality spectral filters will have a high transmittance that is constant across the passband, and a low transmittance outside of the passband.

2.2.2 Modulation Transfer Functions. The next theoretical topic that must be discussed involves modeling the IR camera using the MTF. The necessity of this discussion is due to the fact that optical systems do not form ideal images of objects; in reality, images are blurred due to diffraction effects inherent to the optical system. As a result, the irradiance that is collected by an optic is distributed across the image plane where a detector like an FPA is located. For example, when an optical system with a circular aperture observes a point source, the irradiance does not reform into the ideal image of the point source. Instead, the optical system distributes the irradiance into a form known as the Airy disk. Mathematically, the Airy disk is described by a Bessel function of the first kind, order one, as is shown in Figure 2.4 [10:15]. The blurring that occurs because of the optical system due to diffraction can ultimately be characterized through the application of linear systems theory to yield a tool called the modulation transfer function. Since linear systems theory is the basis for the MTF, the MTF's construction will be centered around the concepts of spatial frequency and

the Fourier transform. Therefore, this section will define spatial frequency, the MTF and how it is computed, discuss the spatial invariance assumption for the MTF, and demonstrate how the MTF is applied to an image.

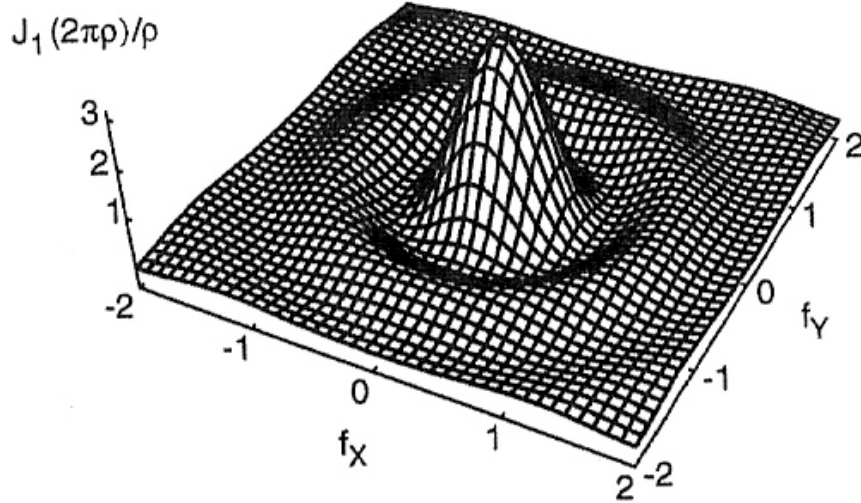


Figure 2.4: Diffraction-limited Airy disk pattern produced by a circular pupil. [10:14].

2.2.2.1 Spatial Frequency. Spatial frequency is a measure of how features in a scene, which can be viewed in terms of irradiance, vary in terms of distance. Rapidly changing irradiance patterns correspond to high spatial frequencies; conversely, irradiances that change slowly with position correspond to low spatial frequencies. The units for spatial frequency are typically expressed in terms of $1/[\text{distance}]$. As a visual demonstration of this idea, consider Figure 2.5. As the irradiance varies across this one-dimensional slice of the two-dimensional irradiance distribution, features of both low and high spatial content can be seen given the distance over which the irradiance varies. The power of this spatial frequency concept is fully realized with the realization that all the Fourier frequency decomposition tools developed in linear systems theory for time-domain electrical signals can be applied to images.

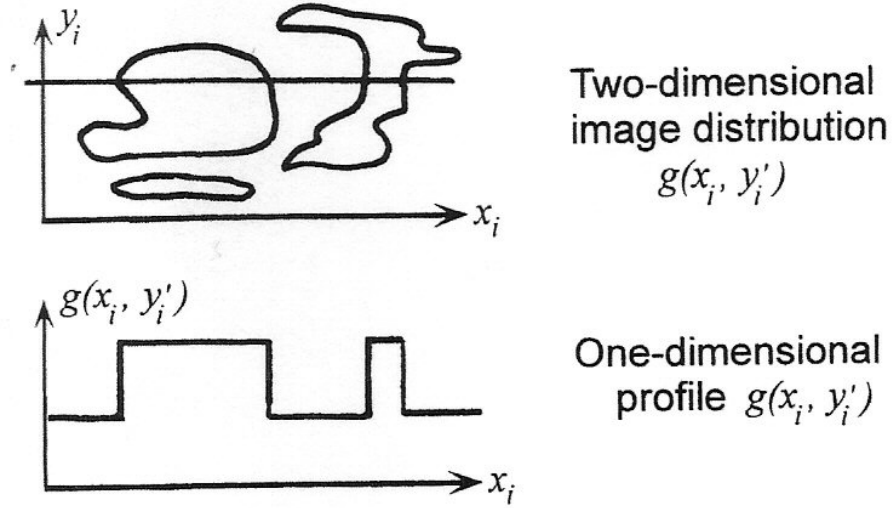


Figure 2.5: Generalized definition of a spatial-domain irradiance distribution. [2:5].

2.2.2.2 Definition of the MTF. By definition, the MTF is the magnitude response of the detection system, so it provides a weighting function to describe the amount of contrast in the system for a given spatial frequency. This effect is demonstrated in Figure 2.6. As the spatial frequency content increases, the amount of contrast seen at the image plane of the optical system goes to zero. The point at which the contrast is zero defines the cutoff spatial frequency of the MTF. The power of the MTF comes from its ability to model many different components and factors that make up an IR simulation. Examples include the optical system, detector size, sampling effects in an FPA, atmospheric turbulence, and motion effects. The MTFs that are represented ultimately depend upon the requirements of the simulation.

2.2.2.3 Methods of Computing the Optical MTF. In order to compute the MTF of the optical system, recognition is required that it comes from a more generalized description of the optical system since the MTF is only the magnitude response. That generalized description is called the optical transfer function (OTF). The OTF provides a more complete description of optical system effects on collected light because it represents both magnitude and phase responses. The MTF can be

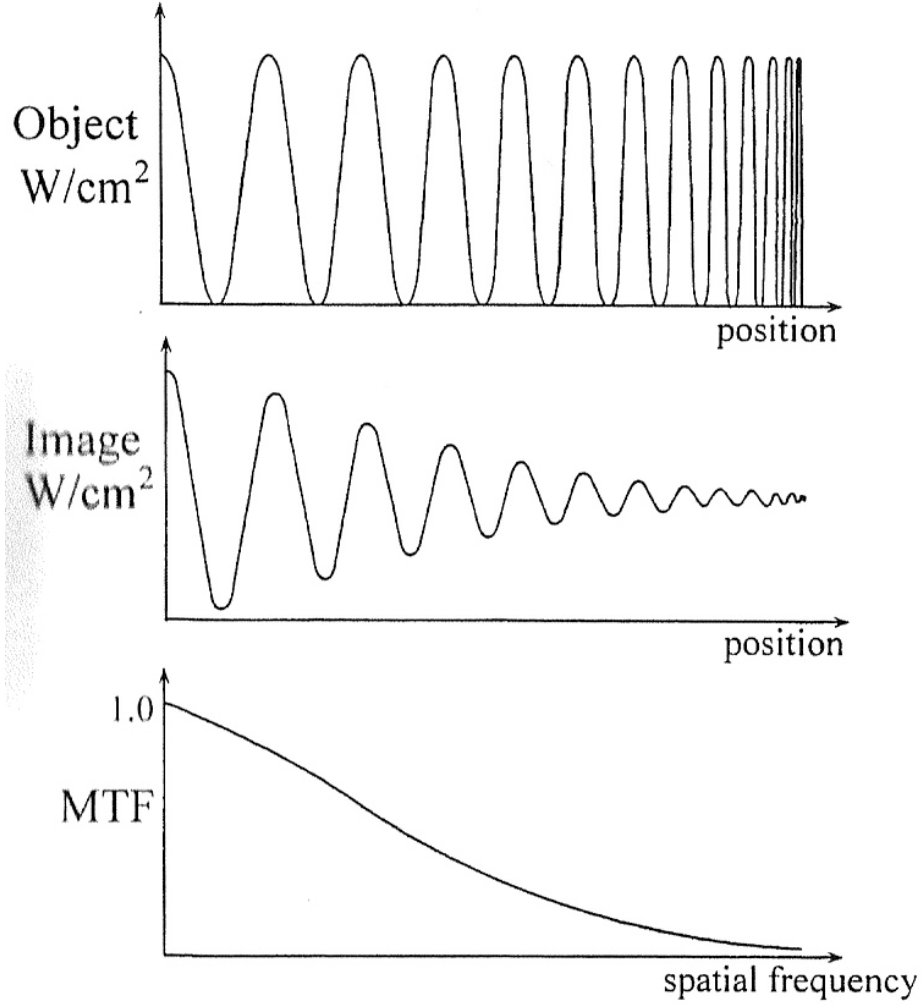


Figure 2.6: Modulation transfer function effects on the modulation depth as spatial frequency increases. [2:12].

interpreted from the OTF as being the magnitude response by [2:70]:

$$OTF(f_X, f_Y) = MTF(f_X, f_Y)e^{-iPTF(f_X, f_Y)} \quad (2.26)$$

where PTF is the phase transfer function, and f_X and f_Y are spatial frequencies. Since this thesis is concerned with only incoherent, diffraction-limited imaging, phase effects can be ignored because diffraction-limited OTFs are always real and non-negative [10:142].

Computation of the MTF can be done using two different methods. For the first method, the diffraction-limited OTF is computed using [10:141]:

$$OTF(f_X, f_Y) = \frac{\int_{-\infty}^{\infty} \int_{-\infty}^{\infty} P\left(x + \frac{\lambda s_i f_X}{2}, y + \frac{\lambda s_i f_Y}{2}\right) P\left(x - \frac{\lambda s_i f_X}{2}, y - \frac{\lambda s_i f_Y}{2}\right) dx dy}{\int_{-\infty}^{\infty} \int_{-\infty}^{\infty} P(x, y) dx dy} \quad (2.27)$$

where $P(x, y)$ is the pupil function that represents the pupil of the optical system and s_i is the distance the light is propagated, which in the case of this thesis is the distance to the image plane. The MTF is simply:

$$MTF(f_X, f_Y) = |OTF(f_X, f_Y)| \quad (2.28)$$

As a note, equation (2.27) has an important geometric interpretation. The numerator represents an area of overlap between two pupil functions whose centers are located diametrically opposite of each other in real space with Cartesian coordinates, (x, y) , at $\left(\frac{\lambda s_i f_X}{2}, \frac{\lambda s_i f_Y}{2}\right)$ and $\left(-\frac{\lambda s_i f_X}{2}, -\frac{\lambda s_i f_Y}{2}\right)$, which effectively describes an autocorrelation. The denominator provides a normalization based the total area of the pupil [10:142]. Again in (2.27), notice the two pupil functions' dependencies on wavelength. This critical observation has a significant impact in the creation of this simulation; the OTF and ultimately the MTF are spectral quantities. As a consequence, the MTFs that are modeled will have to vary over the simulated waveband. This consequence is additionally supported by the computation of the MTF's cutoff frequency, which also has a dependence upon wavelength as seen in the following equation:

$$f_{cutoff} = \frac{1}{\lambda F/\#} \quad \text{where} \quad F/\# = \frac{f}{D} \quad (2.29)$$

where f is the effective focal length of the optical system and D is the aperture diameter.

The second method provides for a much simpler way of computing the MTF than the first by requiring the computation of the optical system's point spread function (PSF). By definition, the PSF is simply the optical system's response to a point source, which is analogous to the impulse response as defined by linear systems theory. Once the PSF has been computed, simply taking the two-dimensional Fourier transform of the PSF will yield the MTF, as shown by:

$$MTF_{optics}(f_X, f_Y) = |\mathcal{FF}\{PSF(x, y)\}| \quad (2.30)$$

where \mathcal{FF} notationally represents a two-dimensional Fourier transform. A two-dimensional MTF is required since the PSF is a function of two spatial components. Additionally, this method provides a much easier way of taking into account complex pupil functions since all pupil geometry effects are included within the PSF. In this thesis, the implemented pupil function is described by a circular aperture that contains a circular, central obscuration, which is indicative of catadioptric telescopes like Schmidt-Cassegrain. The method by which the PSF is computed will be discussed in the next chapter.

2.2.2.4 Spatial Invariance Assumption for the MTF. Since the MTF is computed with the Fourier transform, certain assumptions must be made about the MTF's properties so that it can meet the mathematical requirements of the Fourier transform. Since this thesis focuses on only incoherent imaging, the only MTF property of concern is spatial invariance, which Williams and Becklund term as isoplanatism [24:60]. Spatial invariance requires that a translation of the object in the object plane produces just a proportional translation of the entire PSF in the image plane; no other change occurs within the PSF.

2.2.2.5 Applying the MTF to an Image. Applying the MTF's effects on an irradiance distribution, $E(x, y)$, can be achieved using one of two methods. The most direct method is two-dimensionally convolving the PSF with the irradiance

distribution in order to yield the resulting image, as shown by:

$$E_{img}(x, y) = PSF(x, y) \otimes E(x, y) \quad (2.31)$$

where $E(x, y)$ is the ideal irradiance distribution of an image at the image place and $E_{img}(x, y)$ is the irradiance distribution at the image plane due to the optical system resulting from the convolution. The second method, which is computationally easier, applies linear systems theory to (2.31) to yield the following:

$$E_{img}(x, y) = \mathcal{F}^{-1} \mathcal{F}^{-1} [MTF_{sys}(f_X, f_Y) \times \mathcal{FF} \{E(x, y)\}] \quad (2.32)$$

where $\mathcal{F}^{-1} \mathcal{F}^{-1}$ notationally represents a two-dimensional inverse Fourier transform. The importance of the above equation is primarily due to the $MTF_{sys}(f_X, f_Y)$ term; it allows the overall detection system to be represented by not just the optical MTF, but can include MTFs defining FPA pixel sizes, FPA image sampling effects, atmospheric turbulence, and other non-optical MTFs like motion and vibration effects. To get the overall system-level MTF, multiplication of the various individual MTFs is all that is required. In the case of this thesis, only the MTFs for optical, FPA pixel size, sampling, and atmospheric turbulence are considered. The details behind each of these MTFs are discussed in Chapter III.

2.2.3 Detector Response. The final theoretical area that merits discussion is the detector response, which will take the irradiance collected by the optical system and convert that radiation into an electronic current that can be measured. For this thesis, the chosen detector technology that is modeled is a photovoltaic FPA. Therefore, this section will provide an overview of photovoltaic technology, quantum efficiency, and the relationship between integration time and noise-equivalent bandwidth.

2.2.3.1 Photovoltaic Detectors. A fundamental description of a photovoltaic detector is that it is a semiconductor diode, and it produces a voltage or current that is proportional to the amount of photon radiation. Looking at current specifically, the amount of photogenerated current produced by incident photons is determined by [5:93]:

$$i_g = \eta E_q A_d q \quad (2.33)$$

where η is the quantum efficiency of the detector material, A_d is the area of the detector, and q is the charge of an electron ($1.602 \times 10^{-19}[C]$). The photogenerated current will get coupled into the overall current through the diode by [5:93]:

$$i = i_0 (e^{qv/bk_B T_d} - 1) - i_g \quad (2.34)$$

where i_0 is the reverse saturation current, v is the applied voltage across the diode, T_d is the diode's temperature, and b is a nonlinearity factor. The effect that the photocurrent has on the diode current is shown in the I-V curve in Figure 2.7. How the photodetector is biased will determine the portion of the total diode current that is not photogenerated; this is called dark current. Typically, FPA photodetectors are strongly reverse biased in order to move electrons through the junction. As a result, the dark current will be some value along the flat part of the I-V curve in Figure 2.7.

2.2.3.2 Quantum Efficiency. The parameter that expresses how well a photon detector material converts an incident photon into a photogenerated electron is quantum efficiency, η . Like the transmission functions discussed in section 2.2.1, quantum efficiency is a spectral quantity that varies between zero and one. As a rule, quantum efficiency restricts the counting of electrons to only those photogenerated, instead of electrons generated by other gain mechanisms internal to a detector, and it encapsulates effects due to absorption, reflection, scattering, and electron recombination [5:87].

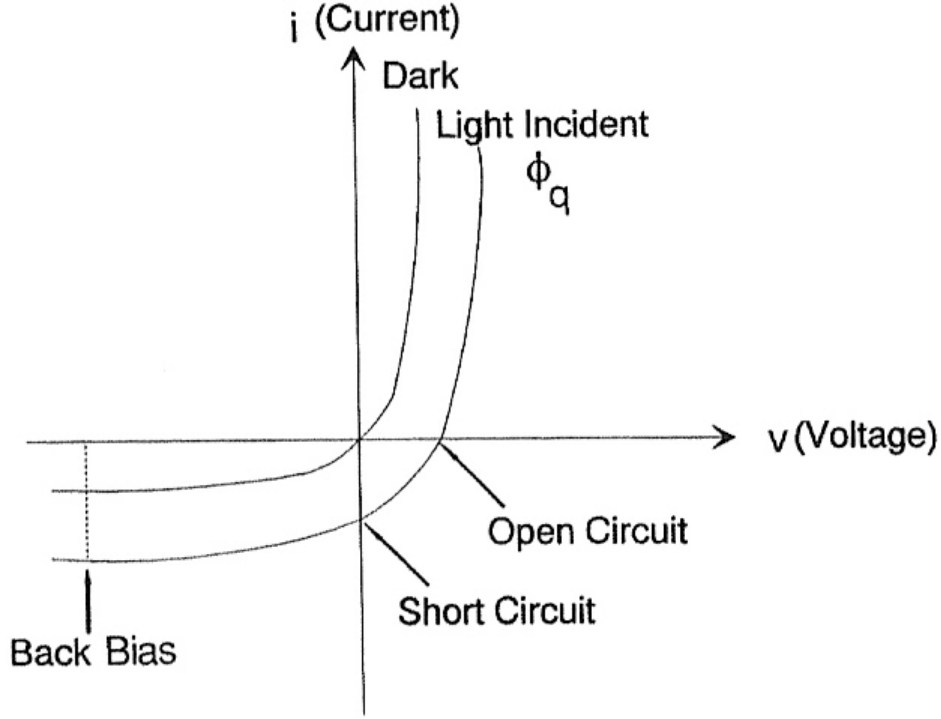


Figure 2.7: Characteristic current-voltage (I-V) curve for a photodiode. [5:92].

Quantum efficiency can be expressed as

$$\eta(\lambda) = \left(1 - \frac{(n(\lambda) - 1)^2}{(n(\lambda) + 1)^2}\right) (1 - e^{-\alpha(\lambda)l_x}) \quad (2.35)$$

where the quantity $\frac{(n(\lambda)-1)^2}{(n(\lambda)+1)^2}$ represents the Fresnel reflectance, $n(\lambda)$ is the spectral index of refraction, $\alpha(\lambda)$ is the spectrally-defined absorption coefficient, and l_x corresponds to the thickness of the detector material [5:89]. In order to have a high quantum efficiency, the Fresnel reflectance must be low so that the optical radiation can get into the detector material, and the detector thickness should be large enough to ensure that the optical radiation can be absorbed [5:89]. Fresnel reflectance is the primary controlling factor in the quantum efficiency as shorter wavelengths. The reduction in quantum efficiency at longer wavelengths is controlled by the detector's absorptivity. This phenomenon is due to the tendency of longer wavelengths to be transmitted through the material instead of being absorbed [5:90]. The wavelength

corresponding to no absorption since the photon energy is less than bandgap energy in the detector material is called the cutoff wavelength. An example quantum efficiency curve is shown in Figure 2.8. This curve was generated using measured complex

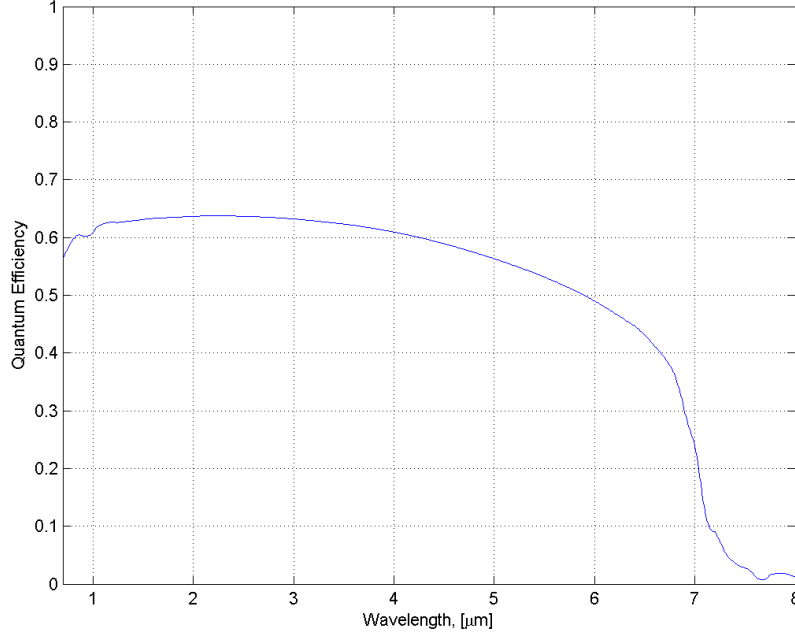


Figure 2.8: Quantum efficiency for InSb at 300K.

index-of-refraction data for indium antimonide (InSb) at 300 K [18:495].

Complex index-of-refraction data from sources like Palik [18] provides the means to simulate detector response with a high degree of fidelity. This capability is possible since the real part of the complex index of refraction is the value associated with equation (2.35), and the imaginary part represents an extinction coefficient of the material (k), which can be converted to an absorption coefficient by [19:656]:

$$\alpha(\lambda) = \frac{4\pi k}{\lambda}. \quad (2.36)$$

2.2.3.3 Noise-Equivalent Bandwidth. Since this thesis will model the effects that integration time has on the SNR, it is important to discuss the relationship between integration time (τ) and the noise-equivalent bandwidth (Δf). Assuming the

noise power spectrum from the detector is white noise, the noise bandwidth can be computed as [5:189]:

$$\Delta f = \frac{1}{\mathcal{G}^2(f_0)} \int_0^{\infty} \mathcal{G}^2(f) df \quad (2.37)$$

where $\mathcal{G}(f)$ is the voltage gain as a function of frequency and f_0 corresponds to the frequency associated with maximum gain. Feeding a time-domain, rectangular pulse of width, τ , whose Fourier transform is defined by

$$g(t) = \text{rect}\left(\frac{t}{\tau}\right) \iff \mathcal{G}(f) = \tau \left(\frac{\sin \pi \tau f}{\pi \tau f}\right), \quad (2.38)$$

into (2.37) yields a noise-equivalent bandwidth of

$$\Delta f = \frac{1}{2\tau}. \quad (2.39)$$

The implication of this equation is that as integration time increases, the noise-equivalent bandwidth will decrease. In this thesis, equation (2.39) is the relationship used to relate integration time to the noise-equivalent bandwidth.

2.3 Summary

From this chapter, the definitions and theories behind optical radiometry, optical system modeling, and photovoltaic detector response provide a solid foundation and necessary tools in order to construct the IR camera simulation. In Chapter III, all these tools will be put into practice as the various components of the IR camera simulation are built. Chapter III will provide in-depth details and discussion behind the development of the simulation.

III. Model Development

This chapter details the development of the overall IR camera simulation. This discussion will address the following questions:

- How is the simulation fundamentally setup from the target to the observer?
- How is the radiometry computed to provide a realistic signal?
- How are the various MTFs representing different components modeled and what are their effects?
- How is the photovoltaic FPA detector modeled?
- What detector noise sources limit the computed signal?

3.1 *Modeling Methodology*

Two aspects in the IR camera simulation’s modeling of the target-to-observer scenario must be discussed first since they affect the overall simulation setup. The first aspect discusses why the simulation is a spectral model. The second aspect discusses how physical sizes are scaled in the three planes that make up the simulation: the object plane, the pupil/aperture plane, and the image plane.

3.1.1 Spectral Model. In order to provide the highest possible fidelity, the model treats many variables as spectral quantities in order to account for realistic variations in their values at different wavelengths. This requirement is justified when considering variables, like atmospheric transmission, which serve to attenuate the received signal. By not incorporating its spectral effects over a waveband, the computed signal would be an overestimate of what really is measured.

3.1.2 Scaling in the Object, Aperture, and Image Planes. The scaling between the object, aperture and image planes is fundamentally important for this simulation because it ensures that the radiometry is properly scaled throughout the simulation. This discussion starts with the object plane since the main simulation

input is located there. The main simulation input is a temperature distribution that varies with position, $T(x_{trg}, y_{trg})$. The details of what $T(x_{trg}, y_{trg})$ represents and how it is computed occurs in section 3.2.2. Within MATLAB, which was used to create this simulation, $T(x_{trg}, y_{trg})$ is represented as a matrix of $N \times N$ elements. As a note, the self-emitted radiance computations use $T(x_{trg}, y_{trg})$, and those answers result in $N \times N$ matrices. In the computation of $T(x_{trg}, y_{trg})$, the physical spacing in the object plane between each adjacent matrix element, Δx_{trg} , must be specified by the simulation user. So, as a result of this representation, any temperature represented in the matrix corresponds to an area defined by Δx_{trg}^2 .

For this simulation, the simulated optical system locates the detector at the image plane as determined by the Gaussian lens equation from geometric optics

$$\frac{1}{s_{trg}} + \frac{1}{s_{img}} = \frac{1}{f_{eff}} \implies s_{img} = \left[\frac{1}{f_{eff}} - \frac{1}{s_{trg}} \right]^{-1} \quad (3.1)$$

where s_{trg} is the distance from the optic to the object plane, s_{img} is the distance from the optic to the image plane, and f_{eff} is the effective focal length of the optical system. From equation (3.1), a magnification factor, M_{opt} , relating size in the object plane to that in the image plane is computed by dividing s_{img} by s_{trg} . As a result, Δx_{trg} translates to the image plane by this magnification term.

$$\Delta x_{img} = M_{opt} \times \Delta x_{trg} \quad (3.2)$$

In terms of the simulation, Δx_{img} corresponds to the spacing between adjacent elements in the $N \times N$ matrix in the image plane.

With Δx_{img} computed, the image plane can be represented in terms of spatial frequency by a sampling equation from wave optics [9]:

$$\Delta f_{img} = \frac{1}{N \Delta x_{img}} \quad (3.3)$$

where Δf_{img} represents the spatial frequency spacing between matrix elements in the Fourier-transformed image, and N is the number of matrix elements in one dimension, which for this simulation, will be the same N as in $T(x_{trg}, y_{trg})$. Spatial frequency spacing is very important in the simulation because the MTFs will apply their contrast weights to the spatial frequencies spaced by Δf_{img} . As mentioned in the previous chapter, the MTFs are spectral quantities because their cutoff spatial frequencies are functions of wavelength. The advantage of this development of Δf_{img} is that it maintains the same spatial frequency scale independent of wavelength.

As a consequence of this wavelength-independent spatial frequency scale, all MTFs must be computed to ensure their values are registered to the same spatial frequency scale. To accomplish this spatial frequency registering, the physical scaling in the aperture plane must be defined, which is computed from another wave-optics sampling equation relating physical sizes between the aperture and image planes [9]:

$$\Delta x_{ap} = \frac{\lambda s_{img}}{N \Delta x_{img}} \quad (3.4)$$

where Δx_{ap} is the spacing between adjacent matrix elements in the aperture plane. With Δx_{ap} defined as a function of wavelength, the number of matrix elements used to represent the aperture will vary according to wavelength. If the diameter of the aperture is defined by D_{ap} , the number of matrix elements used to define that aperture will be

$$N_{ap}(\lambda) = \frac{D_{ap}}{\Delta x_{ap}(\lambda)} \quad (3.5)$$

As will be demonstrated in a succeeding section on computing the optical MTF, varying the number of elements representing the aperture by wavelength will produce accurate MTFs that maintain spatial frequency registration in the image plane.

As a cautionary note about this method of determining spacings in the object, aperture and image planes, tradeoffs exist between the parameters described above which may prevent an accurate simulation or may cause an excessively long simulation run-time. Using engagement scenario parameters that will be defined in the next chap-

Table 3.1: Simulation sampling size considerations for different object plane spacings.

$\Delta x_{trg}[m]$	$N_{ap}(3.4\mu m)$	$N_{ap}(12.0\mu m)$
5.0e-01	5721	1621
1.0e-01	1144	324
5.0e-02	572	162
1.0e-02	114	32
5.0e-03	57	16
1.0e-03	11	3
5.0e-04	6	2
1.0e-04	1	0

ter, tradeoffs exist between Δx_{trg} , λ , and N_{ap} . For example, letting $s_{trg} = 15795m$, $D_{ap} = 0.6m$, $f_{eff} = 6m$, and $N = 1024$, Table 3.1 shows the computed values for N_{ap} using different Δx_{trg} and λ values.

From Table 3.1, larger values of Δx_{trg} produce more aperture-diameter matrix elements but at the expense of resolution in $T(x_{trg}, y_{trg})$. Conversely, smaller values of Δx_{trg} produce fewer aperture-diameter matrix elements even though resolution is increased in $T(x_{trg}, y_{trg})$. Also, notice the difference in N_{ap} between the two wavelengths; simulation runs over a very large waveband like 1 to 12 μm may not be possible given the variability in N_{ap} . For this thesis, $\Delta x_{trg} = 5$ mm is chosen because it provides sufficient resolution in $T(x_{trg}, y_{trg})$ while providing enough matrix elements to effectively represent the aperture.

3.2 Modeling the Radiometry

Now that the object, aperture and image planes have been set up, defining the radiometry for the engagement scenario can begin. The first step will be to define all the radiometric assumptions used in the simulation. An explanation of the temperature distribution, $T(x_{trg}, y_{trg})$, follows. Then, detailed explanations about all the radiometric contributors and how they sum together to produce an irradiance on the detector will be covered.

3.2.1 Radiometric Assumptions. Two main assumptions are made in this thesis that will aid in simplifying the radiometry. The first assumption is that the target's surface is Lambertian. Rationale supporting that assumption is as follows. For the engagement scenario explicitly stated by DETEC, the ABL, target, and observer are coplanar to each other [4]. The slant range from the target to observer is 15.8 km, which can be broken into a target altitude of 13.9 km at a ground range of 7.5 km from the observer. This thesis is making an implicit assumption that the axis of the missile is at zero degrees with respect to zenith. From this scenario configuration, the observer is looking at the missile at an elevation angle of 61.6 degrees. Given this observation angle, the assumption can be made that the target's surface is sufficiently diffuse such that it can be classified as Lambertian. This assumption is justified by studying the bidirectional reflectance distribution function (BRDF) for two possible surface treatments of the missile: bare aluminum and gloss white paint on aluminum. For the bare aluminum, the change in emissivity is less than 1% across 90% of the missile's surface; while the gloss white paint experienced a change in emissivity of less than 1% across 80% of the missile's surface. A complete explanation of these two claims is located in Appendix A.

For the second assumption, which is also based on the diffuse-surface assumption discussed in Appendix A, this model assumes that the target's emissivity can be modeled using fractional specularity. Using theory developed in section 2.1.3.1 and thesis work conducted by Bortle [3], the emissivity of the target can be expressed as:

$$\varepsilon(\lambda) = 1 - \rho_{tot}(\lambda) \quad (3.6)$$

where $\rho_{tot}(\lambda)$ is the total reflectance of the target. However, under the diffuse/fractional-specularity model, $\rho_{tot}(\lambda)$ can be further divided into a specular reflectance and a diffuse reflectance. All three quantities are related by [3:21]:

$$\rho_{tot}(\lambda) = \rho_{spec}(\lambda) + \rho_{diff}(\lambda). \quad (3.7)$$

Therefore, the target's emissivity that will be modeled in the simulation is

$$\varepsilon(\lambda) = 1 - \rho_{spec}(\lambda) - \rho_{diff}(\lambda) \quad (3.8)$$

Seeing that equation (3.8) still has a dependence on wavelength, a further assumption can be made to remove that dependence. Looking at reflectance measurements made by Bortle for bare aluminum [3:46], as seen in Figure 3.1, the total reflectance remains fairly constant over the waveband displayed. But looking at the specular and diffuse reflectivities shows more variation in their respective reflectivities as wavelength changes. The yellow line representing a 60-degree look angle from surface normal is the data that best represents the engagement scenario presented in this thesis. One waveband that is considered in this thesis is 3.4 - 4.2 μm ; the variation in this band is no more than 3% for both specular and diffuse reflectance. For Bortle's 8-to-12- μm data, the variation is no more than 5% for both reflectance cases. Given that this reflectivity variation in both bands is rather small, this thesis will assume that the specular and diffuse reflectivities remain constant as a function of wavelength.

3.2.2 Temperature Distribution. As stated in section 3.2.1, the temperature distribution, $T(x_{trg}, y_{trg})$, serves as the main input to the IR camera simulation. The only values represented in this matrix are the temperatures on the missile body as is shown in Figure 3.2. The distribution was computed for this thesis by Paul Mattie, a colleague also working on DIAT. Figure 3.2 represents how an assumed Gaussian temperature spatial distribution in a plane normal to the surface normal at the center of the Gaussian projects around the 1-m diameter cylindrical body that is viewed from below at a 61.6-degree view angle by the observer. The Gaussian temperature distribution assumption is made given that the beam irradiance distribution produced by the HEL is also Gaussian. The maximum temperature assumption of 800 K, which is just below the melting point of aluminum, was provided for this thesis by Dr. William Bailey, an AFIT professor also working on DIAT, to be a reasonable value for peak temperature. The σ for this Gaussian distribution is assumed to be 0.2 m.

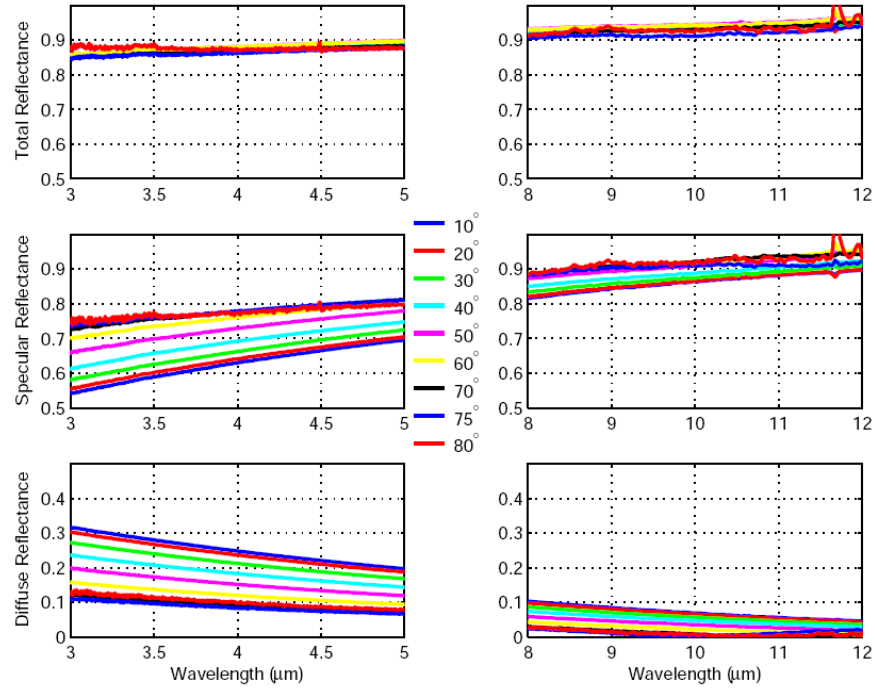


Figure 3.1: Reflectance data for the bare aluminum surface. [3:46].

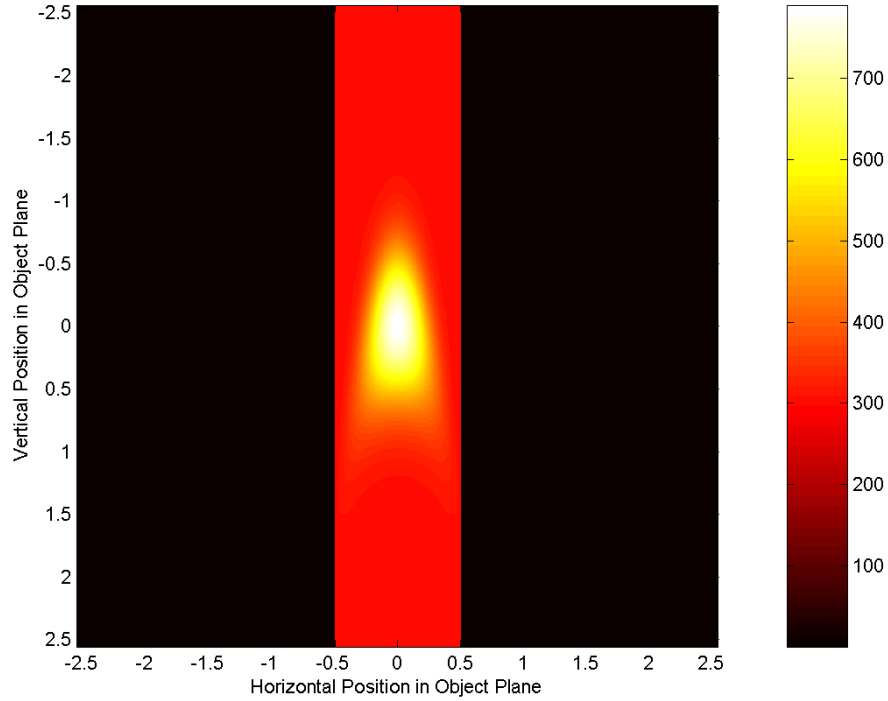


Figure 3.2: HEL-induced missile body temperatures with peak temperature at 800 K, missile body at 300 K, and the background at 0 K.

All other missile body temperatures not induced by the HEL are assumed to be 300 K in order to account for any background- and aerodynamic-heating effects of the missile body.

3.2.3 Self-Emission. To determine the irradiance incident upon the FPA detector due to the temperature distribution, $T(x_{trg}, y_{trg})$, a general equation showing how the detector irradiance is computed is required. Starting with equation (2.4),

$$L = \frac{\partial^2 \phi}{\partial A_{trg} \cos \theta_{trg} \partial \Omega} \quad (3.9)$$

where the differential solid angle is expressed in terms of:

$$d\Omega = \frac{dA_{opt}}{s_{trg}^2} \cos \theta_{opt} \quad (3.10)$$

where s_{trg} is the range to the missile from the observer's position, A_{opt} is the effective area of the optical system's aperture, and θ_{opt} is the angle between the optical system's optical axis and the line-of-sight from the observer to the missile. Substituting in the differential solid angle and solving for the differential flux yields:

$$\partial^2 \phi = L \cos \theta_{trg} \frac{\cos \theta_{opt}}{s_{trg}^2} \partial A_{trg} \partial A_{opt} \quad (3.11)$$

Since the radiant flux collected by the aperture equals the radiant flux incident on the detector, the differential source area, ∂A_{trg} , can be expressed in terms of differential area at the image plane of the optical system by taking advantage of the optical system's magnification, M_{opt} :

$$\begin{aligned} A_{img} = A_{trg} (M_{opt})^2 &\Rightarrow A_{img} = A_{trg} \left(\frac{s_{img}}{s_{trg}} \right)^2 \Rightarrow A_{trg} = A_{img} \left(\frac{s_{trg}}{s_{img}} \right)^2 \\ \partial A_{trg} &= \partial A_{img} \left(\frac{s_{trg}}{s_{img}} \right)^2. \end{aligned} \quad (3.12)$$

Substituting this value back into equation (3.11) and simplifying, the irradiance produced by the target in the image plane can be expressed as an integration over the optical aperture:

$$E_{e,trg}(x_{img}, y_{img}) = \frac{\partial \phi}{\partial A_{img}} = \frac{L_e(T(x_{trg}, y_{trg})) \cos \theta_{trg} \cos \theta_{img}}{s_{img}^2} \int_{A_{opt}} dA_{opt} \quad (3.13)$$

where $\theta_{img} = \theta_{opt}$ since they share the optical axis of the optical system. To provide some generality to the IR camera simulation, the optical aperture can be configured to include a central obscuration as would be the case for any catadioptric system. The effective aperture in radiometric terms is simply the area of the aperture minus the area of the obscuration. For the simulation, only circular apertures and obscurations are considered:

$$A_{eff} = A_{opt} - A_{obsc} = \pi \left(\frac{D_{opt}}{2} \right)^2 - \pi \left(\frac{D_{obsc}}{2} \right)^2 = \frac{\pi}{4} (D_{opt}^2 - D_{obsc}^2). \quad (3.14)$$

Substituting equation (3.14) back into equation (3.13) will yield the general equation for irradiance at the image plane:

$$E_{e,img}(x_{img}, y_{img}) = \left(\frac{L_e(T(x_{trg}, y_{trg})) \cos \theta_{trg} \cos \theta_{img}}{s_{img}^2} \right) \frac{\pi}{4} (D_{opt}^2 - D_{obsc}^2). \quad (3.15)$$

From what equation (3.15) describes, the irradiance at an image plane can be computed by simply scaling the object's radiance by the effective aperture area divided by the square of the image distance. This fact will be applied to all other radiance sources modeled in the simulation.

Since the simulation is based on spectral definitions, equation (3.15) must be modified to compute spectral quantities. The spectral irradiance at the image plane is:

$$E_{e,img}(\lambda, x_{img}, y_{img}) = \left(\frac{L_e(\lambda, T(x_{trg}, y_{trg})) \cos \theta_{trg} \cos \theta_{img}}{s_{img}^2} \right) \frac{\pi}{4} (D_{opt}^2 - D_{obsc}^2). \quad (3.16)$$

The only thing that needs to be further defined in equation (3.16) are the cosine terms. The definition of these terms is solely based on the geometry between the target and optical system. Since the optical system will be tracking the target, it will always be on a line of sight with the target; therefore, θ_{img} can be assumed to be equal to zero thereby making $\cos \theta_{img}$ equal to one. Since the $\cos \theta_{trg}$ term accounts for the projected surface area of the target, by projecting the detector pixel area onto the target to determine the source area, the projected source area is already considered and the $\cos \theta_{trg}$ can also be set to one. With the terms in equation (3.16) now defined, the final representation of the target's spectral irradiance at the image plane can be determined by including the target's emissivity and all attenuation effects due to the optical system and atmosphere:

$$E_{e,trg}(\lambda, x_{img}, y_{img}) = \tau_{opt}(\lambda)\tau_{filter}(\lambda)\tau_{atm}(\lambda) \left(\frac{A_{eff}}{s_{img}^2} \right) \varepsilon(\lambda) L_e(\lambda, T(x_{trg}, y_{trg})) \quad (3.17)$$

where A_{eff} is defined by equation (3.14) and $\varepsilon(\lambda)$ is defined by equation (3.8).

3.2.4 Path Radiance. The next contributor to the overall signal is the path radiance. Spectrally, this emission comes from the absorptive regions of the atmosphere that are located between the observer and target that re-radiate photons, and it is highly dependent upon the engagement geometry which determines the amount of atmosphere between the observer and target. The values used for spectral path radiance are computed via MODTRAN, which will take into account the engagement geometry and will be fully defined in the next chapter. Since this simulation models an imaging system looking at both a target and some background, two different spectral path radiance contributions are modeled in the simulation to account for the path between the observer and the target, and the path from the observer to infinity to represent the background. These path radiances are shown in Figure 3.3. As is shown in Figure 3.3, these two path radiances, as specified by the DETEC scenario geometry, show very little difference between them, which makes sense because at a 13.9-km altitude, the missile has the majority of the atmosphere between it and

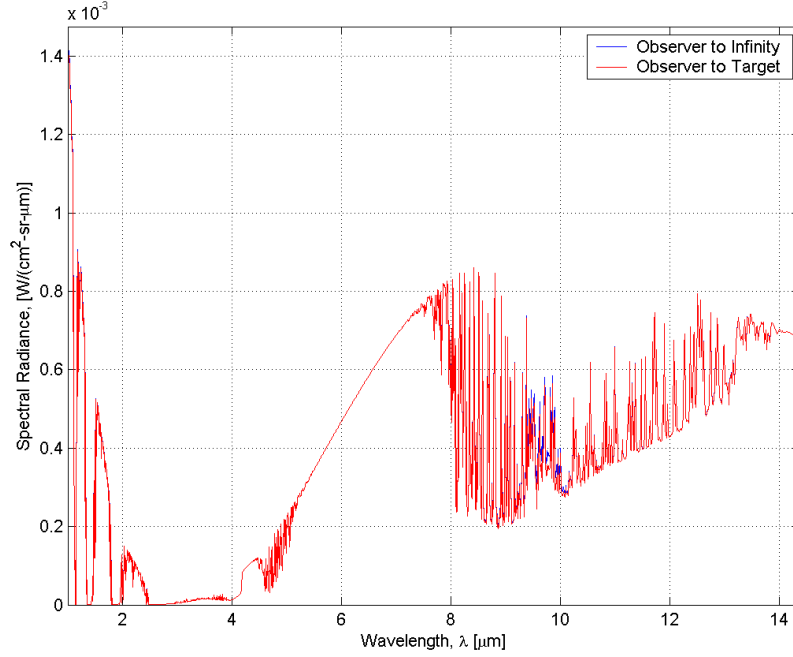


Figure 3.3: A comparison showing little difference between observer-to-target and observer-to- ∞ path radiances.

the observer. When working with MODTRAN, the spectral radiance values are referenced in wave number units [cm^{-1}], which will require a conversion to wavelength units. This conversion is achieved by:

$$L_{e,path}(\lambda) \left[\frac{W}{cm^2 \cdot sr \cdot \mu m} \right] = (10^{-4}) \nu^2 L_{e,path}(\nu) \left[\frac{W}{cm^2 \cdot sr \cdot cm^{-1}} \right] \quad (3.18)$$

where ν is the wave number.

With spectral path radiance in usable form, this contribution can be added into the simulation in terms of irradiance on the detector:

$$E_{e,path}(\lambda) = \tau_{opt}(\lambda) \tau_{filter}(\lambda) \left(\frac{L_{e,path}(\lambda)}{s_{img}^2} \right) \left[\frac{\pi}{4} (D_{opt}^2 - D_{obsc}^2) \right]. \quad (3.19)$$

3.2.5 Specular Background Reflection. Specular background reflection comes about from the geometry that exists between the observer and the target; specifically,

it represents a path radiance from the target to infinity that is reflected toward the observer and scaled by the specular reflectivity, $\rho_{spec}(\lambda)$, at an angle such that the angle of incidence equals the angle of reflection (*i.e.*, Snell's Law) with the angles referenced to the missile's surface normal. Figure 3.4 describes this scenario where the angle of reflection is the observation angle, θ_{obs} and is equal to the angle of incidence, θ_{spec} (*i.e.*, the specular angle). To account for the specular contribution to reflected radiance, MODTRAN is used again to compute the spectral path radiance that exists between the target and infinity at the specular angle. In the case of this simulation, that is the 61.6-degree observation angle. The method by which this contribution is added into the total image irradiance is:

$$E_{e,spec}(\lambda) = \tau_{opt}(\lambda)\tau_{filter}(\lambda)\tau_{atm}(\lambda) \left(\frac{\rho_{spec}(\lambda)L_{e,spec}(\lambda)}{s_{img}^2} \right) \left[\frac{\pi}{4} (D_{opt}^2 - D_{obsc}^2) \right] \quad (3.20)$$

where the specular background path radiance, $L_{e,spec}(\lambda)$, is scaled by the specular reflectance, $\rho_{spec}(\lambda)$.

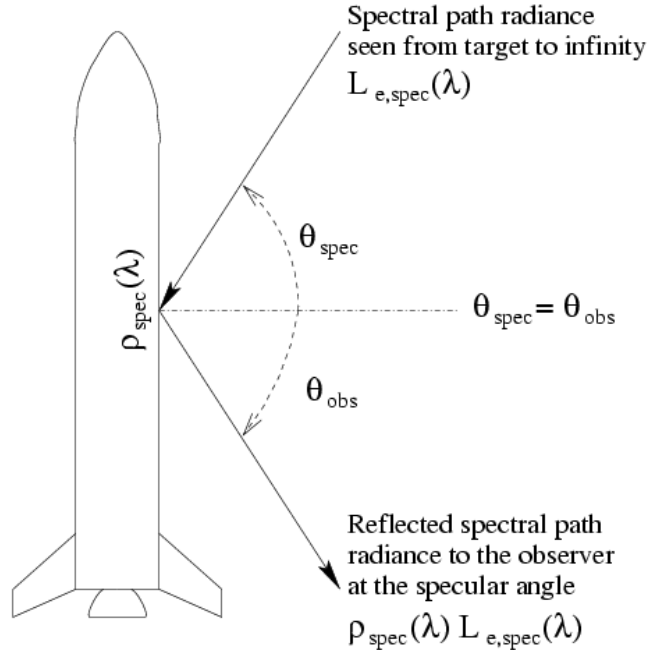


Figure 3.4: Geometry defining the radiance contribution from the reflected specular background.

3.2.6 Diffuse Background Reflection. The diffuse background reflection comes about from the 2π -sr hemispherical field of view seen by a differential area of the missile body that is also being observed by the remote observer. The irradiance from this hemisphere is reflected off of the missile body and back into this hemisphere having been scaled by the diffuse reflectivity, $\rho_{diff}(\lambda)$. Since the target body is assumed to be a Lambertian surface, this last statement is radiometrically summarized by:

$$L_{e,diff}(\lambda) = \frac{\rho_{diff}(\lambda)E_{e,bkgdf}(\lambda)}{\pi} \quad (3.21)$$

where $E_{e,bkgdf}(\lambda)$ is the incident hemispheric spectral irradiance. The remote observer will then only collect a portion of that reflected radiation, which will also be attenuated by the atmosphere. As result, the spectral irradiance that is incident on the detector will be

$$E_{e,diff}(\lambda) = \tau_{opt}(\lambda)\tau_{filter}(\lambda)\tau_{atm}(\lambda) \left(\frac{\rho_{diff}(\lambda)E_{e,bkgdf}(\lambda)}{\pi s_{img}^2} \right) \left[\frac{\pi}{4} (D_{opt}^2 - D_{obs}^2) \right] \quad (3.22)$$

However, the main difficulty in this computation is defining the spectral irradiance from the background, $E_{e,bkgdf}(\lambda)$. When considering the spectral radiance for this hemispherical source, the realization hits that it is composed of many different spectral radiance profiles describing varying elevation angles and degrees of skyshine and earthshine. To approximate this effect, the background hemisphere is divided into five horizontal spectral radiance bands whose borders are defined by the elevation angles 22.5, 67.5, 112.5, and 157.5 degrees. This description is shown in Figure 3.5. These radiance bands correspond to path radiances computed from MODTRAN to represent skyshine at 0° and 45° from zenith, horizon-shine at 90° from zenith, and earthshine at 135° and 180° from zenith.

Since the target's axis is assumed to be aligned with zenith, the radiance band borders are normal to the target, which provides symmetry to this computation that greatly simplifies it. Looking at Figure 3.5, it can be seen from the symmetry in the figure that spectral radiance bands 1 and 5 have equal areas on the hemisphere as do

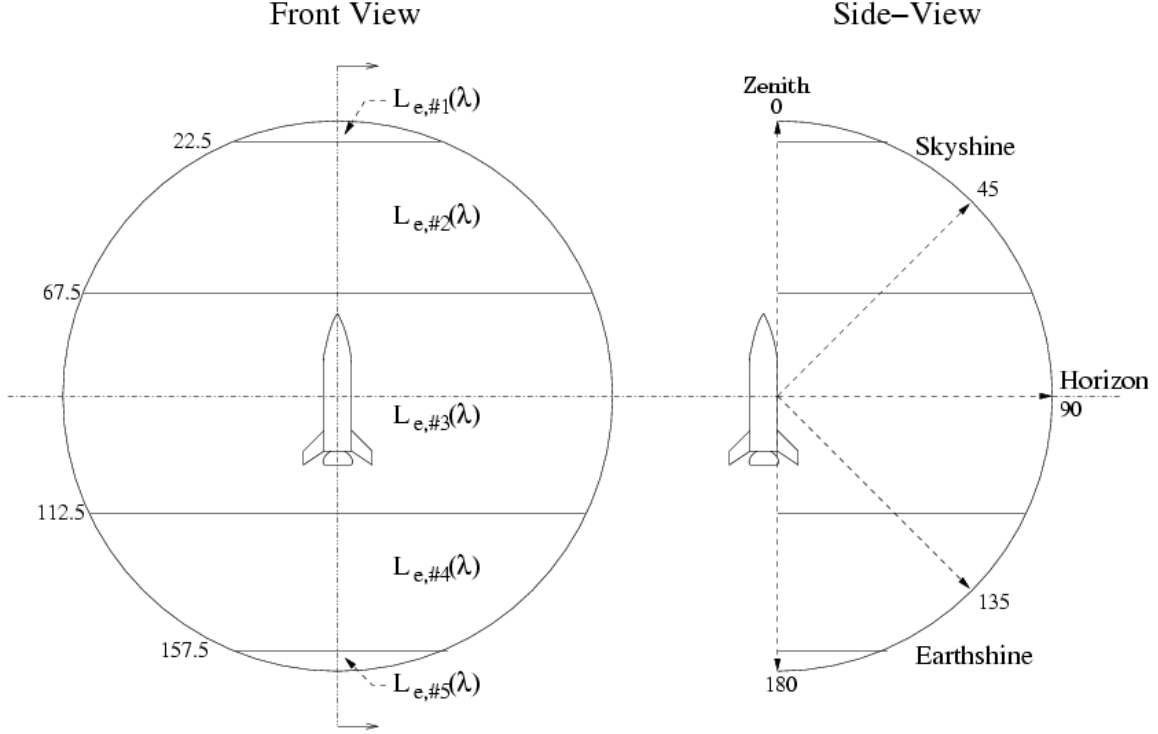


Figure 3.5: Geometry defining the diffuse-background spectral-irradiance computation.

spectral radiance bands 2 and 4. The hemispherical area of spectral radiance band 3 is divided in half by the 90-degree line. Since the spectral radiance in each band is assumed constant across the whole band, the spectral irradiance from each band is [16]:

$$E_{e,band}(\lambda) = L_{e,band}(\lambda) \int_0^\pi \int_{\theta_1}^{\theta_2} \cos \theta_d \sin \theta_d d\theta_d d\phi = \pi L_{e,band}(\lambda) (\sin^2 \theta_2 - \sin^2 \theta_1) \quad (3.23)$$

where θ_1 and θ_2 are the angles of adjacent band borders. In computing the integral in equation (3.23), the solid angle of the hemisphere corresponding to bands 1 and 5 is approximately 0.23 [sr]. The solid angle for bands 2 and 4 is approximately 1.11 [sr]. The solid angle for band 3 is approximately 0.46 [sr]. From these values, the diffuse

background irradiance on the target from the entire hemisphere can be computed by:

$$E_{e,bkgdf}(\lambda) = 0.23L_{e,\#1}(\lambda) + 1.11L_{e,\#2}(\lambda) + 0.46L_{e,\#3}(\lambda) + 1.11L_{e,\#4}(\lambda) + 0.23L_{e,\#5}(\lambda). \quad (3.24)$$

The validity of this equation is verified by letting all five spectral radiance bands have the same value such that the whole hemisphere has one spectral radiance value. The resulting spectral irradiance value should equal the spectral radiance multiplied by π , which is the expected result for a diffuse, Lambertian surface [5:47].

3.2.7 Total Spectral Irradiance at the Image Plane. With all the radiometric sources defined and quantified, a statement can finally be made about the expected spectral irradiance at the image plane of the optical system. The total spectral irradiance is simply the sum of equations (3.17), (3.19), (3.20), and (3.22):

$$E_{e,tot}(\lambda, x_{img}, y_{img}) = E_{e,trg}(\lambda, x_{img}, y_{img}) + E_{e,spec}(\lambda) + E_{e,diff}(\lambda) + E_{e,path}(\lambda). \quad (3.25)$$

3.3 Modeling the Modulation Transfer Functions

With a radiometrically correct ideal image in the focal plane, the simulation must now account for the phenomena that blurs this ideal image. The two chief blurring agents are the optical system and atmospheric turbulence. Two other blurring agents, namely the FPA pixel footprint and sampling footprint, which are inherent to the detection system, also contribute. In order to apply all of these blurring effects, they must be represented as MTFs. With the application of all these MTFs, the result is a realistic image of the target recorded by the detector; therefore, this section will present how these quantities are determined.

3.3.1 Optical MTF. The first MTF considered is the optical MTF for the unaberrated optical system. For this thesis, the method of computation will be the PSF method discussed in section 2.2.2.3. In the computation, the system parameters that are used in defining the MTF include:

- The size and shape of the optical system's aperture.
- The size and shape of any central obscurations in the aperture.
- The effective focal length of the optical system.
- The wavelength of the optical radiation being propagated.

The method of computation is outlined in Goodman [10:142] for the computation of complex apertures. For this thesis, a circular aperture with a circular central obscuration is only considered. The first step is to spatially define this aperture, $P(x_{ap}, y_{ap})$, by creating a matrix and letting it contain values zero through one. A zero indicates no transmission, and one indicates total transmission through any given region. With the aperture defined, compute the Fourier transform of $P(x_{ap}, y_{ap})$ and square it to yield an intensity PSF. Then, perform the Fourier transform on the intensity PSF and take its modulus to yield an unnormalized MTF. The optical MTF used in the simulation requires the MTF to be normalized, so using the value of the unnormalized MTF at zero spatial frequency as the normalizing term will yield the desired result. This description is summarized by:

$$MTF_{Un-Norm}(f_{X,img}, f_{Y,img}) = |\mathcal{FF} \{ |\mathcal{FF} \{ P(x_{ap}, y_{ap}) \} |^2 \} | \quad (3.26)$$

$$MTF_{opt}(f_{X,img}, f_{Y,img}) = \frac{MTF_{Un-Norm}(f_{X,img}, f_{Y,img})}{MTF_{Un-Norm}(0, 0)} \quad (3.27)$$

As a MATLAB implementation note, the defined aperture within the matrix must not fill more than half of the matrix size in order to prevent aliasing in the Fourier transform computation. Example results of this calculation is shown in Figure 3.6.

3.3.1.1 Analyzing the Optical MTF. Some qualitative analysis is required to understand the impacts that the optical MTF has on the overall optical system. Looking at Figure 3.6 shows how the optical MTF varies with wavelength for an optical system defined with the following parameters: aperture diameter = 0.6 m, central obscuration = 0.2 m, and $F/\# = 10$. The exactness of these MTFs can be confirmed by looking at the plotted spatial cutoff frequencies and comparing them

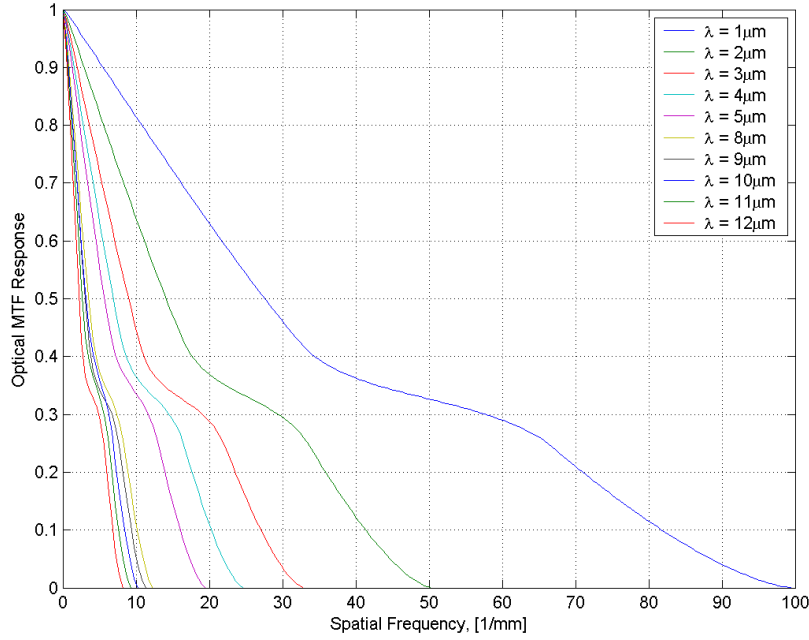


Figure 3.6: Optical MTFs for various IR wavelengths. Optic parameters: a 0.6 m circular aperture with 0.2 m circular obscuration, $F/\# = 10$.

to equation (2.29). The first observation concerns how the cutoff spatial frequency varies with wavelength. The practical implication of cutoff spatial frequency is that it is the point at which the image contrast goes to zero. Shorter wavelengths have higher cutoff frequencies than longer wavelengths. The main conclusion that comes from Figure 3.6 is that, for an object emitting IR radiation and being imaged, the irradiance differences in finer spatial features on the object will be detected when those features emit at shorter wavelengths as opposed to longer ones. At longer wavelengths, the irradiance of those finer features will produce an average irradiance value that creates a blurred effect in the image. As a note, the flattened portion in the MTFs at approximately 0.3 is due to the central obscuration.

3.3.2 Detector MTF. When attempting to quantify the effects that an FPA pixel has on a scene, one must realize that there is an inherent spatial averaging of scene irradiance that takes places due to the detector pixel's finite size [2:31]. This

averaging takes place due to the pixel's inability to distinguish between two different sources that are within its instantaneous field of view (IFOV). To perform this spatial averaging, the scene irradiance must be convolved with the pixel footprint which can be modeled as a square aperture of size, w_{det}^2 . As a result, this square aperture can be described by its Fourier transform to provide an MTF.

$$MTF_{det} = \left| \frac{\sin(\pi f_X w_{det})}{\pi f_X w_{det}} \right| \left| \frac{\sin(\pi f_Y w_{det})}{\pi f_Y w_{det}} \right| \quad (3.28)$$

This MTF experiences a zero at $f_X, f_Y = \frac{1}{w_{det}}$ [2:34], which is due to one line pair of spatial frequency aligning just right to produce a zero modulation depth. This effect is demonstrated in Figure 3.7. Figure 3.8 shows one dimension of the detector MTF.

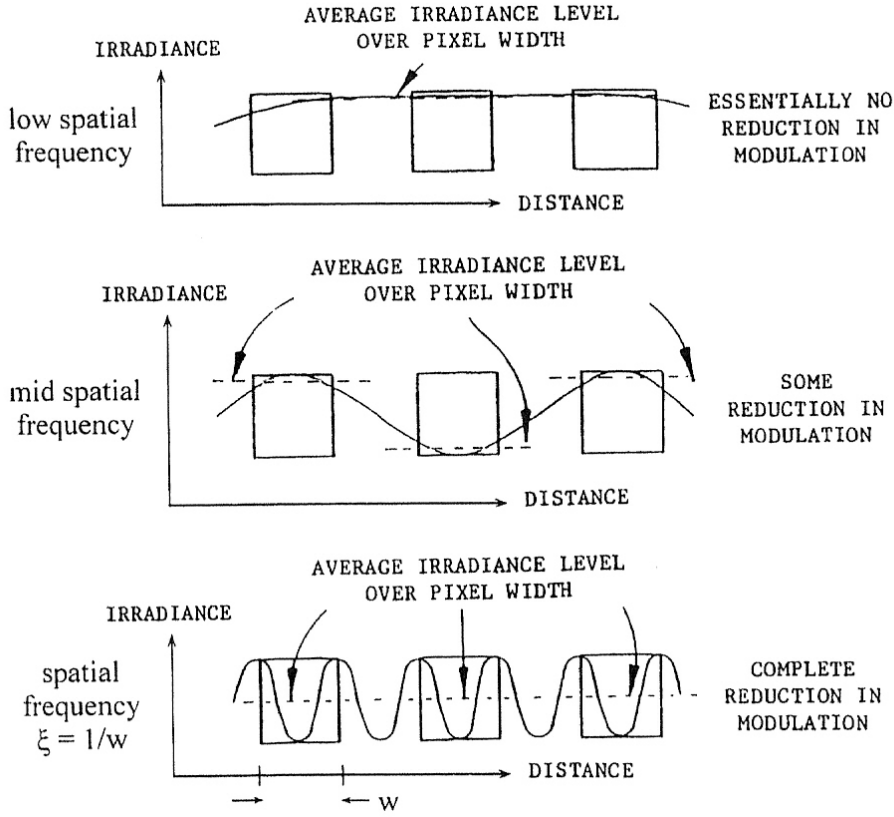


Figure 3.7: At the detector spatial cutoff frequency $f_X = 1/w$, the modulation depth is zero. [2:34].

For this thesis, the physical dimension of the pixel is $25 \mu m$. This choice was based

on a mercury cadmium telluride (HgCdTe or MCT) FPA datasheet specification from DRS Infrared Technologies [7]. This value is in the mid-range of pixel sizes seen on different datasheets, which vary from 19 - 60 μm with the majority being between 20 - 30 μm [8, 11, 14, 22].

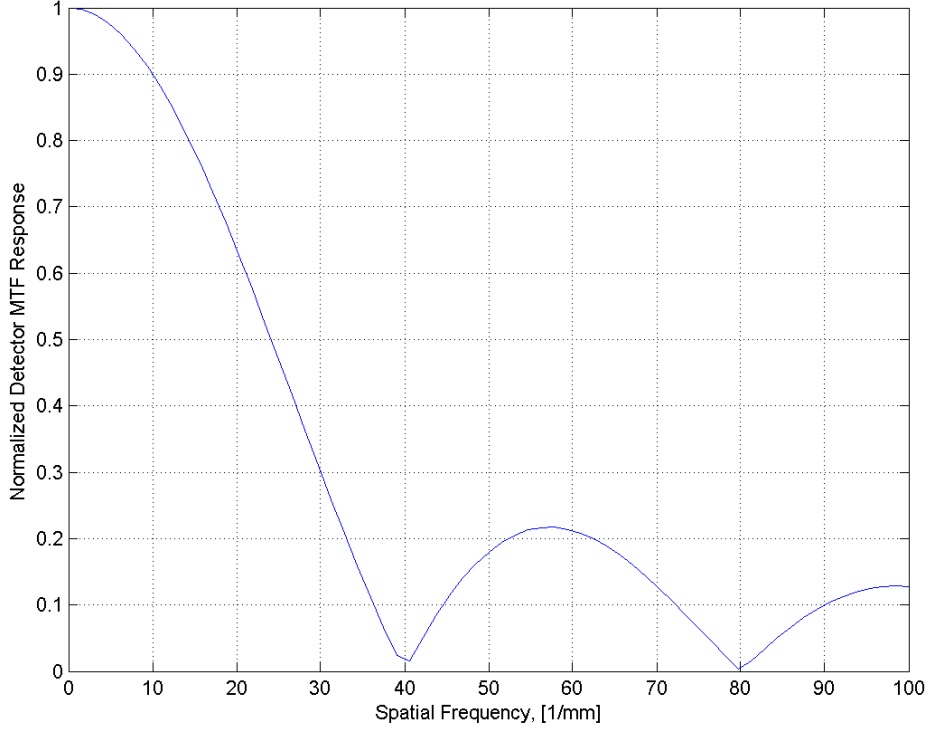


Figure 3.8: MTF of a 25- μm FPA pixel.

3.3.3 Sampling MTF. The sampling MTF attempts to account for the FPA sampling the irradiance scene. A successful accounting proves to be more difficult since sampled-imaging systems are shift variant [2:41]. This fact is easily observed in Figure 3.9 which shows that the measured irradiance value can vary depending upon how it is sampled. A perfect alignment on the FPA detectors will yield a higher measurement than if the irradiance is straddled and being measured by two sets of detectors. In order to invoke shift invariance onto this problem, the sampling MTF can be defined in similar terms as the detector MTF by defining a sampling footprint. This footprint is defined by the sampling interval, x_{samp} , which equals the distance between pixel centers. The irradiance scene can then be spatially averaged

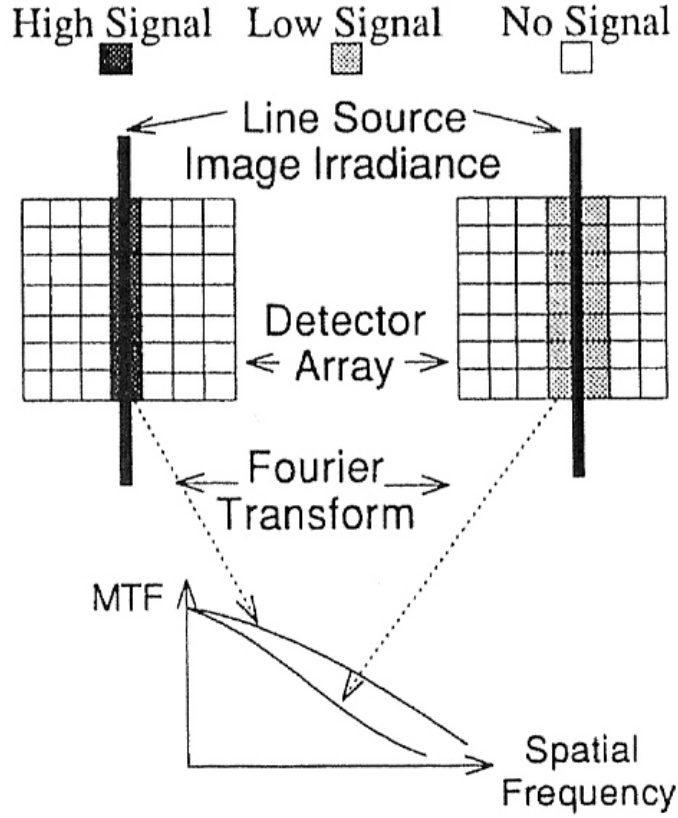


Figure 3.9: Demonstration of the shift variance of a sampled, image-forming system. [2:41].

by a rectangular footprint of size $x_{samp} \times y_{samp}$, which results in a similar MTF as described by equation (3.28) [2:42]:

$$MTF_{samp} = \left| \frac{\sin(\pi f_X x_{samp})}{\pi f_X x_{samp}} \right| \left| \frac{\sin(\pi f_Y y_{samp})}{\pi f_Y y_{samp}} \right|. \quad (3.29)$$

For this thesis, the modeled FPA will have a 100% fill factor, which makes $x_{samp} = y_{samp} = w_{det}$. As a result, the sampling MTF equals the detector MTF.

3.3.4 Atmospheric MTF. The atmospheric MTF attempts to account for turbulence effects due to the atmosphere which randomly refracts optical radiation as it propagates through the atmosphere. One fundamental parameter used in creating the atmospheric MTF that should be discussed here is the atmospheric coherence

diameter, r_0 . r_0 describes the effective aperture of the atmosphere under which a beam of light retains coherence. The practical impact that this value has on spatial frequency in this simulation is that this parameter determines the limits of resolution in the optical system. Because of this parameter, any aperture size greater than r_0 will not yield greater resolution in the image. In this simulation, the atmospheric MTF is not explicitly computed; Becky Beauchamp, a DIAT team member working atmospheric issues, provided long-term atmospheric MTFs for many different wavelengths with an $r_0 = 0.25$ m. As a result, the atmospheric MTF will be the limiting MTF in the simulation, given that the simulated optic diameter is 0.6 m; this will be shown in the next section.

3.3.5 System MTF. With the MTFs defined for each component in the optical system, the overall system MTF can be computed by multiplying the optical, detector, sampling, and atmospheric MTFs together. Figure 3.10 shows the system MTF and should be compared to Figures 3.6 and 3.8 to see how it relates to the other MTFs.

To apply the imaging effects of the optical system onto the ideal spectral irradiance that is incident on the detector, the following mathematical operation is required:

$$E_{e,img}(\lambda, x_{img}, y_{img}) = \mathcal{F}^{-1} \mathcal{F}^{-1} \{ MTF_{sys}(f_{X,img}, f_{Y,img}) \times \mathcal{F} \mathcal{F} \{ E_{e,tot}(\lambda, x_{img}, y_{img}) \} \}. \quad (3.30)$$

3.4 Modeling the Detector Response

At this stage of the simulation, all optical radiation sources have contributed to produce a blurred irradiance due to the optical system onto the FPA. All that is left is for the FPA to absorb the incident photons and produce a measurable current. This section will describe how the IR camera simulation takes the incident irradiance

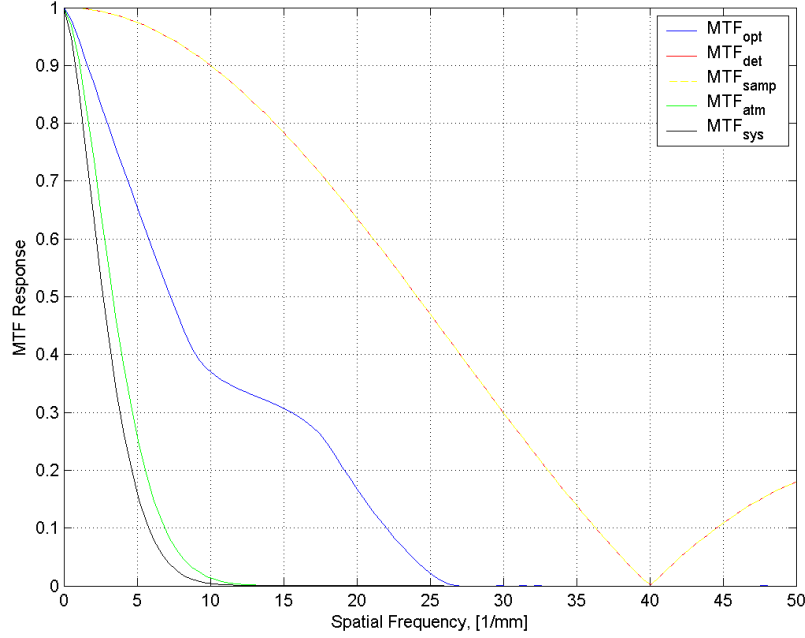


Figure 3.10: Overall system MTF which is composed of the optical, detector, sampling, atmospheric MTFs.

image and models the response from the photovoltaic detector, which could be made from either InSb or MCT.

3.4.1 Computing the Detector Signal. Up to this point in the simulation, all the radiometric values have been expressed in terms of radiant units. Since a photovoltaic detector is a photon detector, the radiant radiometric values need to be converted to photon quantities. The first step in this conversion is to express $E_{e,img}(x_{img}, y_{img}, \lambda)$ in terms of radiant spectral flux. At this stage, the simulation is still working with the spectral irradiance image, which has yet to be integrated across an FPA detector pixel, so using the MATLAB representation discussed in section 3.1.2 and equation (3.2) and in section 3.2.7 and equation (3.25) to represent the physical spacing between adjacent image values, the radiant spectral flux of the image is then:

$$\phi_{e,img}(x_{img}, y_{img}, \lambda) = E_{e,img}(x_{img}, y_{img}, \lambda) \Delta x_{img}^2 \quad (3.31)$$

where Δx_{img}^2 represents the area in the image plane that $E_{e,img}(x_{i,img}, y_{j,img}, \lambda)$ is a constant value. The conversion to photon flux is achieved by the application of equation (2.1):

$$\phi_{q,img}(x_{img}, y_{img}, \lambda) = \frac{\lambda}{hc} \phi_{e,img}(x_{img}, y_{img}, \lambda). \quad (3.32)$$

With the image expressed in terms of spectral photon flux, the signal can now be integrated over a physical detector size, w_{det}^2 , in order to represent what is collected by an actual FPA pixel. This integration is achieved in MATLAB by first defining pixel boundaries across the image by normalizing the image's physical scales, x_{img} and y_{img} , by w_{det} , which is seen in Figure 3.11. These boundaries are represented by whole numbers in the array. The next step is to sum up all the photon spectral flux

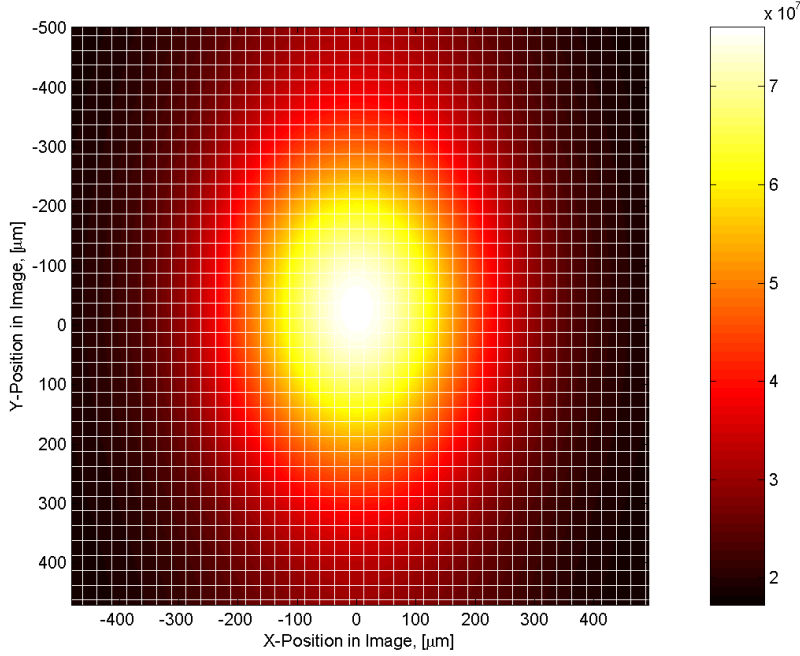


Figure 3.11: Photon flux distribution across the MCT FPA showing pixel boundaries in the 8.5-to-12- μm waveband, 0.125 msec integration time. Simulated source reflectivities: $\rho_{spec} = 0.2$, $\rho_{diff} = 0.3$.

image values, $\phi_{q,img}(x_{img}, y_{img}, \lambda)$, that lie in between adjacent whole numbers in the x- and y-directions across the entire image. The result of this operation is the FPA image, which is shown in Figure 3.12 in terms of total photon flux on the FPA pixel.

This spectral photon flux is then used to determine the amount of spectral current

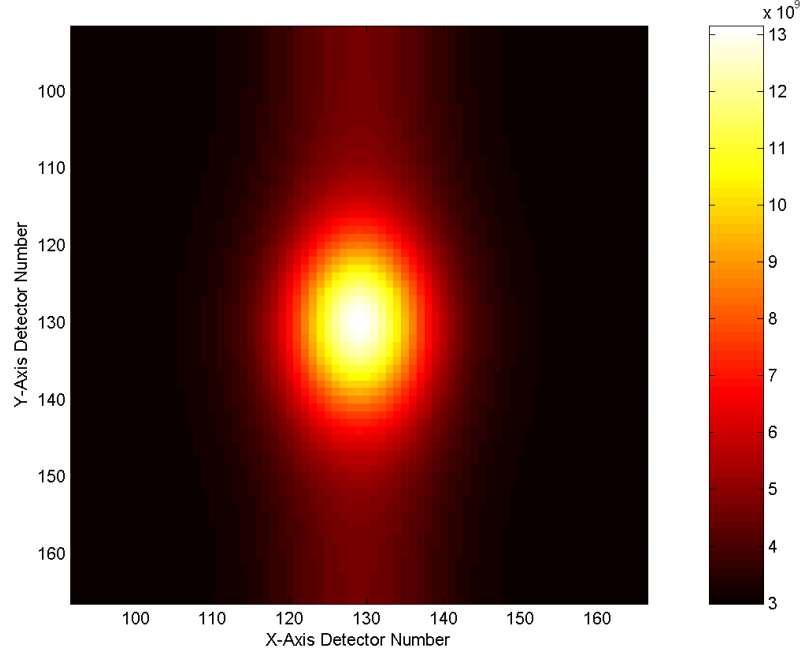


Figure 3.12: Spatially-integrated photon flux incident on each MCT FPA pixel in the 8.5-to-12- μm waveband, 0.125 msec integration time. Simulated source reflectivities: $\rho_{spec} = 0.2$, $\rho_{diff} = 0.3$.

generated in the detector, which is determined by the photocurrent equation, (2.33). Since the computed detector currents are spectral quantities, the whole simulation must be repeated for every wavelength specified in the waveband, from computing new spectral irradiances at the next wavelength and applying the next spectral MTF, to integrating this new image to an FPA image. For each iteration of the simulation, the FPA spectral current will be summed with all the previous iterations, which will yield a total current over a waveband. Mathematically, this spectral integration is represented discretely by:

$$i_{FPA} = \sum_{m=1}^{j-1} i_{m,FPA}(\lambda) \Delta\lambda_m \quad \text{where} \quad \Delta\lambda_m = \lambda_{m+1} - \lambda_m \quad (3.33)$$

where $i_{m,FPA}(\lambda)$ is the spectral current.

With a total current defined, a signal, quantified by the number of electrons generated in the detector, can be determined by simply dividing the current by the charge of an electron, q , and multiplying it by the integration time, τ .

$$S_{FPA} = \frac{i_{FPA}\tau}{q} \quad (3.34)$$

This signal is now the focus of this thesis because it will be used to show how detectable the target will be with respect to the detection system's noises discussed in section 3.4.3, but more importantly, it provides the comparison signal by which temperature estimates on the target body will be made as will be discussed in Chapter IV. The detectability will be based on the computation of the SNR.

$$SNR = \frac{S_{FPA}}{N_{total}} \quad (3.35)$$

where N_{total} is the total number of detection system noise electrons as defined in section 3.4.3.

3.4.2 Detector Materials. The choice of detector materials to be modeled was based on the desire to explore a wide range of wavelengths. Looking at the possibilities, the best choices were InSb and MCT, since they are both common commercially-used detector materials; plus, between the two, they cover a wide range of wavelengths. InSb is suited to the 3-to-5- μm band; while, MCT covers 8 to 12 μm . Since MCT is a very configurable material depending upon the Hg-Cd mole fraction, the specific type of MCT used for this simulation is $Hg_{0.2}Cd_{0.8}Te$.

Based on the discussion in section 2.2.3.2, the two most important factors in determining a detector's suitability are its cutoff wavelength, λ_c , and quantum efficiency, η . For this simulation, these detector materials are modeled as being cooled to 77 K, which produces $\lambda_{c,InSb} = 5.5 \mu m$ [5:94] and $\lambda_{c,MCT} = 13.78 \mu m$ [19:682]. As for the quantum efficiency, defining it as a spectral quantity was preferred for the sake of model fidelity. The original goal was to find complex indices of refraction for

both materials and use equations (2.35) and (2.36) to calculate the quantum efficiencies. Such values are available for MCT from Polk at 80 K [19:682]. These values were then interpolated to the proper wavelength values to make them useful for this simulation. The quantum efficiency for MCT is shown in Figure 3.13. Overall, the

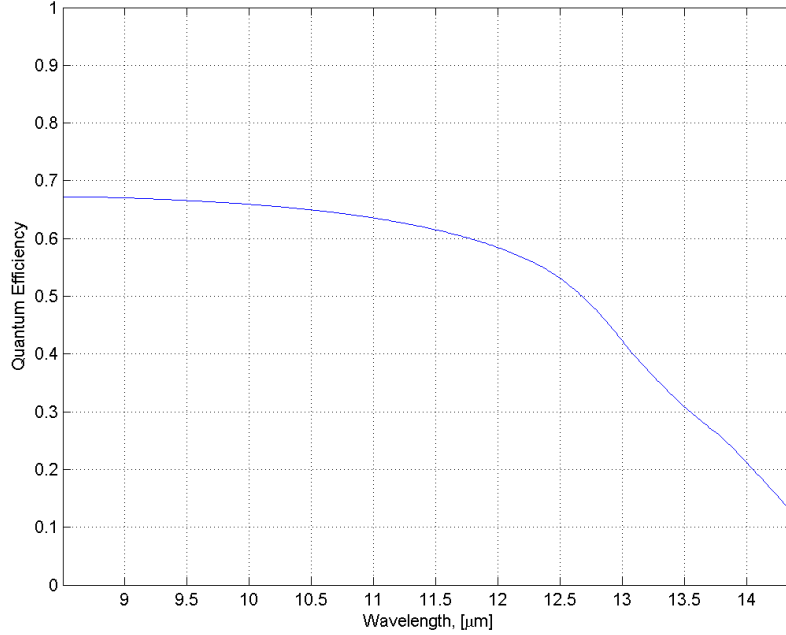


Figure 3.13: Quantum efficiency of $\text{Hg}_{0.2}\text{Cd}_{0.8}\text{Te}$ at 80 K with a measured cutoff wavelength, λ_c , of $13.78 \mu\text{m}$.

spectral quantum efficiency is comparable to the 65% specified by Dereniak [5:94]. As for InSb, no extinction coefficient, k , data could be found at 77K. However, the real index-of-refraction data from Palik [18:495] could be used. The only other way found to define InSb's absorption coefficient spectrally was through [5:90]:

$$a = a_0 \sqrt{h\nu - \mathcal{E}_g} + a'_0 \quad \text{for} \quad h\nu > \mathcal{E}_g \quad (3.36)$$

$$a = a'_0 \exp\left(\frac{h\nu - \mathcal{E}_g}{kt}\right) \quad \text{for} \quad h\nu < \mathcal{E}_g \quad (3.37)$$

where $a_0 = 1.9 \times 10^4 \text{ cm}^{-1}$ and $a'_0 = 800 \text{ cm}^{-1}$ for InSb. The quantum efficiency computed for InSb is shown in Figure 3.14. It should be noted that these quantum

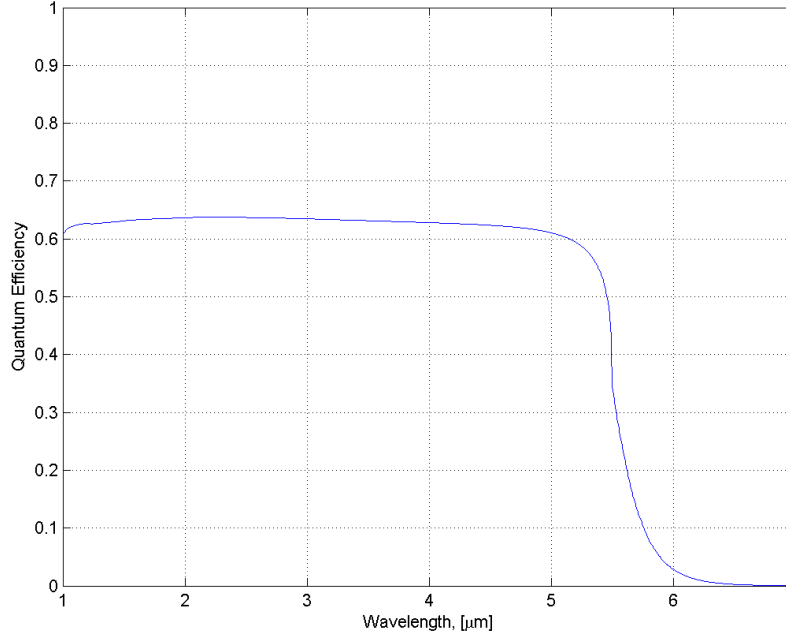


Figure 3.14: Quantum efficiency of InSb at 77 K with a cutoff wavelength, λ_c , of $5.5 \mu\text{m}$.

efficiencies are only for the bare material. No anti-reflective coatings, which would increase the quantum efficiency, are assumed to be applied.

3.4.3 Noise Sources. In the continued effort to attain the required fidelity in this simulation, consideration of noise sources in the detector and associated ROIC are required. The noises are caused by random fluctuations in charge within the detector and ROIC, which may be perceived as part of the true signal. As a result, the total noise of the system determines the lower limit of a detector's sensitivity. To be able to quantify inherently random noises sources, their variances must be determined. Dereniak provides a justification through the use of the power spectrum density that the variances can be quantified into root-mean-squared (rms) values [5:154]. As a result of this definition, independent noise sources must be added in quadrature to get the total detector noise. For this thesis, the following detector noises sources were considered: photon (N_{photon}), dark current (N_{dark}), and Johnson (N_{Johnson}), while the following read noises were considered: transfer inefficiency (N_{trsfrr}), fat zero

($N_{FatZero}$), kTC (N_{kTC}), and preamplifier (N_{preamp}). From these noise sources, the total detection system noise in the simulation is defined as:

$$N_{total} = \sqrt{N_{photon}^2 + N_{dark}^2 + N_{Johnson}^2 + N_{trsf}^2 + N_{FatZero}^2 + N_{kTC}^2 + N_{preamp}^2} \quad (3.38)$$

Descriptions of these noises are in the following sections. As a note, these noises are computed and quantified in units of number of electrons [e^-]. Also, noise expressions are usually expressed in terms of the noise-equivalent bandwidth, but since this thesis focuses on integration time as an analysis parameter, all the noise terms will use the definition of noise-equivalent bandwidth as defined by equation (2.39) so that they are in terms of integration time.

3.4.3.1 Photon Noise. Photon noise is a result of photons from the source arriving at the detector at random times. Since arrival times can be described as Poisson processes, the noise value can be expressed as the square root of the mean number of photons. This noise will manifest itself as a shot noise because these photons will generate a photocurrent that will flow across the photovoltaic depletion region [5:175]. The photon noise can be expressed as:

$$N_{photon} = \sqrt{\eta E_{q, det} A_d \tau} \quad [e^-]. \quad (3.39)$$

3.4.3.2 Dark Current Noise. Another shot noise source in photovoltaic detectors is dark current. This current represents the current flowing in the detector when no optical radiation is incident upon it. The amount of dark current in a detector is controlled by how the semiconductor is doped and how the photovoltaic device is biased.

To estimate the dark current, Janesick [12:622] provides a datasheet-friendly method of computation. Using ambient-temperature testing information from a de-

tector datasheet, the following constant is computed:

$$C = \frac{D_{FM} A_d}{q T_{amb}^{1.5} e^{-E_{g,amb}/(2k_B T_{amb})}} \quad (3.40)$$

where D_{FM} is a dark current density figure of merit at some ambient-testing temperature, T_{amb} , A_d is the area of the detector pixel, and $E_{g,amb}$ is the bandgap energy of the detector material at T_{amb} . This value is then substituted into [12:622]:

$$i_{dark} = C T_{opr}^{1.5} e^{-E_{g,opr}/(2k_B T_{opr})} \quad (3.41)$$

where T_{opr} is the operating temperature of the detector material and $E_{g,opr}$ is the bandgap energy of the detector material at T_{opr} . In this form, the units of the dark current are $[e^-/sec]$. At which, the shot noise from the dark current is [12:626]:

$$N_{dark} = \sqrt{i_{dark} \tau} \quad [e^-] \quad (3.42)$$

3.4.3.3 Johnson Noise. Johnson noise is due to fluctuations caused by thermal motion of charge carriers in a resistive element [5:168]. This noise is computed with

$$N_{Johnson} = \sqrt{\frac{2k_B T_{opr} \tau}{q^2 R_{det}}} \quad [e^-] \quad (3.43)$$

where R_{det} is the resistance of the detector. Resistance-area (RA) products, when multiplied by the detector area, can be used to compute R_{det} . The RA value chosen for InSb at an operating temperature of 77 K is $10^7 \Omega - cm^2$ [5:308]. For $Hg_{0.2}Cd_{0.8}Te$, the RA value chosen, based on Figure 3.15, is $15 \Omega - cm^2$.

3.4.3.4 Transfer Inefficiency Noise. In charge-coupled device (CCD) technology, the transfer inefficiency noise characterizes the amount of charge randomly removed from a signal as it leaves a potential well or the amount of charge randomly added to a signal as it enters a potential well. Charge transfer efficiency (CTE) is a parameter used to quantify how well a CCD can transfer the charge from one

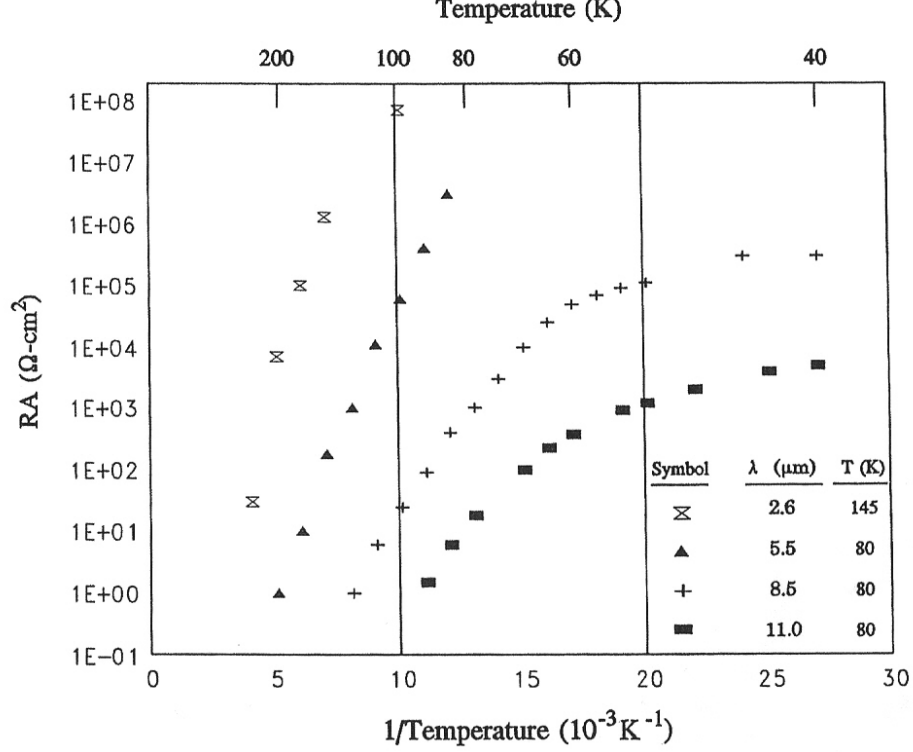


Figure 3.15: Plots of RA products for various β -valued $\text{Hg}_{1-\beta}\text{Cd}_\beta\text{Te}$ detectors. Note, the $\text{Hg}_{0.2}\text{Cd}_{0.8}\text{Te}$ detector variant corresponds to darkened rectangle symbol. [5:323].

potential well to the next. A common value for CTE, which is used in the simulation, is 0.99999 [12:387]. This noise can be quantified by [12:656]:

$$N_{trsf r} = \sqrt{2(1 - CTE)N_{pixel}S_{pixel}} \quad [e^-] \quad (3.44)$$

where N_{pixel} is the number of detector pixels in one dimension and S_{pixel} is the signal in (e^-) in a specific pixel. The value chosen for N_{pixel} is 256 and is based on various IR FPA datasheets used in military applications [14, 22].

3.4.3.5 Fat Zero Noise. Fat zero noise results from an electrical fat zero randomly injecting charge into a potential well. Electrical fat zeros are designed into a CCD array to fill electron-trapping sites in the potential well and allow for more

efficient charge transfer [12:654]. The following equation quantifies this noise [12:655]:

$$N_{FatZero} = \sqrt{\frac{k_B T_{opr} C_I}{q^2}} [e^-] \quad (3.45)$$

where C_I is the input capacitance to an input metal-oxide semiconductor field-effect transistor (MOSFET) on the preamplifier in the ROIC. Janesick lists a value of 0.01 pF as a typical order of magnitude for C_I [12:515].

3.4.3.6 kTC Noise. kTC noise is associated with the reset circuit on the CCD preamplifier. It results from thermal noise generated by the channel resistance of the reset MOSFET. This noise is quantified by [12:538]:

$$N_{kTC} = \sqrt{\frac{k_B T_{opr} C_S}{q^2}} [e^-] \quad (3.46)$$

where C_S is the output capacitance to an output MOSFET on the preamplifier on the ROIC. Janesick lists a value of 0.1 pF as a typical order of magnitude for C_S [12:538].

3.4.3.7 Preamplifier Noise. The preamplifier noise is associated with the MOSFET transconductance of the preamplifier. The preamplifier noise is defined by [17]:

$$N_{preamp} = \frac{C_S}{q} \sqrt{\frac{4k_B T_{opr}}{3g_m \tau}} \quad (3.47)$$

where g_m is the MOSFET transconductance. Janesick lists a value of $5 \times 10^{-4} \text{ } \mathcal{U}$ as a typical order of magnitude for g_m [12:497].

3.5 Summary

With the IR camera simulation completely developed, it now has the capability to start answering questions for the DIAT program. These questions will be addressed in the next chapter as the IR camera simulation is used as an analysis tool to identify the critical parameters in measuring irradiance from the ABL.

IV. Temperature and SNR Analyses

With the IR camera simulation fully developed, it can now be employed to provide initial answers that will aid in the development of DIAT. This chapter details the analysis that was conducted to initially look at how the SNR of the target changes with respect to four variables: the target's specular and diffuse reflectivities, integration time, and the choice of waveband in which to measure the irradiance. However, this analysis took on greater significance with the realization that using the generated data, a temperature estimate may be produced. Therefore, this chapter will document the scenario and model inputs from which the results came, display and discuss the results of the SNR study, and document the initial method of estimating temperature and the results that it generated.

4.1 Analysis Scenario and Simulation Parameter Definitions

For the initial analysis scenario that was defined by DETEC, a missile is launched from Vandenberg AFB California. At a specific instant of time, the ABL is lasing the missile, which is at an altitude of 13.9 km with its axis pointing at zenith, and an observer, who is located on the ocean at a ground range of 7.5 km from the missile, is looking at the laser-induced hot spot on the missile at a 61.6-degree angle from horizontal. The ABL, missile, and observer share the same vertical plane. The distance between the target and missile is a slant range of 15.8 km. From this information, parameters used in the simulation like the background spectral radiances and atmospheric transmission can be estimated by PLEXUS/MODTRAN.

To create these transmission and radiance values, PLEXUS requires specific geometry, time, and location information. So for this analysis, inputs into PLEXUS were defined as:

- Date: July 14, 2007
- Time: Noon, local time
- Aerosol environment: Maritime

- Clear day with a visibility of 23 km and no significant weather in the past 24 hours
- Observer is looking at the missile with an azimuth of 40 degrees from due north
- Observer altitude: 0 km (sea level)
- Slant range: 15.8 km
- Observation angle: 28.2 degrees from zenith

From these data inputs, PLEXUS generated the atmospheric transmission function shown in Figure 4.1. This figure shows that there is substantial atmospheric

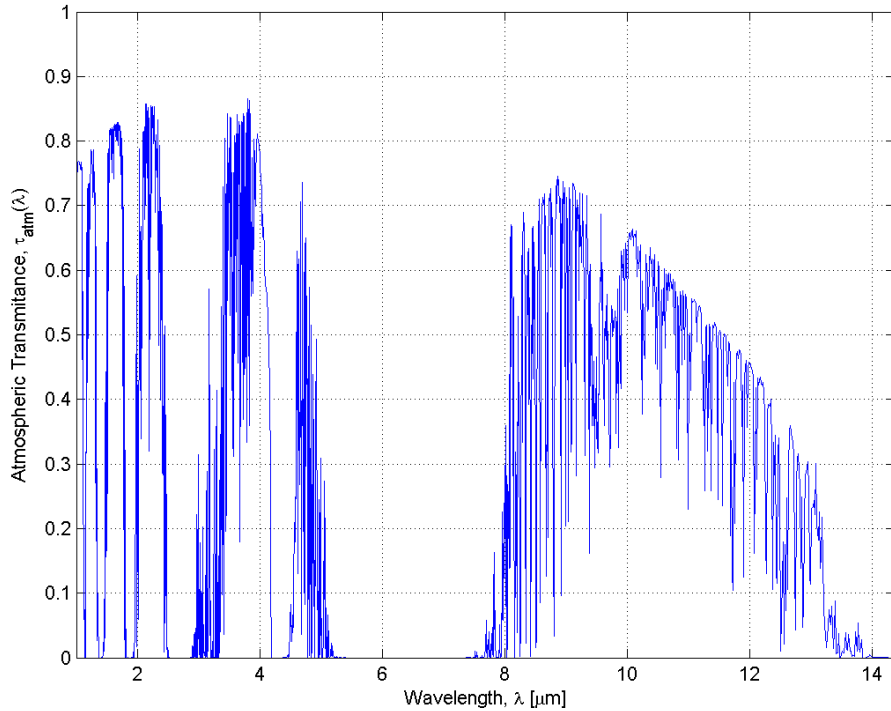


Figure 4.1: Atmospheric transmission function defined for a 15.8-km slant range at Vandenberg AFB on July 14, 2007 at 12:00 local time..

absorption taking place given the above parameters. The best wavebands to simulate will have the highest atmospheric transmission values. As a result of this data, the 3.4-4.2- μm waveband, which has an average atmospheric transmission of 64%, is the best choice for the InSb FPA. The best waveband choice for the MCT FPA is 8.5-12

μm , and its average atmospheric transmission is 54%. Due to these waveband choices, the spectral filter transmission functions for each detector type will be set to their respective wavebands and have a 95% transmittance; any wavelengths outside each waveband will have zero transmittance.

Since the IR simulation produces a detector image of collected energy from the missile body and the surrounding background, background spectral radiance contributions must be added to account for path radiance emissions between the observer and the target, and from the observer to infinity, which is seen on both sides of the missile body. These contributions are shown in Figure 4.2. As shown in Figure 4.2,

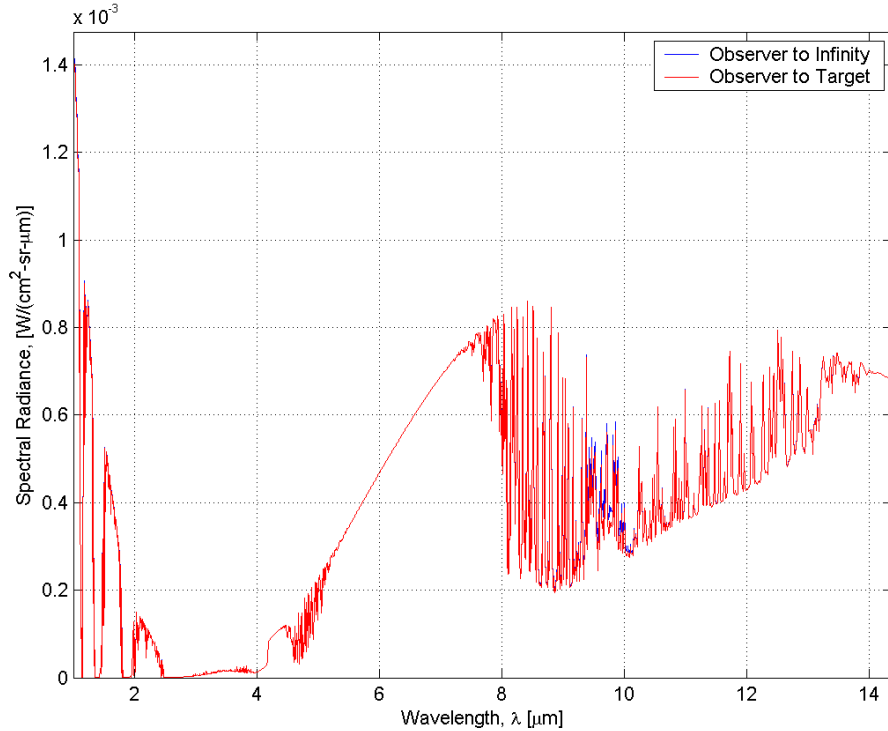


Figure 4.2: Observer-to-target and observer-to-infinity spectral path radiances used to provide background sources.

very little difference exists between the two spectral path radiances. This lack of difference is due to the target's 13.9-km altitude and the fact that most of atmosphere is between the observer and target. The only difference occurs in the 8.5-10.1- μm

waveband, which according to Lt Col Steven Fiorino, an AFIT professor also working on DIAT, is a spectral path radiance contribution from ozone.

The next spectral radiance input is the specular reflectance source. This source requires slightly different PLEXUS input parameters because the target becomes the “observer”. Specifically, the IR simulation must account for background spectral radiance contributions that are incident onto the target at its current position, so changes in the observer’s altitude, azimuth angle, observation angle, and slant range are required in PLEXUS. For the specular reflectance case, the observer’s parameters become:

- Altitude: 13.9 km
- Azimuth angle: -140 degrees from due north
- Observation angle: 28.4 degrees from zenith (specular angle)
- Slant range: Infinity

The resulting specular reflectance spectral radiance input, which will be scaled by $\rho_{spec}(\lambda)$, is shown in Figure 4.3. Looking at the wavebands used in the simulation, Figure 4.3 shows an almost insignificant contribution made in the 3.4-4.2- μm waveband and a large spectral radiance contribution from ozone in the 8.5-12- μm waveband.

The last spectral-source input that must be addressed is the diffuse reflectance source. As discussed in section 3.2.6, this input comes from the spectral radiances observed at angles 0, 45, 90, 135 and 180 degrees from zenith at the target’s position. Figure 4.4 shows how each of these spectral radiances compare with each other. The spectral radiances at zero (blue line) and 45 (green line) degrees, which represent skyshine, are very similar to Figure 4.3 in that there is an almost insignificant contribution in the 3.4-4.2- μm waveband and a large spectral radiance contribution, which peaks at approximately $7.5 \times 10^{-5} [\text{W}/(\text{cm}^2 \cdot \text{sr} \cdot \mu\text{m})]$ in each angular region from ozone in the 8.5-12- μm waveband. The spectral radiance at 90 degrees (black line), which also represents skyshine, has a similar spectral profile as the 0- and 45-degree profiles

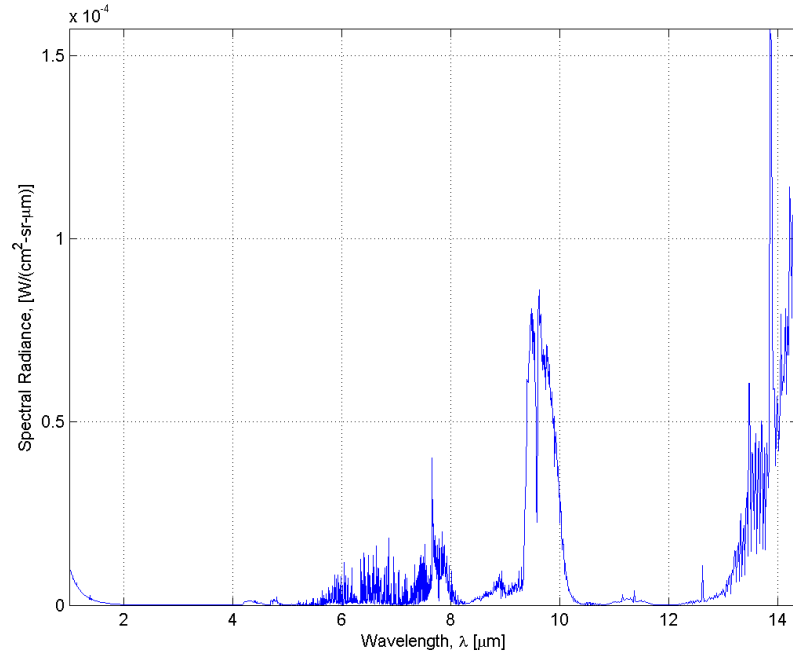


Figure 4.3: Spectral radiance incident onto target body seen at the specular angle, 28.4 degrees from zenith, with a path from the target to infinity.

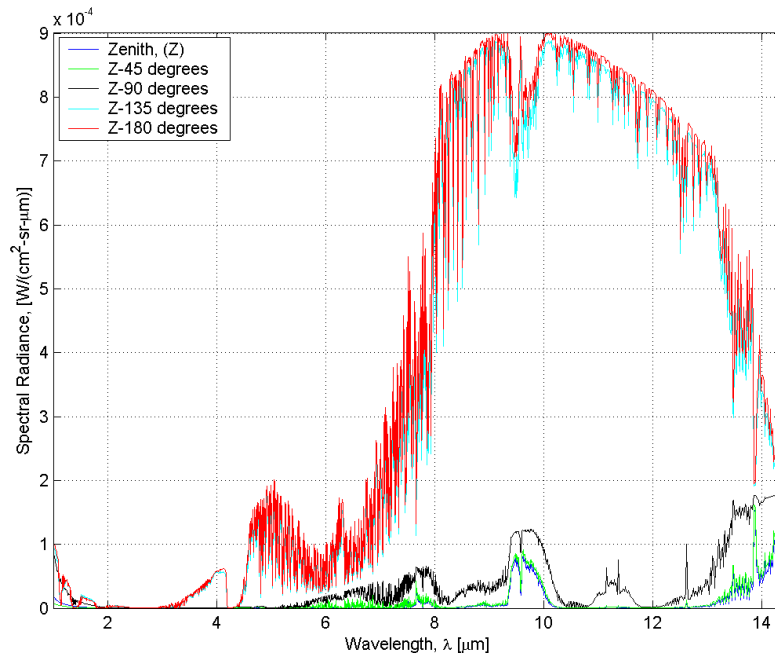


Figure 4.4: Spectral radiances incident onto target body used to compute the diffuse reflected background as seen from angles 0, 45, 90, 135, and 180 degrees from zenith, with a path from the target to infinity.

with the main difference being the 90-degree spectral radiance contribution is larger than the other two. This result makes sense because the longest path through the atmosphere occurs at this 90-degree angle, which looks out to the horizon. The spectral radiances at 135 (cyan line) and 180 (red line) degrees are significantly different than the others because this spectral radiances represent earthshine. These earthshine components are the main contributors to the diffuse reflected background. The 3.4-4.2- μm waveband experiences a peak spectral radiance contribution of approximately $6 \times 10^{-5} [W/(cm^2 \cdot sr \cdot \mu m)]$ in both angular regions; the 8.5-12- μm waveband experiences a large peak spectral radiance contribution of approximately $9 \times 10^{-4} [W/(cm^2 \cdot sr \cdot \mu m)]$ in both angular regions. To get a usable quantity for the simulation, each of these spectral radiances are inputs to equation (3.24), which produces an irradiance incident on the target body:

$$E_{e,bkgdf}(\lambda) = 0.23L_{e,0}(\lambda) + 1.11L_{e,45}(\lambda) + 0.46L_{e,90}(\lambda) + 1.11L_{e,135}(\lambda) + 0.23L_{e,180}(\lambda). \quad (4.1)$$

The result from equation (4.1) is shown in Figure 4.5 and is used in computing the diffuse-reflected component in the simulation.

With the above scenario-dependent spectral inputs defined for this analysis, all the other IR camera simulation parameters can be defined, too. These input parameters are summarized in Table 4.1.

Table 4.1: IR camera simulation inputs with their corresponding units, symbols, and default values.

Parameter Name	Symbol	Units	Spectral Quantity?	Default Value(s)
<i>Engagement Scenario</i>				
Target distance	s_{trg}	m	No	15794
<i>Target Parameters</i>				
Temperature distribution on target	$T(x_{trg}, y_{trg})$	K	No	300 - 800
Target sample size	Δx_{trg}	m	No	5×10^{-3}
Specular reflectivity	$\rho_{spec}(\lambda)$	unitless	Yes	0 - 1
<i>continued on the next page</i>				

Table 4.1: *continued*

Parameter Name	Symbol	Units	Spectral Quantity?	Default Value(s)
Diffuse reflectivity	$\rho_{diff}(\lambda)$	unitless	Yes	0 - 1
Number of sample elements in $T(x_{trg}, y_{trg})$	N	unitless	No	1024
Radius of missile	r_{trg}	m	No	0.5
<i>Atmospheric Parameters</i>				
Observer-to-target atmospheric transmission	$\tau_{atm}(\lambda)$	unitless	Yes	0 - 1
Observer-to-target spectral path radiance	$L_{e,path,trg}(\lambda)$	$\frac{W}{m^2 \cdot sr \cdot m}$	Yes	Scenario dependent
Observer-to-infinity spectral path radiance	$L_{e,path,inf}(\lambda)$	$\frac{W}{m^2 \cdot sr \cdot m}$	Yes	Scenario dependent
Specular angle spectral path radiance	$L_{e,spec}(\lambda)$	$\frac{W}{m^2 \cdot sr \cdot m}$	Yes	Scenario dependent
Diffuse background spectral irradiance	$E_{e,diff}(\lambda)$	$\frac{W}{m^2 \cdot m}$	Yes	Scenario dependent
Atmospheric MTFs	MTF_{atm}	unitless	Yes	0 - 1
<i>Optical System Parameters</i>				
Waveband	λ	m	Yes	$3.4 - 4.2 \times 10^{-6}$ $8.5 - 12 \times 10^{-6}$
Aperture diameter	D_{opt}	m	No	0.6
Obscuration diameter	D_{obsc}	m	No	0.2
Focal length	f	m	No	6
Optical transmission	$\tau_{opt}(\lambda)$	unitless	Yes	0 - 1
Spectral filter transmission	$\tau_{filter}(\lambda)$	unitless	Yes	0 - 0.95
<i>Detector Parameters</i>				
Operating temperature	T_{opr}	K	No	77
Dark current density figure of merit at ambient temperature	D_{FM}	$\frac{A}{m^2}$	No	5×10^{-7}
Ambient environment temperature	T_{amb}	K	No	300
Cutoff wavelength at ambient temperature	$\lambda_{c,amb}$	m	No	InSb: 7×10^{-6} MCT: 7.293×10^{-6}
Resistance-area product	RA	$\Omega - m^2$	No	InSb: 1×10^3 MCT: 1.5×10^{-3}
Cutoff wavelength	λ_c	m	No	InSb: 5.5×10^{-6}
<i>continued on the next page</i>				

Table 4.1: *continued*

Parameter Name	Symbol	Units	Spectral Quantity?	Default Value(s)
				MCT: 13.75×10^{-6}
Index of refraction	n	unitless	Yes	Material dependent
Extinction coefficient	k	unitless	Yes	Material dependent
Detector alignment			No	“det_center” or “edge_cent”
FPA pixel size	w_{det}	m	No	25×10^{-6}
Detector material thickness	l_x	m	No	10×10^{-6}
Integration time	τ	sec	No	0.125×10^{-3} 1×10^{-3}
FPA array size	N_{det}	unitless	No	256
Charge transfer efficiency	CTE	unitless	No	0.99999
Gate capacitance of input MOSFET	C_I	F	No	1×10^{-14}
Gate capacitance of output MOSFET	C_S	F	No	1×10^{-13}
Transconductance of output MOSFET	g_m	mhos	No	5×10^{-4}

The outputs generated by the IR camera simulation are summarized in Table 4.2.

4.2 SNR Data

With all the simulation parameters defined, a parametric study that investigates the expected SNR as four simulation parameters are varied can begin. These four parameters are the target’s specular and diffuse reflectivities, integration time, and the choice of waveband. The waveband choices (3.4-4.2 μm and 8.5-12 μm) were rationalized in terms atmospheric transmission in section 4.1. The chosen values for FPA integration time are 1 msec and 0.125 msec. The former is a common integration time for an FPA based on the several FPA datasheets [8, 11, 22]. The latter is based on the minimum integration time for AFIT’s Santa Barbara InSb FPA [23:10]. The most varied parameters in this study are the specular and diffuse reflectivities, which

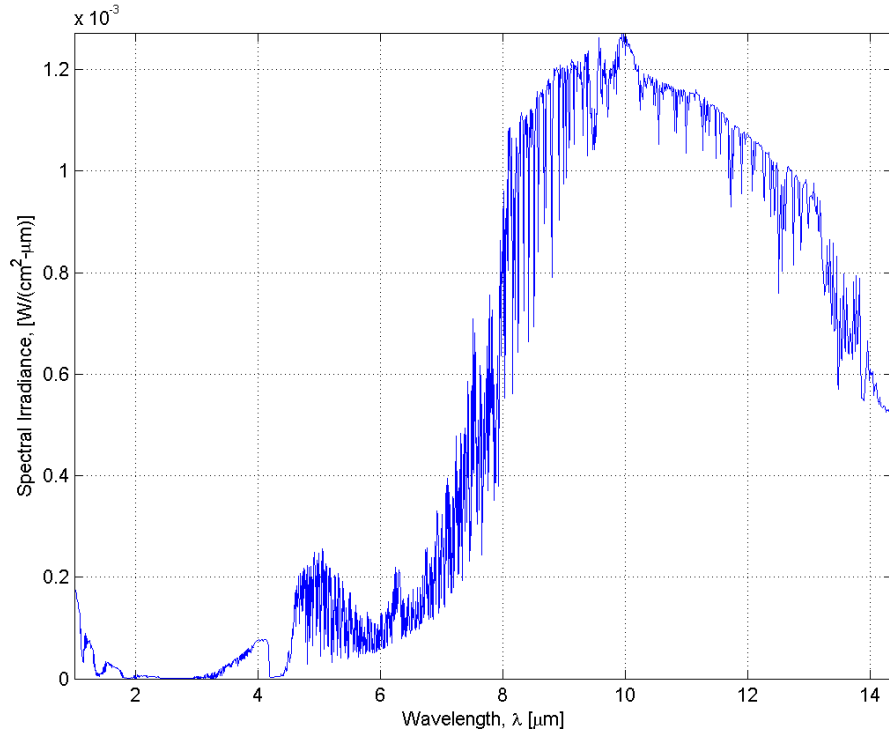


Figure 4.5: Diffuse spectral irradiance incident on the missile body computed from the 0-, 45-, 90-, 135-, and 180-degree spectral radiance contributions.

will range from zero to one and will be changed in steps of 0.1. These reflectivities are coupled and governed by the relation in equation (3.8) which describes the emissivity of the target. The overall objective of this SNR study is to determine how detectable the HEL-induced thermal emission is based on these four parameters and to identify trends in the results.

For this SNR study, 264 simulation runs were required to account for all combinations of the four test variables. The main simulation output used for this study is the variable “SNR” from Table 4.2. This variable presents an image of the target as it would be seen by an FPA with values representing the SNR for each pixel in the FPA. Examples of the SNR variable are shown in Figures 4.6, which shows the expected SNR for the InSb FPA in the 3.4-4.2 μm waveband, and 4.7, which shows

Table 4.2: IR camera simulation outputs with their corresponding units.

Parameter Name	Units
<i>Spectrally Integrated Images</i>	
Radiance from target	$\frac{W}{m^2 \cdot sr}$
Irradiance on FPA	$\frac{W}{m^2}$
Radiant flux on FPA	W
Photon flux on FPA	$\frac{photon}{sec}$
<i>Detector Images (Spatially Integrated)</i>	
Number of electrons	e^-
Irradiance	$\frac{W}{m^2}$
Radiant flux	W
Photon flux	$\frac{photon}{sec}$
Photo-generated current	A
SNR	unitless
<i>Noise Factors</i>	
Photon	e^-
Johnson	e^-
Dark Current	e^-
Transfer	e^-
Fat zero	e^-
kTC	e^-
Preamplifier	e^-

the expected SNR for the MCT FPA in the 8.5-12 μm waveband. In this SNR study, three pixels in Figures 4.6 and 4.7 are of interest:

1. Pixel (129,129) represents the SNR at the hottest part of the HEL-induced temperature distribution. Data associated with this pixel are in Tables 4.3, 4.4, 4.5, and 4.6.
2. Pixel (92,129) represents the SNR at a point along the missile axis not experiencing HEL-induced heating. Data associated with this pixel are in Tables 4.7, 4.8, 4.9, and 4.10.
3. Pixel (92,92) represents the SNR of the background located off of the missile. Data associated with this pixel are in Tables 4.11, 4.12, 4.13, and 4.14.

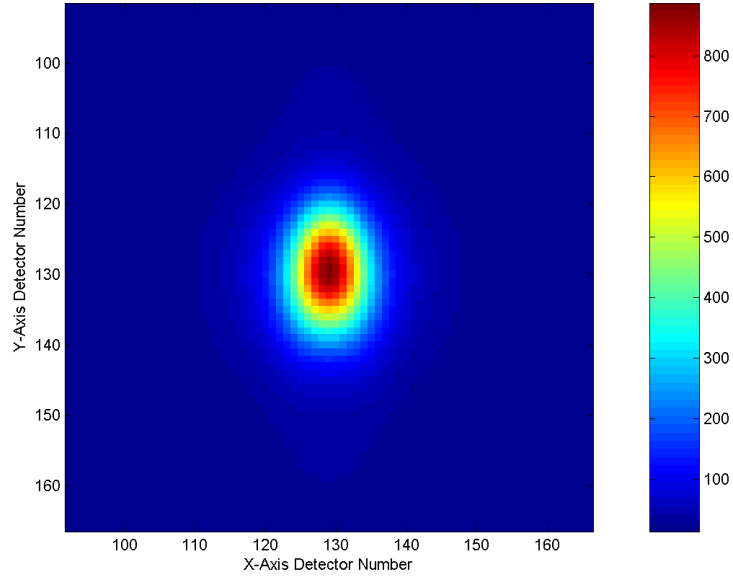


Figure 4.6: Computed SNR from a 256×256 InSb FPA in the $3.4\text{-}4.2\ \mu\text{m}$ waveband: Integration Time: 0.125 msec, $\rho_{spec} = 0.2$, $\rho_{diff} = 0.5$. Optic: $D_{opt} = 0.6\text{ m}$, $F\# = 10$.

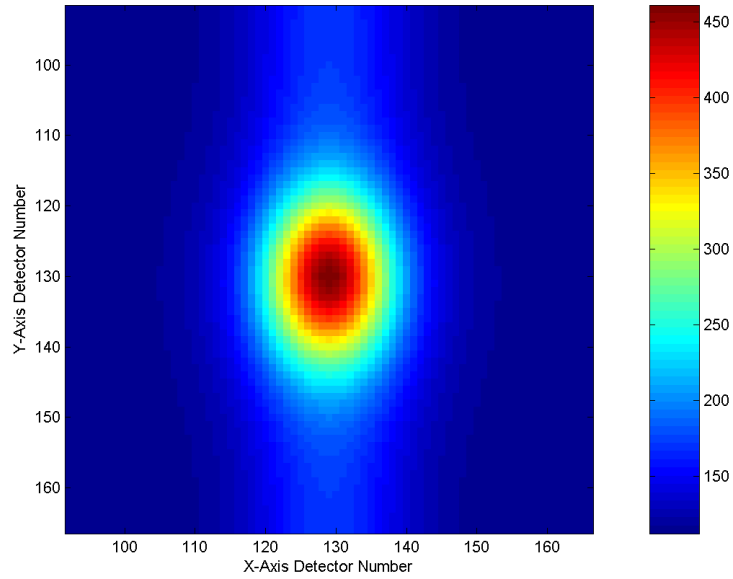


Figure 4.7: Computed SNR from a 256×256 MCT FPA in the $8.5\text{-}12\ \mu\text{m}$ waveband: Integration Time: 0.125 msec, $\rho_{spec} = 0.2$, $\rho_{diff} = 0.5$. Optic: $D_{opt} = 0.6\text{ m}$, $F\# = 10$.

Table 4.3: Computed SNR for hottest pixel (129,129) using a 256×256 InSb FPA in the $3.4\text{--}4.2 \mu\text{m}$ waveband, Integration Time: 1 msec. Optic: $D_{opt} = 0.6$ m, $F\# = 10$.

		ρ_{spec}										
		0.0	0.1	0.2	0.3	0.4	0.5	0.6	0.7	0.8	0.9	1.0
ρ_{diff}	0.0	3557	3375	3182	2977	2756	2516	2250	1949	1592	1126	67
	0.1	3375	3182	2977	2756	2516	2250	1949	1592	1126	70	
	0.2	3182	2977	2756	2516	2251	1949	1592	1126	72		
	0.3	2977	2756	2516	2251	1949	1592	1127	74			
	0.4	2756	2516	2251	1949	1592	1127	77				
	0.5	2516	2251	1950	1592	1127	79					
	0.6	2251	1950	1592	1127	81						
	0.7	1950	1593	1127	83							
	0.8	1593	1128	85								
	0.9	1128	87									
	1.0	90										

Table 4.4: Computed SNR for hottest pixel (129,129) using a 256×256 InSb FPA in the $3.4\text{--}4.2 \mu\text{m}$ waveband, Integration Time: 0.125 msec. Optic: $D_{opt} = 0.6$ m, $F\# = 10$.

		ρ_{spec}										
		0.0	0.1	0.2	0.3	0.4	0.5	0.6	0.7	0.8	0.9	1.0
ρ_{diff}	0.0	1256	1192	1123	1051	972	887	793	686	559	393	12
	0.1	1192	1123	1051	972	887	793	686	559	393	13	
	0.2	1123	1051	972	887	793	686	559	393	14		
	0.3	1051	972	887	793	686	559	393	14			
	0.4	972	887	793	686	559	394	15				
	0.5	887	793	686	559	394	15					
	0.6	793	686	560	394	16						
	0.7	686	560	394	17							
	0.8	560	394	17								
	0.9	394	18									
	1.0	18										

Table 4.5: Computed SNR for hottest pixel (129,129) using a 256×256 MCT FPA in the 8.5-12 μm waveband, Integration Time: 1 msec. Optic: $D_{opt} = 0.6$ m, $F\# = 10$.

		ρ_{spec}										
		0.0	0.1	0.2	0.3	0.4	0.5	0.6	0.7	0.8	0.9	1.0
ρ_{diff}	0.0	2101	1944	1782	1617	1447	1272	1092	906	715	518	314
	0.1	1952	1790	1625	1455	1280	1101	916	725	528	324	
	0.2	1798	1633	1463	1289	1110	925	734	538	334		
	0.3	1641	1472	1298	1119	934	744	548	344			
	0.4	1480	1306	1128	943	753	557	355				
	0.5	1315	1137	953	763	567	365					
	0.6	1145	962	772	577	375						
	0.7	971	782	587	385							
	0.8	791	596	395								
	0.9	606	405									
	1.0	415										

Table 4.6: Computed SNR for hottest pixel (129,129) using a 256×256 MCT FPA in the 8.5-12 μm waveband, Integration Time: 0.125 msec. Optic: $D_{opt} = 0.6$ m, $F\# = 10$.

		ρ_{spec}										
		0.0	0.1	0.2	0.3	0.4	0.5	0.6	0.7	0.8	0.9	1.0
ρ_{diff}	0.0	743	687	630	571	511	449	386	320	253	183	111
	0.1	690	633	574	514	453	389	324	256	187	115	
	0.2	636	577	517	456	392	327	260	190	118		
	0.3	580	520	459	395	330	263	194	122			
	0.4	523	462	399	333	266	197	125				
	0.5	465	402	337	270	200	129					
	0.6	405	340	273	204	132						
	0.7	343	276	207	136							
	0.8	280	211	140								
	0.9	214	143									
	1.0	147										

Table 4.7: Computed SNR for missile body pixel (92,129) using a 256×256 InSb FPA in the $3.4\text{-}4.2 \mu\text{m}$ waveband, Integration Time: 1 msec. Optic: $D_{opt} = 0.6$ m, $F\# = 10$.

		ρ_{spec}										
		0.0	0.1	0.2	0.3	0.4	0.5	0.6	0.7	0.8	0.9	1.0
ρ_{diff}	0.0	153	147	140	133	125	117	109	100	90	79	67
	0.1	148	141	134	127	119	110	102	92	81	70	
	0.2	142	135	128	120	112	103	94	84	72		
	0.3	137	130	122	114	105	96	86	74			
	0.4	131	123	115	107	98	88	77				
	0.5	125	117	109	100	90	79					
	0.6	119	110	101	92	81						
	0.7	112	103	94	83							
	0.8	105	96	85								
	0.9	97	87									
	1.0	90										

Table 4.8: Computed SNR for missile body pixel (92,129) using a 256×256 InSb FPA in the $3.4\text{-}4.2 \mu\text{m}$ waveband, Integration Time: 0.125 msec. Optic: $D_{opt} = 0.6$ m, $F\# = 10$.

		ρ_{spec}										
		0.0	0.1	0.2	0.3	0.4	0.5	0.6	0.7	0.8	0.9	1.0
ρ_{diff}	0.0	38	36	34	31	29	27	24	21	18	15	12
	0.1	37	34	32	30	27	24	22	19	16	13	
	0.2	35	32	30	28	25	22	20	17	14		
	0.3	33	30	28	25	23	20	17	14			
	0.4	31	29	26	23	21	18	15				
	0.5	29	26	24	21	18	15					
	0.6	27	24	22	19	16						
	0.7	25	22	19	17							
	0.8	23	20	17								
	0.9	21	18									
	1.0	18										

Table 4.9: Computed SNR for missile body pixel (92,129) using a 256×256 MCT FPA in the $8.5\text{-}12\ \mu\text{m}$ waveband, Integration Time: 1 msec. Optic: $D_{opt} = 0.6\text{ m}$, $F\# = 10$.

		ρ_{spec}										
		0.0	0.1	0.2	0.3	0.4	0.5	0.6	0.7	0.8	0.9	1.0
ρ_{diff}	0.0	615	586	556	526	497	467	436	406	375	345	314
	0.1	596	566	536	506	476	446	416	386	355	324	
	0.2	576	546	516	486	456	426	396	365	334		
	0.3	556	526	496	466	436	406	375	344			
	0.4	536	506	476	446	416	385	355				
	0.5	516	486	456	426	395	365					
	0.6	496	466	436	405	375						
	0.7	476	446	415	385							
	0.8	456	425	395								
	0.9	435	405									
	1.0	415										

Table 4.10: Computed SNR for missile body pixel (92,129) using a 256×256 MCT FPA in the $8.5\text{-}12\ \mu\text{m}$ waveband, Integration Time: 0.125 msec. Optic: $D_{opt} = 0.6\text{ m}$, $F\# = 10$.

		ρ_{spec}										
		0.0	0.1	0.2	0.3	0.4	0.5	0.6	0.7	0.8	0.9	1.0
ρ_{diff}	0.0	217	207	197	186	175	165	154	143	133	122	111
	0.1	210	200	190	179	168	158	147	136	125	115	
	0.2	203	193	182	172	161	151	140	129	118		
	0.3	196	186	175	165	154	143	133	122			
	0.4	189	179	168	158	147	136	125				
	0.5	182	172	161	150	140	129					
	0.6	175	165	154	143	132						
	0.7	168	158	147	136							
	0.8	161	150	140								
	0.9	154	143									
	1.0	147										

Table 4.11: Computed SNR for background pixel (92,92) using a 256×256 InSb FPA in the 3.4-4.2 μm waveband, Integration Time: 1 msec. Optic: $D_{opt} = 0.6$ m, $F\# = 10$.

		ρ_{spec}										
		0.0	0.1	0.2	0.3	0.4	0.5	0.6	0.7	0.8	0.9	1.0
ρ_{diff}	0.0	73	73	72	72	71	70	70	69	69	68	67
	0.1	73	72	72	71	70	70	69	69	68	67	
	0.2	72	72	71	70	70	69	69	68	67		
	0.3	72	71	70	70	69	69	68	67			
	0.4	71	70	70	69	69	68	67				
	0.5	70	70	69	69	68	67					
	0.6	70	69	69	68	67						
	0.7	69	69	68	67							
	0.8	69	68	67								
	0.9	68	67									
	1.0	67										

Table 4.12: Computed SNR for background pixel (92,92) using a 256×256 InSb FPA in the 3.4-4.2 μm waveband, Integration Time: 0.125 msec. Optic: $D_{opt} = 0.6$ m, $F\# = 10$.

		ρ_{spec}										
		0.0	0.1	0.2	0.3	0.4	0.5	0.6	0.7	0.8	0.9	1.0
ρ_{diff}	0.0	14	14	14	14	13	13	13	13	13	13	12
	0.1	14	14	14	13	13	13	13	13	13	12	
	0.2	14	14	13	13	13	13	13	13	12		
	0.3	14	13	13	13	13	13	13	12			
	0.4	13	13	13	13	13	13	12				
	0.5	13	13	13	13	13	12					
	0.6	13	13	13	13	12						
	0.7	13	13	13	13							
	0.8	13	13	13								
	0.9	13	13									
	1.0	13										

Table 4.13: Computed SNR for background pixel (92,92) using a 256×256 MCT FPA in the 8.5-12 μm waveband, Integration Time: 1 msec. Optic: $D_{opt} = 0.6$ m, $F\# = 10$.

		ρ_{spec}										
		0.0	0.1	0.2	0.3	0.4	0.5	0.6	0.7	0.8	0.9	1.0
ρ_{diff}	0.0	321	320	320	319	318	317	317	316	315	315	314
	0.1	320	320	319	318	318	317	316	316	315	314	
	0.2	320	319	318	318	317	316	316	315	314		
	0.3	319	318	318	317	317	316	315	315			
	0.4	319	318	317	317	316	315	315				
	0.5	318	317	317	316	315	315					
	0.6	318	317	316	316	315						
	0.7	317	316	316	315							
	0.8	317	316	315								
	0.9	316	315									
	1.0	315										

Table 4.14: Computed SNR for background pixel (92,92) using a 256×256 MCT FPA in the 8.5-12 μm waveband, Integration Time: 0.125 msec. Optic: $D_{opt} = 0.6$ m, $F\# = 10$.

		ρ_{spec}										
		0.0	0.1	0.2	0.3	0.4	0.5	0.6	0.7	0.8	0.9	1.0
ρ_{diff}	0.0	113	113	113	113	112	112	112	112	112	111	111
	0.1	113	113	113	112	112	112	112	112	111	111	
	0.2	113	113	113	112	112	112	112	111	111		
	0.3	113	113	112	112	112	112	111	111			
	0.4	113	112	112	112	112	111	111				
	0.5	112	112	112	112	112	111					
	0.6	112	112	112	112	111						
	0.7	112	112	112	111							
	0.8	112	112	111								
	0.9	112	111									
	1.0	112										

4.2.1 SNR Discussion. Starting this SNR discussion with the hot spot SNR data (Tables 4.3, 4.4, 4.5 and 4.6), the IR camera simulation predicts that the measured irradiance is strongly affected by the target's reflectivity, yet the irradiance is

very observable. To quantify this statement, the simulated SNR at the hottest part of the HEL-induced thermal emission in the 3.4-to-4.2- μm with a 0.125-msec integration time produced values ranging from 1256, for the case of a true blackbody, to 394 when the total reflectivity was very high at 0.9. In the 8.5-to-12- μm waveband, similar trends were also experienced with a 743 SNR at zero reflectivity and approximately 200 SNR at 0.9 total reflectivity. When the FPA integration time increased to 1 msec, the SNRs increase significantly for the same spatial location on the target. For the 3.4-to-4.2- μm waveband at zero reflectivity, the SNR is 3557, while at a total reflectivity of 0.9, the SNR is 1127. The 8.5-to-12- μm waveband produces an SNR of 2101 at zero reflectivity and averaged 560 for the 0.9 total reflectivity. These observations are supported by Wien's Displacement Law (equation (2.15)), which computes the peak exitant wavelength associated with the peak hot-spot temperature. For an 800-K blackbody temperature, the peak wavelength result is 3.62 μm , which is within the 3.4-to-4.2- μm waveband; consequently, the spectral radiance in the 8.5-to-12- μm waveband will be lower.

When the total reflectivity was broken into its constituent specular and diffuse components, the SNR varied only slightly in the 3.4-to-4.2- μm waveband with a ΔSNR of 1 at 0.9 total reflectivity. However, the 8.5-to-12- μm waveband is more susceptible to specular and diffuse reflectivity changes. At a total reflectivity of 0.9, the SNR varied from 518 to 606 for a 1-msec integration time. The reason for the variability is due to the larger background radiance seen in the 8.5-to-12- μm waveband of Tables 4.13 and 4.14. Since the diffusely reflected component has a higher spectral radiance than the specularly reflected component, slight increases in the computed SNR occur at constant total reflectance as the diffuse reflectivity becomes more predominant. These subtle results are meeting expectations which indicate the simulation is correct in predicting fundamental trends.

As a note, the presented SNR values are computed with respect to the low noise level at the detector, which explains why the reported SNRs are so large. To get a more realistic perspective in relation to the measured background, the 3.4-to-4.2- μm

waveband hot-spot SNR is above the background SNR, in Tables 4.11 and 4.12, by a factor of 16 in the case of 0.9 total reflectivity. The 8.5-to-12- μm waveband hot-spot SNR is above the background SNR by a factor of 1.9 in the case of 0.9 total reflectivity. Because of these observations, the 3.4-to-4.2- μm waveband is the better choice for measuring irradiances. Further study is required to see if the falloff between $\rho_{tot} = 0.9$ and $\rho_{tot} = 1$ is gradual or abrupt.

Since the simulated hot-spot signals are considerably larger than the detector noise, it would be interesting to see what noise sources are the largest contributors. Table 4.15 provides a summary of all the noise contributions considered in this thesis for both detector materials and integration times. These results are in terms of rms electron counts and came from detecting a target whose reflectivity is $\rho_{spec} = 0.2$ and $\rho_{diff} = 0.3$. For the InSb FPA, the largest noise source is, by far, photon noise. For the MCT FPA, significant noise contributions are from photon and Johnson noises.

Table 4.15: Noise contributions in the InSb and MCT FPAs for integration times of 0.125 msec and 1 msec while observing a target with reflectivities of $\rho_{spec} = 0.2$ and $\rho_{diff} = 0.3$.

	InSb		MCT	
	0.125 msec	1 msec	0.125 msec	1 msec
Photon	$892e^-$	$2523e^-$	$1035e^-$	$2919e^-$
Johnson	$3e^-$	$7e^-$	$2207e^-$	$5875e^-$
Dark Current	$2.4 \times 10^{-4}e^-$	$5.7 \times 10^{-4}e^-$	$0.03e^-$	$0.09e^-$
Transfer	$64e^-$	$181e^-$	$74e^-$	$209e^-$
Fat zero	$20e^-$	$20e^-$	$20e^-$	$20e^-$
kTC	$64e^-$	$64e^-$	$64e^-$	$64e^-$
Preamplifier	$0.1e^-$	$0.3e^-$	$0.1e^-$	$0.3e^-$
Total noise	$897e^-$	2531	$2232e^-$	$6553e^-$

The only SNR results that seem to have some inconsistencies are the background SNR values (Tables 4.11, 4.12, 4.13 and 4.14). As the simulation is currently set up, the entire background is represented by a single path radiance profile. Equation (3.19) does not scale by any reflective or emissive terms. So from a purely radiomet-

ric point of view, these background SNR quantities should remain constant no matter the what diffuse and specular reflectivities are assigned to the target. Further observations show that the SNR values monotonically increase as the target becomes less reflective. The question arises, “What is causing this increase in SNR?” A possible answer was mentioned in section 4.3.2 concerning the differences between the ideal radiometric estimation case and the estimation case using simulation-produced data. The main difference between the two, besides additional radiometric sources, is the optical system; specifically, the diffraction effects inherent to optical systems which produce the Airy disk (Figure 2.4) and the PSF. As Williams and Becklund [24:45] specify, the area underneath a PSF is always one:

$$\int_{-\infty}^{\infty} \int_{-\infty}^{\infty} PSF(x, y) dx dy = 1 \quad (4.2)$$

which means that when a PSF is reduced in height, it must become wider. Causes for wider PSFs, as expressed by the angular size of the Airy disk:

$$\theta_A = \frac{2.44\lambda}{D_{opt}} \quad (4.3)$$

are small apertures and longer wavelengths. The consequence of a wider PSF is a narrower MTF by way of equation (2.30); a narrow MTF reduces the modulation depth more quickly at smaller spatial frequencies. The question might arise as to how this effect changes the SNR values. Since wider PSFs spread out more energy across the image plane, a source emitting more energy will provide the PSF with more energy to distribute. This logic matches the trends in the background SNR tables; more emissive targets had higher background SNRs than less emissive targets.

4.3 Temperature Estimation Via Least Square Optimization

In the process of exercising the capabilities in the IR camera simulation to generate SNRs in the different wavebands, an important realization occurred. By

having two integrated wavebands observing the same spatial region on the target with some temperature distribution, $T(x_{trg}, y_{trg})$, as described in section 3.1.2, a blackbody with an effective temperature for that region, T_{eff} , can be defined. Recalling equations (3.17), (3.19), (3.20), (3.22), (3.25), (3.31) and (3.32), and the discussion in section 3.4.1, a reverse algorithm can be developed using the flux, $\phi_{q,img}$, collected at each pixel, and effectively rewriting equations (3.17), (3.20) and (3.22) as:

$$E'_{e,trg}(\lambda, x_{img}, y_{img}) = \tau_{opt}(\lambda)\tau_{filter}(\lambda)\tau_{atm}(\lambda) \left(\frac{A_{eff}}{s_{img}^2} \right) \varepsilon' L_e(\lambda, T_{eff}) \quad (4.4)$$

$$E'_{e,spec}(\lambda) = \tau_{opt}(\lambda)\tau_{filter}(\lambda)\tau_{atm}(\lambda) \left(\frac{\rho'_{spec}(\lambda)L_{e,spec}(\lambda)}{s_{img}^2} \right) \left[\frac{\pi}{4} (D_{opt}^2 - D_{obs}^2) \right] \quad (4.5)$$

$$E'_{e,diff}(\lambda) = \tau_{opt}(\lambda)\tau_{filter}(\lambda)\tau_{atm}(\lambda) \left(\frac{\rho'_{diff}(\lambda)E_{e,bkgdf}(\lambda)}{\pi s_{img}^2} \right) \left[\frac{\pi}{4} (D_{opt}^2 - D_{obs}^2) \right] \quad (4.6)$$

respectively, where ρ'_{spec} , ρ'_{diff} , and T_{eff} are unknown quantities to be found by least-squares optimization of the best fit of these functions to the $\phi_{q,img}$ value for each waveband. Again, note that $\varepsilon' = 1 - \rho'_{spec} - \rho'_{diff}$. Gauging the desires of DETEC for DIAT, since ABL testers may not have *a priori* knowledge of the missile's emissivity, this initial reverse algorithm, which determines ε' along with T_{eff} , is an appropriate starting point.

4.3.1 Ideal Radiometric Case. To test this algorithm, irradiances from two different wavebands were computed using equation (3.17) at a defined, spatially constant temperature and scaled by a defined emissivity, where ε is of the form of equation (3.8). The values tested were $T_{test} = 567$ K and $\varepsilon = 0.74$. Using equation (4.4), which has the same form as equation (3.17), a least-squares optimization was performed that let the target's temperature and emissivity values be swept independently across a range of values. As a result, the exact values of the temperature and emissivity were extracted: $T_{eff} = 567$ K and $\varepsilon' = 0.74$; consequently, this algorithm works for the ideal radiometric case. Two figures demonstrate where the exact values were met. Figure 4.8 shows the space over which temperature and emissivity were swept. The

location where the two white lines meet indicates where the least-square value is located. Figure 4.9 shows where T_{eff} and ε' were computed in terms of temperature and emissivity independently.

4.3.2 Estimation Using Simulation Data. To apply the same least-squares optimization on actual data from the IR camera simulation is a bit more difficult than the previous case. The measured irradiances include contributions from additional atmospheric sources, the measured irradiance itself comes from many different temperatures that are encompassed by a detector's IFOV, and the signal irradiance is attenuated spectrally by the atmospheric transmission. Another factor that makes the least-squares optimization more difficult for this case is the diffracting effects of the optical system. To perform the least-squares optimization on the IR camera simulation data, three variables that should be swept for each pixel in order to account for the primary contributions include the specular and diffuse reflectivities and the effective temperature.

So as to not get too complicated initially, there might be a reasonable assumption that may allow the sweeping of just two variables: temperature and total reflectivity, which is related to emissivity by equation (3.6). Looking at Figures 4.10 and 4.11, which show the spectral radiance contributions for all modeled sources in both wavebands, the specular background contribution (cyan line) is quite insignificant compared to the other contributions; it ranges from 10 to 1000 times below the magnitude of the diffuse background and path radiance contribution. With the 300-K blackbody (blue line) and the diffuse background being fairly close to each other in magnitude, any change in the diffuse reflectivity should be negated by the opposite response in emissivity of the 300-K blackbody. For higher temperatures, like at 800 K, the self-emission is so large that any change in the diffuse reflectivity will produce only slight changes in the total radiance, which can be seen in the SNR data. For these reasons, use of total reflectivity is justified.

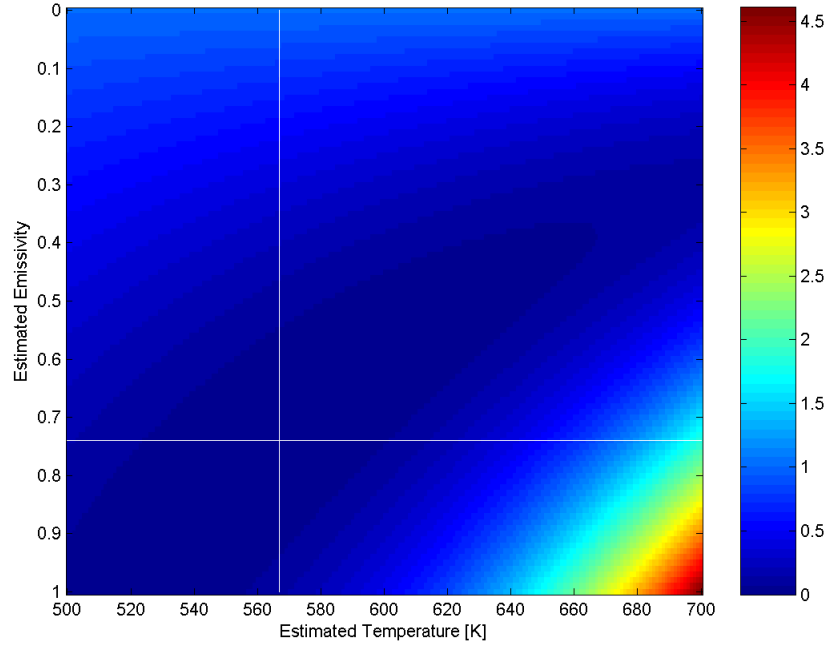


Figure 4.8: Image of estimated variable space showing where the least square is located: $T_{eff} = 567$ K and $\varepsilon' = 0.74$.

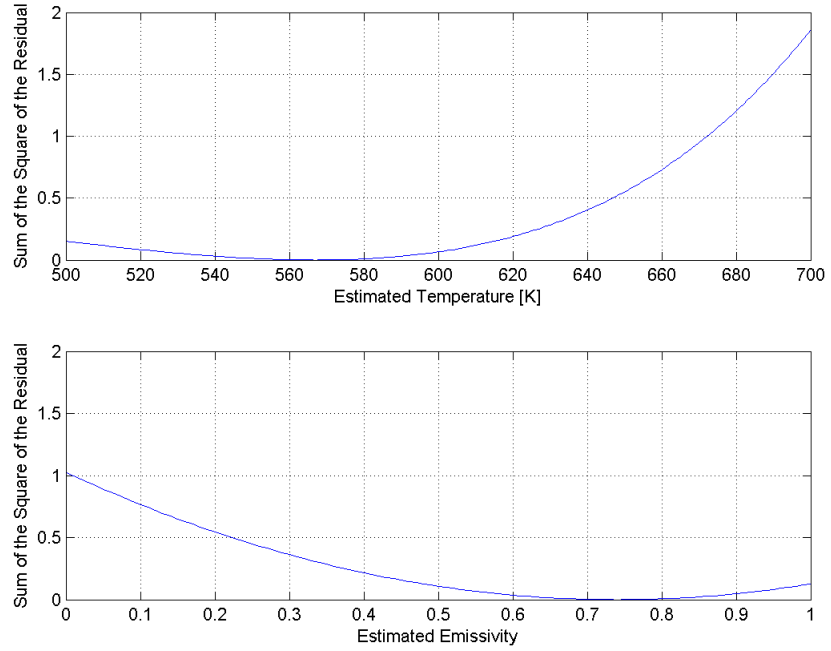


Figure 4.9: Top: How the estimation residual varied with temperature. Bottom: How the estimation residual varied with emissivity.

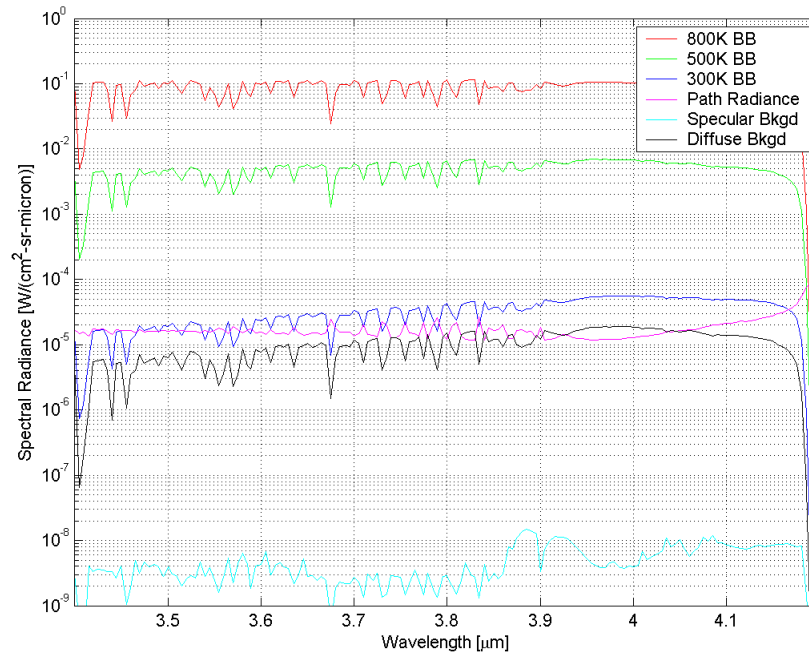


Figure 4.10: Spectral radiance contributions in the 3.4-to-4.2- μm waveband; atmospheric transmission is included..

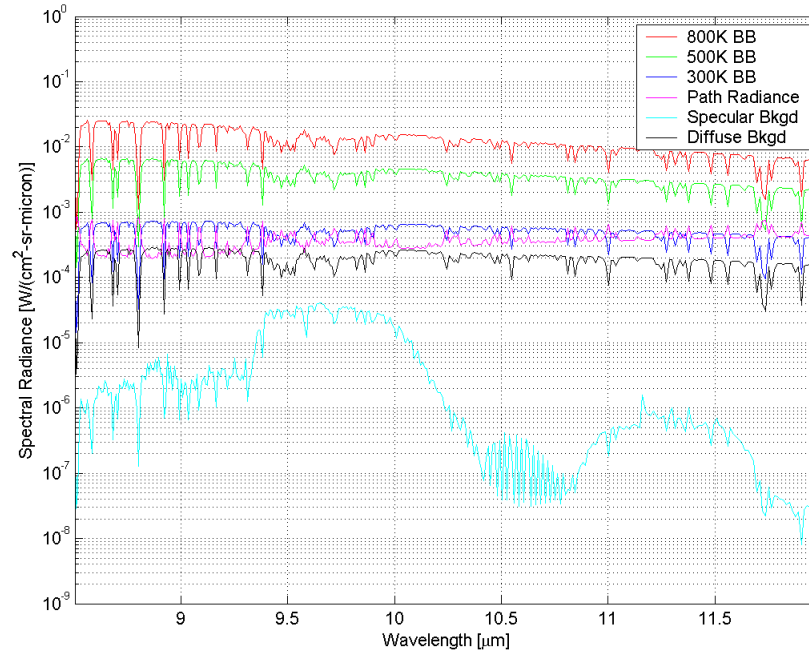


Figure 4.11: Spectral radiance contributions in the 8.5-to-12- μm waveband; atmospheric transmission is included..

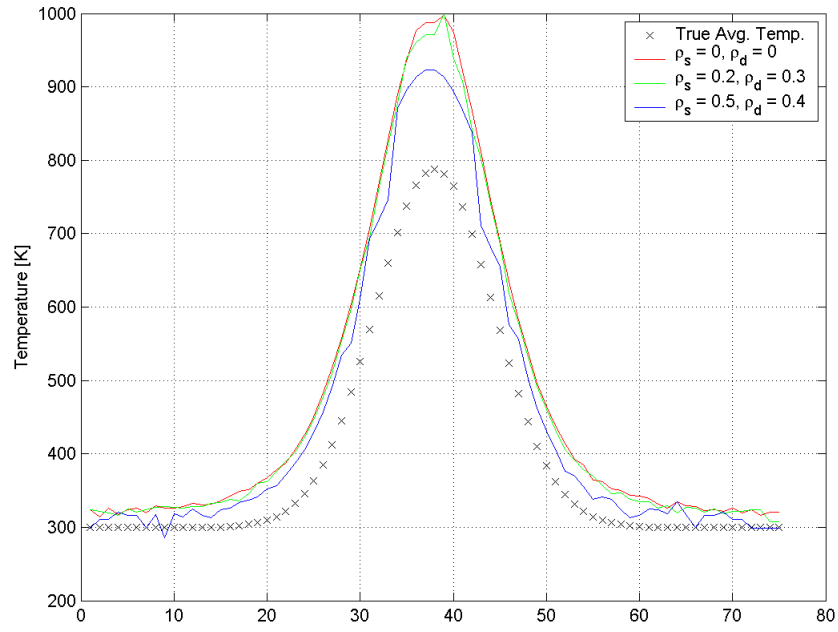


Figure 4.12: Estimated temperature profiles for various specular and diffuse reflectivities along the axis of the missile, 0.125 msec integration time.

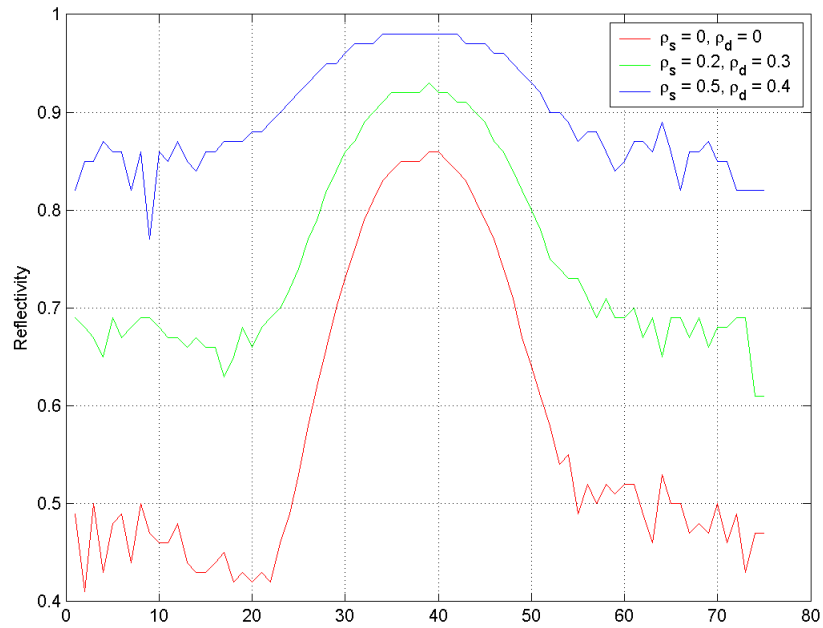


Figure 4.13: Estimated total reflectance profiles for various specular and diffuse reflectivities along the axis of the missile, 0.125 msec integration time.

The first attempt at estimating the effective temperature and total reflectance along the missile axis is shown in Figures 4.12 and 4.13, respectively. Looking at Figure 4.12, something obviously is amiss with the estimating algorithm since it shows a 100- to 200-K overshoot at the peak average temperature of 780 K. Away from the HEL-induced hot spot, where the missile body was set to 300 K, the estimates were improved, but they still showed 20-50 K overshoot. The reflectivity estimates in Figure 4.13 are nowhere near their expected values, especially, for the cases where the total reflectance is zero (red line) and 0.5 (green line). The zero-reflectivity case varies between 0.45 and 0.85. Given that the estimating algorithm gave exact results for the ideal case, and the same algorithm produced such bad results used the simulated data, some quantity has not been fully accounted for between these two cases. So instead of continuing to generate tables of suspect temperature estimates, the remainder of this analysis will be spent discussing why the temperature estimates deviated from the expected value.

4.3.3 Temperature Estimation Discussion. As discussed in section 4.2.1, the optical system may be the reason why the proposed estimation algorithm works poorly. Further analysis is required to determine whether this argument applies to the results of the estimation algorithm. To simplify this analysis, the use of apparent temperature will enable this study to more easily pick out how the least-squares estimation comes to its conclusions. Since temperature is the only variable, the estimate can be done for each band, as well as using both bands. Also, each estimate will incorporate one of the following assumptions in its estimator:

1. The estimator is modeled strictly as an ideal blackbody (*i.e.*, ε is one).
2. The estimator is modeled as case 1 with the additional assumption that the spectral atmospheric transmission function is known.
3. The estimator is modeled as case 2 with the additional assumption that the spectral path radiance from the observer to infinity at the observation angle is a known quantity.

For case 1, using an ideal Planckian as the estimating function in the least-square estimation algorithm results in Figure 4.14. This figure shows the result of the two-band estimation (black, dashed line) on a target whose emissivity is one (*i.e.*, ρ_{spec} is zero and ρ_{diff} is zero), which allows this analysis to be independent of emissivity. The figure shows a significant underestimate in temperature, with a peak apparent temperature of 405 K; however, this result makes perfect sense. Even though this estimation used the simulated, ideal blackbody data, specific radiometric factors like atmospheric transmission and path radiance were not factored into the estimator. As a consequence, the apparent temperature does not have to be large in order to create a Planckian function estimator whose two integrated wavebands equal the results from the simulation. The end result is an underestimation of the temperature. Looking

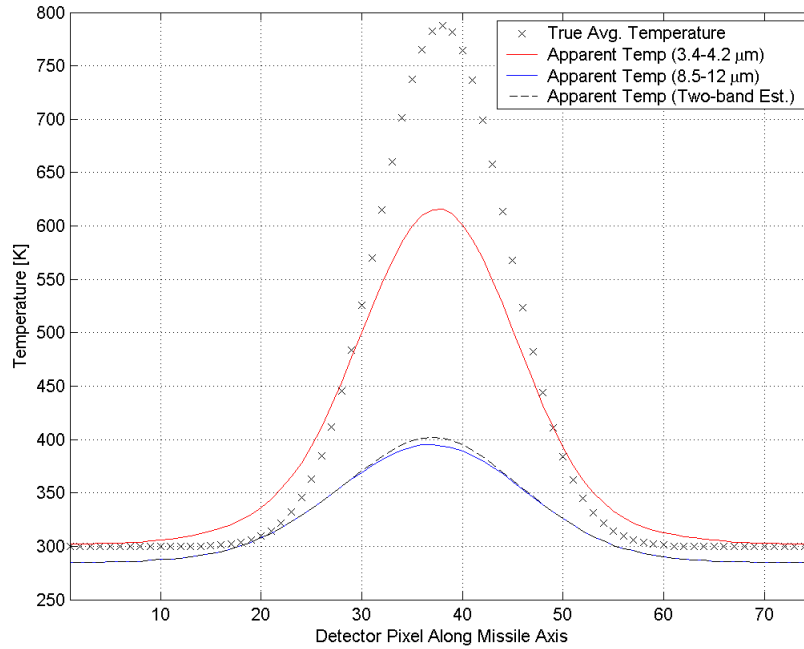


Figure 4.14: Apparent temperatures using an ideal blackbody estimator for the 3.4-4.2- μm band, 8.5-12- μm , and the two-band cases. Simulated source reflectivities: $\rho_{spec} = 0.0$, $\rho_{diff} = 0.0$. Integration time: 0.125 msec.

at the individual bands, the peak apparent temperature estimate in the 3.4-4.2- μm band (red line) is a better estimate at 615 K, while, the peak apparent-temperature

estimate in the 8.5-12- μm band (blue line) is at 395 K. These results makes sense again given the radiometric factors listed above. The atmospheric transmission, shown in Figure 4.1, demonstrates that the transmission is better in the 3.4-4.2- μm band than the 8.5-12- μm band. Also, the spectral path radiance, shown in Figure 4.2, shows that background is much larger in the 8.5-12- μm band than the 3.4-4.2- μm band. The net effect is an underestimation of apparent temperature in both bands, but the 3.4-4.2- μm band provides the better estimate than the 8.5-12- μm band. The only part of the apparent-temperature profiles that do not make sense occurs in the 3.4-4.2- μm -band estimate at the points on the missile body furthest away from the HEL-induced hot spot. This profile shows an overestimate of 305 K. From the above radiometric reasoning, the expected result should be an underestimate. The optical system may be contributing to this result, but all the other estimating cases must be addressed first before any definitive statement are made.

In case 2, the next step is to add an assumption that the state of atmospheric transmission is a known quantity. Multiplying the ideal Planckian estimator function by the spectral atmospheric transmission results in the estimation profiles shown in Figure 4.15. The peak apparent temperatures in the two-band, 3.4-4.2- μm band and 8.5-12- μm band cases are 505 K, 665 K, and 475 K, respectively. These estimates are better than in case 1, and their temperature shifts make sense even though the overall estimates are still off. By including the spectral atmospheric transmission, energy is removed from the vacuum-transmission estimator, which requires a higher apparent temperature. For the missile body temperatures, an interesting phenomenon has occurred; the single band estimates have switched from Figure 4.14, where the 8.5-12- μm band has a larger apparent temperature estimate than the 3.4-4.2- μm band. This observation can be explained. Since atmospheric absorption and the path radiance are so much greater in the 8.5-12- μm band than the 3.4-4.2- μm band, the 8.5-12- μm -band estimator produces a higher apparent temperature than the 3.4-4.2- μm -band estimator. However, this result is counterintuitive when entire temperature profile is considered. The expectation would be both single-band curves maintain their same

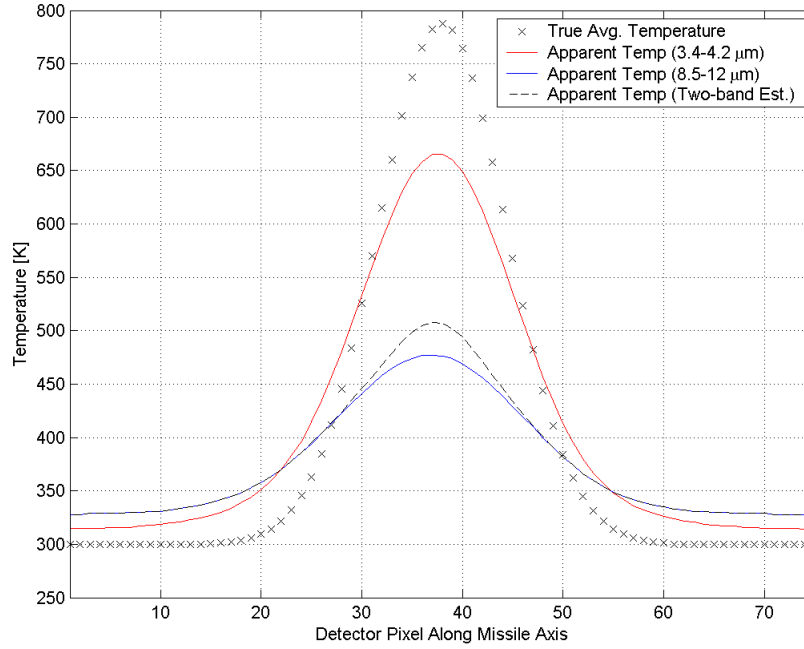


Figure 4.15: Apparent temperatures using an ideal blackbody estimator scaled by the atmospheric transmission function for the 3.4-4.2- μm band, 8.5-12- μm , and the two-band cases. Simulated source reflectivities: $\rho_{spec} = 0.0$, $\rho_{diff} = 0.0$. Integration time: 0.125 msec.

relative positions; they would simply be shifted higher due to the addition of the atmospheric transmission function in the estimator. This result provides some initial evidence that the optical system is redistributing energy onto the FPA, but there is still one more factor that needs to be considered: the path radiance.

For the last case, the remaining assumption that can be made is that the path radiance is a known quantity. Conceivably, this quantity could be measured by having the camera look at a region of sky where the missile will fly through the camera's FOV, but in order for the measurement to be valid, the camera can no longer move as this measurement only applies to that specific part of the atmosphere. An uncertainty analysis with respect to the possible variance in path radiance may be in order here. When the path radiance of this "measurement" is added to the case 2 blackbody estimator, the apparent-temperature estimation results for the two-band and each

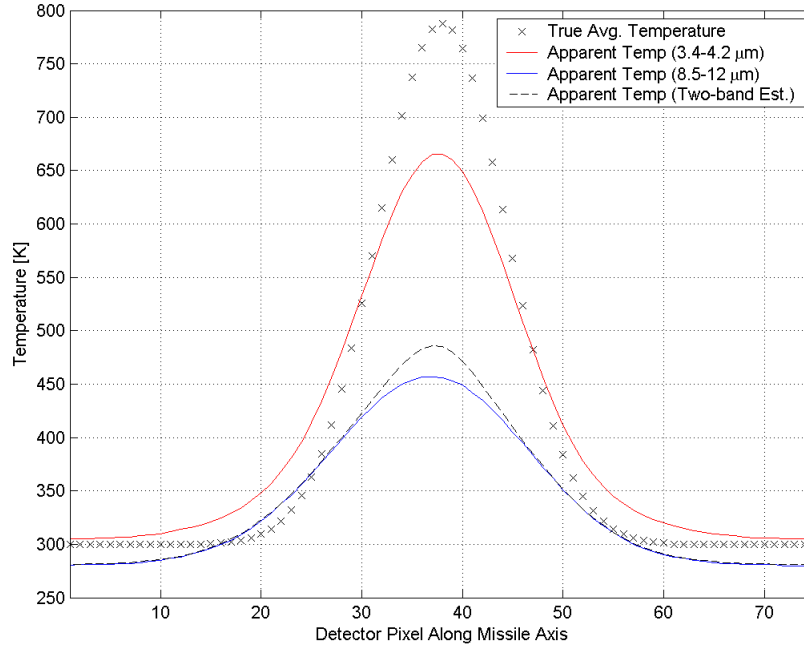


Figure 4.16: Apparent temperatures using an ideal blackbody estimator scaled by the atmospheric transmission function and incorporating path radiance for the 3.4-4.2- μm band, 8.5-12- μm , and the two-band cases. Simulated source reflectivities: $\rho_{spec} = 0.0$, $\rho_{diff} = 0.0$. Integration time: 0.125 msec.

single band case is shown in Figure 4.16. The peak apparent temperatures in the two-band, 3.4-4.2- μm band and 8.5-12- μm band cases changed slightly from case 2 and are 490 K, 660 K, and 455 K, respectively. The missile body apparent temperatures returned to similar values like in case 1, and no “switching” of the missile body temperatures were observed like in case 2. As a result, the differences between the peak and missile body temperatures are at their greatest extent. Out of the three cases analyzed, case 3 represents the best case to estimate temperature because it takes into account the two radiometric effects, besides self-emission, that affect the measured signal. Since this analysis uses the zero-reflectivity simulation data, specular- and diffuse-reflected radiances shown in Figures 4.10 and 4.11 are not factors affecting these estimations. From this case, the main question to be asked is, “What is causing these apparent temperature estimates to be significantly underestimated?”

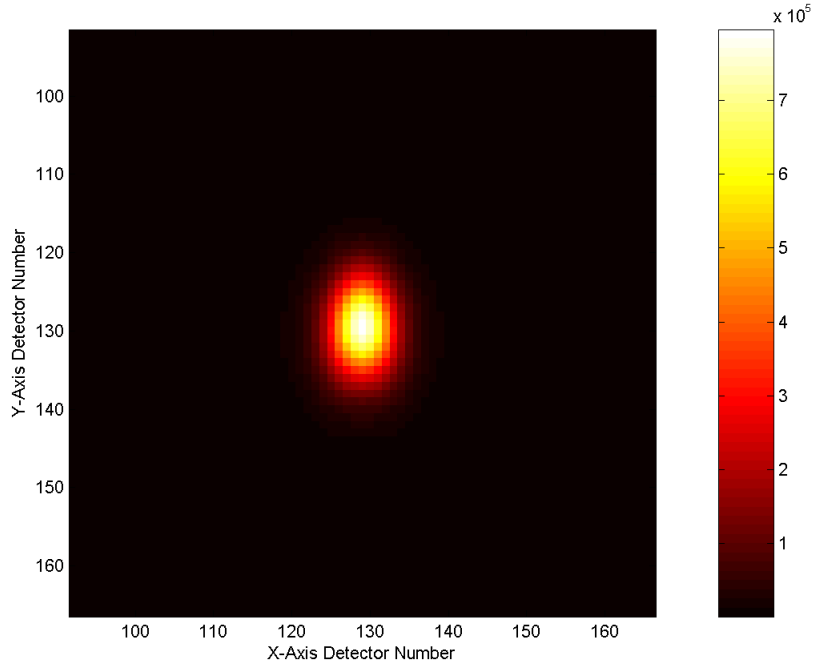


Figure 4.17: Photon flux incident on the InSb FPA in the 3.4-to-4.2- μm waveband, 0.125-msec integration time. Simulated source reflectivities: $\rho_{spec} = 0.2$, $\rho_{diff} = 0.3$.

Incorporating the discussion from section 4.2.1 that the PSF is an energy distribution device with the analysis results from the above three cases, a definitive conclusion can be made about the temperature estimates: the PSF is the cause of the inaccurate temperature estimates. To create an image like what is shown in Figures 3.12 and 4.17, requires by equation (2.31) that the optical system's PSF be convolved with the incoming scene irradiance. In that process, energy is redistributed across the whole image. This effect can be observed in Figures 4.14, 4.15 and 4.16. For the case of the 8.5-12- μm band apparent temperature, part of the irradiance that comes from spatial regions associated with the missile body is distributed to spatial regions associated with the background, which would explain why the missile body apparent temperature for the blackbody target in Figure 4.16 is underestimated. The same observation applies to the spatial region associated with HEL-induced hot spot, which is by far the most significant energy source in the image; the PSF will redis-

tribute a larger portion of its energy across the whole image as was indicated by the background SNR results. With the larger energy portion removed, the apparent temperature estimates of the hottest pixel have the largest errors of any measurement on any given temperature profile as seen in Figures 4.14, 4.15 and 4.16. Given that the estimates for the 8.5-12- μm band were worse than the 3.4-4.2- μm band, there is an inherent wavelength dependence in the amount of error in the apparent temperature estimates. As seen in Figure 4.16, 3.4-4.2- μm band estimates are better than the 8.5-12- μm band estimates simply because the PSF in the 3.4-4.2- μm band narrower. This assertion makes intuitive sense when equation (4.3) is considered. The angular size of the PSF is smaller for shorter wavelengths than for longer wavelengths.

To improve the temperature estimates, as approached in this thesis, the PSF should be designed such that it is as narrow as possible. This effect can be achieved by incorporating adaptive optic systems which will reduce the widening effects of the atmosphere on the PSF. To demonstrate how much an effect the modeled atmosphere had on the generated data, see Figures 4.18, 4.19 and 4.20. The only way that the least-squares temperature estimating algorithm will provide accurate estimates is if all factors associated with generating the imaging data are precisely accounted. Assuming the PSF is optimized as much as possible, the temperature estimates will still be off given that the PSF can never become a delta function (*i.e.*, an infinitely large aperture). The only way to fully counteract the effects of the PSF would be to deconvolve it with the collected image. This action would then retrieve the perfect image, which would provide more suitable conditions for the least-squares method to work.

Because Figures 4.12 and 4.13 were the starting points of this entire discussion, additional discussion is required to explain their results since the PSF is now known to be the main source of uncertainty in the temperature estimation. The question that must be answered in this discussion is, “Why were the temperature and reflectivity estimates so inaccurate in this two-band, two-dimensional least-squares optimization?” The object of the least-squares optimization is to find the tempera-

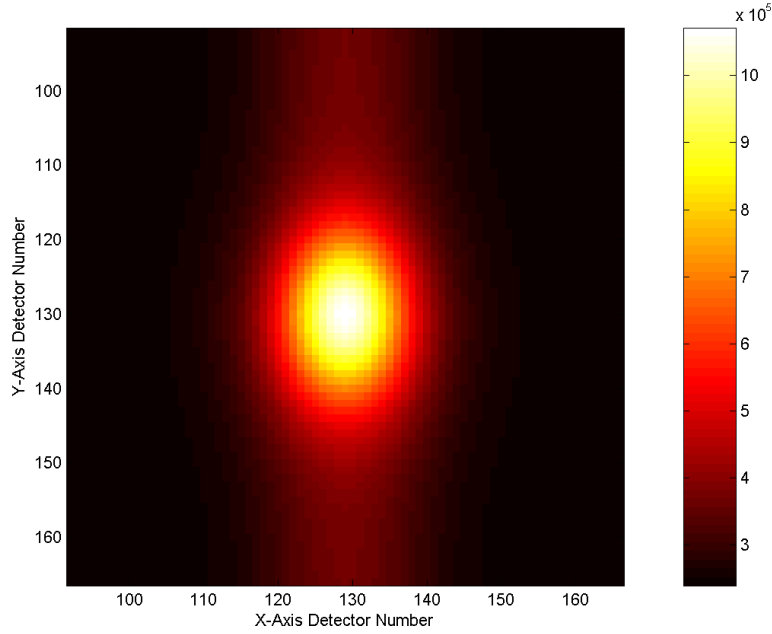


Figure 4.18: Number of electrons generated (atmospheric MTF included) in the MCT FPA in the 8.5-to-12- μm waveband, 0.125-msec integration time. Simulated source reflectivities: $\rho_{spec} = 0.2$, $\rho_{diff} = 0.3$.

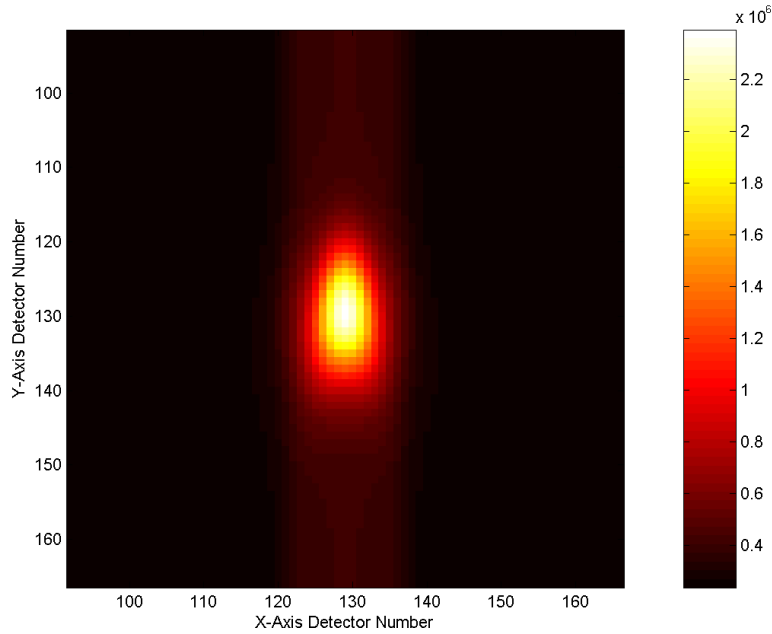


Figure 4.19: Number of electrons generated (atmospheric MTF not included) in the MCT FPA in the 8.5-to-12- μm waveband, 0.125 msec integration time. Simulated source reflectivities: $\rho_{spec} = 0.2$, $\rho_{diff} = 0.3$.

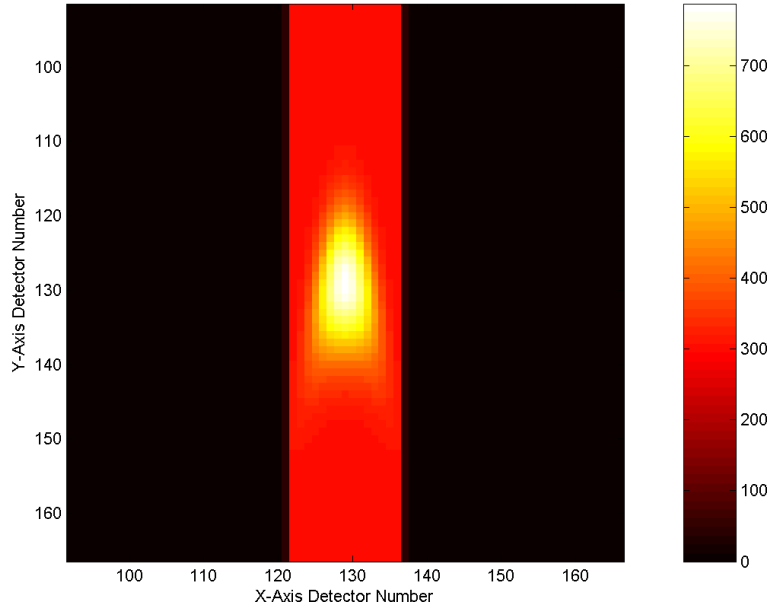


Figure 4.20: Ideal image of temperature distribution which shows the average temperature within each projected pixel of the FPA.

ture and reflectivity values that best match the two-band simulated values using a single Planckian estimating function. Focusing on the zero reflectivity case (red line), Figure 4.12 shows a consistent overestimate over the entire temperature profile, and Figure 4.13 shows an significant overestimate of the target's reflectivity. From the above apparent-temperature discussions, the PSFs consistently cause the apparent temperature estimates to underestimate, and the estimates was worse at longer wavelengths. Since the irradiance of the hottest pixel was smaller, due to the PSF, than in the ideal case, the least-squares optimization was selecting higher reflectivities and temperature estimates in order to minimize the sum of the squares of the differences.

4.4 Summary

In this chapter, the IR camera simulation went from just being a model to a tool that can provide technical answers to aid DIAT development. The SNR data generated in this chapter can be used to gauge the expected signal from the HEL-

induced hotspot. The attempt at estimating temperature will give DIAT developers insight as to what factors need to be considered for that estimate. These impacts will be discussed more thoroughly in the next chapter.

V. Conclusions and Recommendations

With the analysis complete, some definitive conclusions can be presented that will help guide DIAT's development. In Chapter I, this thesis asked a series of fundamental questions about the scenario of verifying the ABL's performance when it lases targets; those questions now have answers. Along the way in finding answers to those questions, many other questions arose, which provided other avenues of research. Those different avenues will be discussed, as well.

5.1 *Major Contributions*

The IR camera simulation provided a major contribution to the development of DIAT by answering the following questions:

1. How will the target's reflectivity affect the measured irradiance?
2. What kind of SNRs can be expected for different target reflectivity values?
3. What waveband is the best choice for the irradiance measurement?
4. Can the laser hot-spot temperatures be estimated?
5. What factors contribute to the estimated temperature's uncertainty?

Questions 1, 2, and 3 need to be addressed jointly because their answers are very coupled. The results of the SNR analysis showed that the target's reflectivity has a significant impact on the measured irradiance, which was indicated by the variation in simulated SNR values for different reflectivities. The data showed that the SNRs are very dependent on the choice of waveband, with the 3.4-4.2- μm waveband providing the best SNRs from very emissive to very reflective targets. The 8.5-12- μm waveband provided strong SNRs, as well, but the background radiance contributions are much more significant in that waveband than the 3.4-4.2- μm waveband, which may cause detection problems for reflective targets. Since this thesis looked at a temperature distribution that had a maximum temperature of 800 K, the best observing waveband is 3.4-4.2 μm .

For Question 4, the answer is, “Not by the estimator used in this thesis!” While this thesis was able to estimate temperature and emissivity for an ideal radiometric case, the temperature estimates became very poor when the least-squares algorithm started to use IR-camera-simulation data. The main difference between these two cases is the incorporation of the optical system and its abilities to redistribute the collected energy over the focal plane. More research is required in order to find ways that correct for the optical system’s effects on truly remote temperature measurement with imaging devices. Which leads to the answer for Question 5, the greatest factor contributing to the estimated temperature uncertainty using the method applied here is the optical system’s PSF.

5.2 Recommendations for Future Research

Given the level of generality that has been designed into the IR camera simulation, the amount of future research possibilities is quite immense. Of first importance, a future research project should be conducted in order to validate the IR camera simulation. An excellent experimental setup would involve the use of an IR scene projector. The advantage of such a setup would be not only to test and validate the radiometric equations, but also to test the ability of the imaging side of the simulation by generating scenes with varying spatial frequencies. An experiment of this type should be able to quantify how much error is induced by an optical system in radiometric measurements.

A second area of continued research should be more extensive parametric studies for the DIAT program. Given the amount of parameters that can be varied for the IR camera simulation, an intensive sensitivity study should begin to identify which parameters in the model are the most susceptible to changes. A study that would be of interest is to identify which other wavebands are the good choices to provide a temperature estimate. Seeing the amount of background radiance that existed in the 8.5-to-12- μm waveband in this thesis provides impetus to explore how well temperature estimation might be made if the background was not so strong. Based

on the spectra seen in the initial estimation attempt, two wavebands in the 3-to-5- μm region may be good choices because the background radiances were so low. All these efforts would certainly aid in the development of a temperature-estimating algorithm.

A third area of continued research, which would again aid the DIAT program, would be to investigate the possibilities, requirements, and methods for deconvolving PSFs from images. Because this factor was the single greatest uncertainty in estimating temperature in this thesis, understanding how to counteract its effects on irradiance measurements would be very beneficial.

Another potential area of future study would be to combine AFIT's Large Commercial Aircraft Infrared (LCAIR) signature modeling software with the IR camera simulation. The benefits of such a simulation would be to expand LCAIR's capabilities by taking into account sensor performance of a modeled sensor system like a tracking pod or a missile seeker, and to incorporate target geometries other than just a single cylinder into the DIAT simulation.

One final area of future research that the IR camera simulation enables is the study of other photon detector materials. Since this simulation uses complex index-of-refraction data to quantify detector performance, measurements of potential detector material's complex index of refraction could be conducted. Based on that data, their performance as a detector could then be evaluated for different scenarios and optical radiation sources.

5.3 Conclusion

In developing this IR camera simulation, a useful tool has been created to aid the development of DIAT and any other projects that require extensive use of IR imaging systems. The tool is a very general model which attempts to encapsulate the critical parameters that define such systems in order to provide realistic results. It is because of this model that this thesis was able to identify the PSF's effects on

irradiance measurements and its impacts in remotely estimating temperature from a target.

Appendix A. Lambertian Source/Fractional Specularity Justification

In Chapter III, section 3.2.1, two assumptions were made concerning the missile body:

1. It could be modeled as a Lambertian radiator.
2. Its emissivity can be modeled using a fractional specularity model.

While these assumptions certainly simplify the radiometry of the problem, they were not chosen at the expense of simulation fidelity. For the engagement scenario specified in this thesis, these assumptions are valid. This appendix provides the necessary justifications and reasoning to validate these assumptions.

The first step toward validation is to begin with the Sandford-Robertson reflectance model [21]. To start, the directional emissivity provides a method for defining the directional and spectral dependence of emissivity. It is defined by [21:18]:

$$\varepsilon(\lambda, \theta) = \varepsilon(\lambda) \frac{g(b, \theta)}{G(b)} \quad (\text{A.1})$$

where $g(b, \theta)$ is the angular distribution, which is a function of elevation angle, θ and grazing angle reflectivity, b and $G(b)$ is a normalization constant for the angular distribution. Expressions for $g(b, \theta)$ and $G(b)$ are defined by [21:18]:

$$g(b, \theta) = \frac{1}{1 + b^2 \tan^2 \theta} \quad (\text{A.2})$$

$$G(b) = \frac{1}{1 - b^2} \left[1 - \frac{b^2 \log(b^2)}{1 - b^2} \right] \quad (\text{A.3})$$

The quantity b , which ranges from zero to one, is an empirical constant determined from surface reflectance data. $g(b, \theta)$ takes emissivity to zero as θ approaches 90 degrees.

To show how these two quantities interact, Figure A.1 plots equation (A.1) to show how the directional emissivity changes with reflectance angle, where $\theta = \theta_r$ and varies from zero to $\frac{\pi}{2}$, and b , which varies from zero to one. As is shown, the directional emissivity can vary significantly depending upon θ_r and b . The important

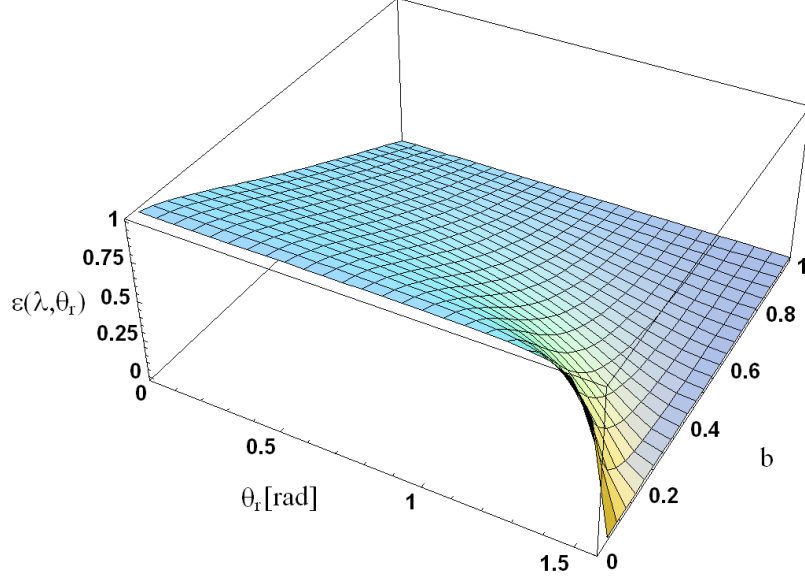


Figure A.1: Directional emissivity for an ideal blackbody (*i.e.*, $\varepsilon(\lambda) = 1$) with θ_r varying from zero to $\frac{\pi}{2}$ and b varying from zero to one.

trend to notice is how directional emissivity varies over θ_r for a given b . Observe that as b decreases from one, the directional emissivity becomes more constant across the θ_r -range with increasingly quick transitions from near the hemispherical emissivity, $\varepsilon(\lambda)$, to zero. For the case that b equals zero, the directional emissivity remains constant for the entire range of θ_r , but right at 90 degrees, the directional emissivity is zero. When this special case occurs, the surface can be defined as a Lambertian radiator; consequently, it will emit equally in all directions.

From the discussion in section 2.1.3.1 about Kirchhoff's law, the total directional reflectivity, which includes specular and diffuse reflectivities, is defined by [21:19]:

$$f_r(\lambda, \theta_i, \phi_i) = \rho_{spec}(\lambda, \theta_i) + \rho_{diff}(\lambda, \theta_i) = 1 - \varepsilon(\lambda, \theta_i) \quad (\text{A.4})$$

where θ_i is the incident elevation angle and ϕ_i is the incident azimuthal angle, which is usually set to zero as a reference. Figure A.2 shows how the total reflectivity varies with the incoming radiation's incident angle for three values of b .

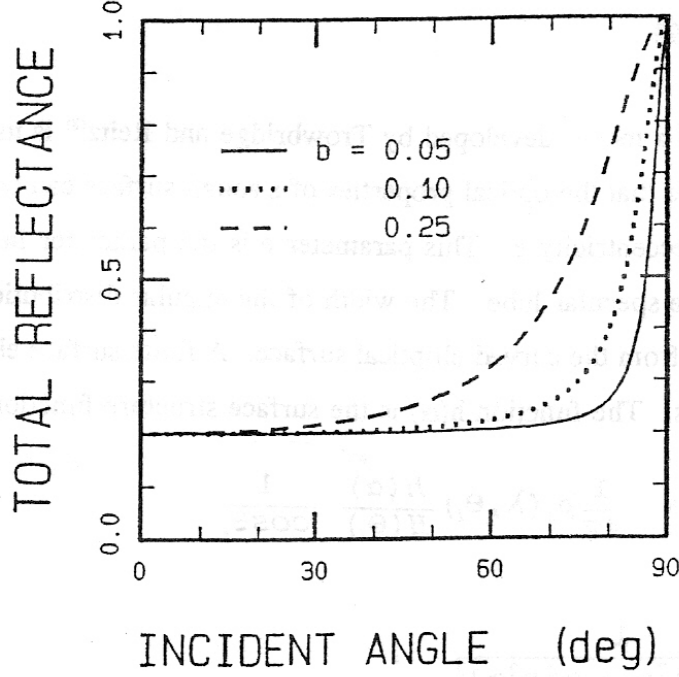


Figure A.2: Angular dependence of the total reflectance for three values of b [21:19].

Focusing on the diffuse component, Sandford and Robertson state that the diffuse reflectivity is assumed to be an average property of the surface that is dependent on microscopic surface roughness and θ_i [21:19]. To consider how the diffuse reflectivity varies with θ_i and b , Sandford and Robertson's diffuse BRDF is used [21:20]:

$$f_d(e, b, \rho_{diff}(\lambda); \theta_i, \phi_i; \theta_r, \phi_r) = \frac{g(\theta_r) \rho_{diff}(\lambda) g(\theta_i)}{\pi [G(b)^2]} \quad (\text{A.5})$$

where the amount of diffusely scattered energy is defined by $\rho_{diff}(\lambda)g(\theta_i)$, and the angular distribution of that radiation is determined by $g(\theta_r)$. For a case when $b \approx 0$ (*i.e.*, Lambertian), Figure A.3 shows that diffuse reflectivity is fairly uniform over a wide range of incident and reflected angles, but when the incident angles are grazing, the diffuse reflectivity decreases while the specular component increases. To clarify what this quantity is in Figure A.3, the question should be asked: Is the diffuse BRDF integrated across the entire range of reflection angles, (θ_r, ϕ_r) , equal to the diffuse

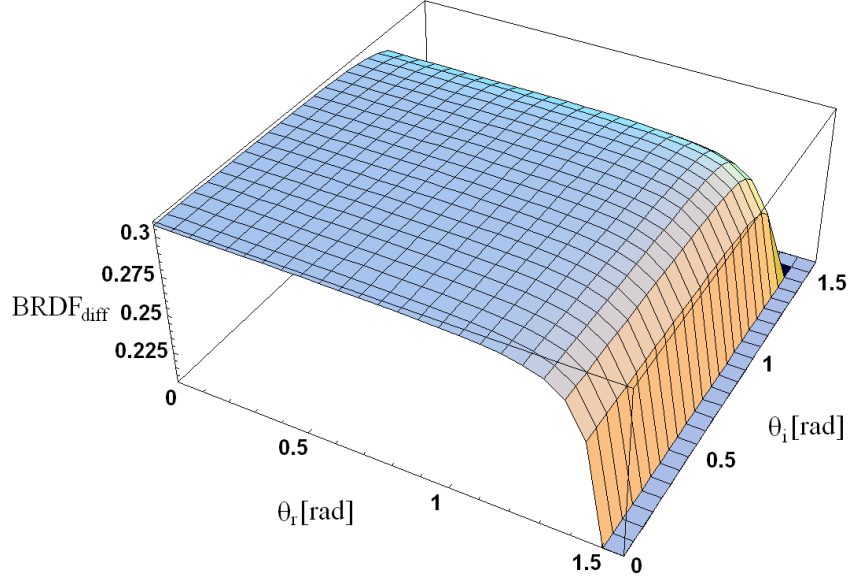


Figure A.3: Diffuse BRDF as a function of incident elevation angle, θ_i , and reflected elevation angle, θ_r , for $b = 0.05$ and $\rho_{diff}(\lambda) = 1$.

reflectivity (*i.e.*, $\int_0^{2\pi} \int_0^{\frac{\pi}{2}} f_d(\theta_i, \phi_i; \theta_r, \phi_r) \cos \theta_r \sin \theta_r d\theta_r d\phi_r = \rho_{diff}(\lambda)$)? The answer is no; this integration represents the diffuse reflectivity as a function of incident elevation angle, θ_i . (*i.e.*, $\rho_{diff}(\lambda, \theta_i)$) as shown in Figure A.4. As b increases, the trend is that the diffuse reflectivity is less uniform over all angles and becomes more directional.

Next, Sanford and Robertson's specular reflectance model requires defining three unit vectors in relation to the reflecting surface: the source, \hat{s} , the observer, \hat{o} ,

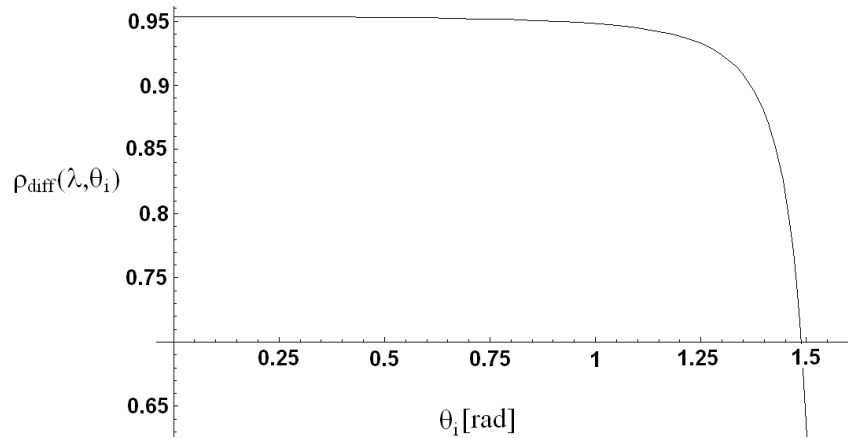


Figure A.4: Diffuse reflectivity as a function of incident elevation angle, θ_i .

and the glint, \hat{g} . They are defined as [21:5]:

$$\hat{s}(\theta_i, \phi_i) = \sin \theta_i \cos \phi_i \hat{x} + \sin \theta_i \sin \phi_i \hat{y} + \cos \theta_i \hat{z} \quad (\text{A.6})$$

$$\hat{o}(\theta_r, \phi_r) = \sin \theta_r \cos \phi_r \hat{x} + \sin \theta_r \sin \phi_r \hat{y} + \cos \theta_r \hat{z} \quad (\text{A.7})$$

$$\hat{g}(\theta_i, \phi_i; \theta_r, \phi_r) = \frac{\hat{o}(\theta_r, \phi_r) + \hat{s}(\theta_i, \phi_i)}{\sqrt{2(1 + \hat{o}(\theta_r, \phi_r) \cdot \hat{s}(\theta_i, \phi_i))}} \quad (\text{A.8})$$

where all vectors are defined in Cartesian coordinates, and \hat{g} defines the unit vector that bisects the angle between \hat{s} and \hat{o} . With \hat{g} computed, the angle, β , which is defined between \hat{g} and the surface normal vector, \hat{n} , can be determined from [21:6]:

$$\beta(\theta_i, \phi_i; \theta_r, \phi_r) = \arccos[\hat{g}(\theta_i, \phi_i; \theta_r, \phi_r) \cdot \hat{n}]. \quad (\text{A.9})$$

When $\beta = 0$, the specular reflection is at a maximum. With β defined, the specular BRDF is modeled by [21:20]:

$$f_s(e, b, \varepsilon(\lambda), \rho_{diff}(\lambda); \theta_i, \phi_i; \theta_r, \phi_r) = \frac{1}{4\pi} \rho_{spec}(\lambda, \theta_i) \frac{h(e, \beta)}{H(e, \theta_i)} \frac{1}{\cos \theta_i} \quad (\text{A.10})$$

where e is the eccentricity of a circular ellipsoid that describes the angular width of the specular lobe, $\rho_{spec}(\lambda, \theta_i)$ is the directional specular reflectivity specified by [21:20]:

$$\rho_{spec}(\lambda, \theta_i) = 1 - \rho_{diff}(\lambda, \theta_i) - \varepsilon(\lambda, \theta_i), \quad (\text{A.11})$$

$h(e, \beta)$ is surface structure function defined by [21:20]:

$$h(e, \beta) = \frac{1}{(e^2 \cos^2 \beta + \sin^2 \beta)^2}, \quad (\text{A.12})$$

and $H(e, \theta_i)$ is a normalization factor defined by [21:21]:

$$H(e, \theta_i) = \frac{1}{2e^2} \left[(1 - e^2) \cos \theta_i + \frac{2e^2 + (1 - e^2)^2 \cos^2 \theta_i}{\sqrt{(1 - e^2)^2 \cos^2 \theta_i + 4e^2}} \right]. \quad (\text{A.13})$$

As the specular BRDF is currently defined, a divergence exists as θ_r approaches 90 degrees; therefore, a cutoff factor must be applied to $f_s(\theta_i, \phi_i; \theta_r, \phi_r)$ to make the energy in the specular lobe [21:22]:

$$d(b, \theta_r) = \frac{1}{1 + b^2 \tan^2 \theta_r}. \quad (\text{A.14})$$

The total BRDF that describes a surface is then the sum of the diffuse and specular components:

$$f_r(e, b, \varepsilon(\lambda), \rho_{diff}(\lambda); \theta_i, \phi_i; \theta_r, \phi_r) = f_d + f_s \times d(b, \theta_r) \quad (\text{A.15})$$

Using the total BRDF as defined, values for $\varepsilon(\lambda)$, $\rho_{diff}(\lambda)$, b , and e can be entered to provide a realistic representation of a surface's reflectivity. Incorporating the Sandford-Robertson parameters that Bortle measured in the mid-wave IR for bare aluminum [3:69], the resulting total BRDF is shown in Figures A.5 and A.6 where $\varepsilon(\lambda) = 0.11$, $\rho_{diff}(\lambda) = 0.02$, $b = 0.05$, and $e = 0.0042$. Figure A.5 shows the BRDF in a Cartesian plot as a function of θ_r and ϕ_r , while Figure A.6 shows the same result, but the BRDF is plotted using spherical coordinates. Both plots demonstrate that this material is very specular given the the strength of the specular lobe. Also, the flatness of the Cartesian plot and the spherical shape of the spherical plot away from the specular lobe shows that the BRDF, at those points, is very nearly perfectly diffuse (*i.e.*, Lambertian), and total BRDF can be described well by a fractional specularity model.

Now, the question is whether the specular lobe is visible to the observer at the observation angle. To answer this, the total BRDF at the appropriate observation angle is plotted as a function of position across the cylindrical missile body, as shown in Figure A.7. Figure A.7 shows that the total BRDF stays reasonably constant across the central 90% of the missile body with a mean value of 6.07×10^{-3} . As expected, the BRDF becomes strongly specular at the grazing angles associated with

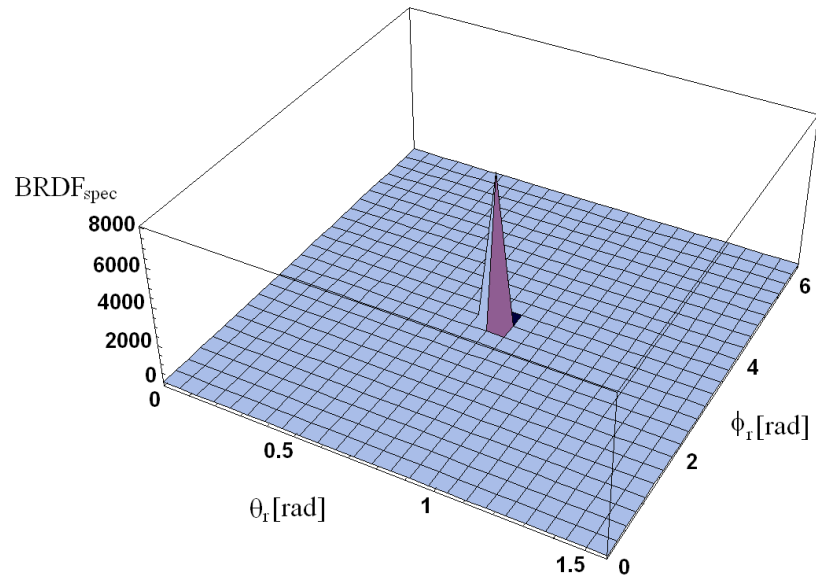


Figure A.5: Total BRDF of bare Al on a Cartesian plot. Sandford-Robertson parameters: $\varepsilon(\lambda) = 0.11$, $\rho_{diff}(\lambda) = 0.02$, $b = 0.05$, and $e = 0.0042$.

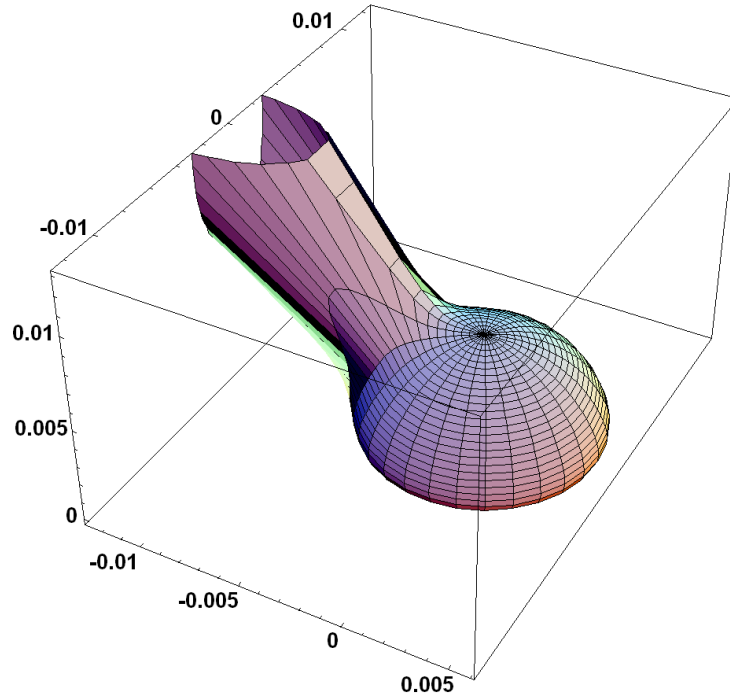


Figure A.6: Total BRDF of bare Al on a spherical plot. Sandford-Robertson parameters: $\varepsilon(\lambda) = 0.11$, $\rho_{diff}(\lambda) = 0.02$, $b = 0.05$, and $e = 0.0042$.

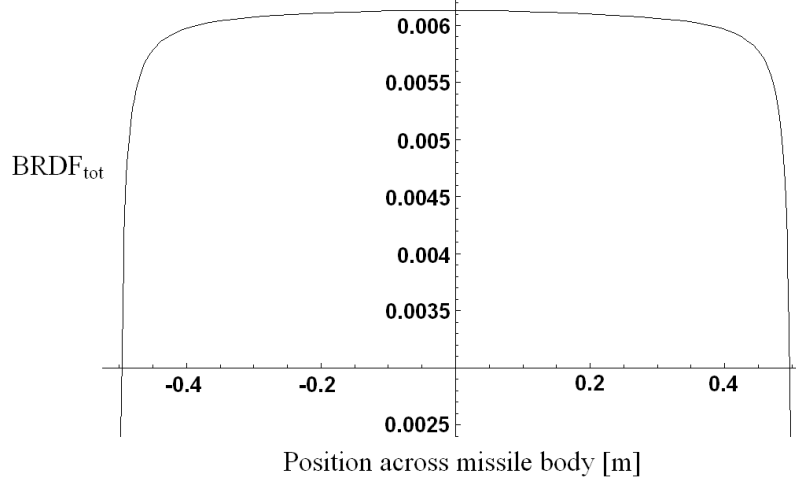


Figure A.7: Total BRDF of bare Al as a function of position on missile body at the 61.6-degree observation angle. Missile body radius is 0.5 m. Sandford-Robertson parameters: $\varepsilon(\lambda) = 0.11$, $\rho_{diff}(\lambda) = 0.02$, $b = 0.05$, and $e = 0.0042$.

the missile's edges, so the BRDF in the direction of the observer drops significantly. These observations indicate that the DETEC scenario is within the diffuse part of the BRDF and away from the specular lobe.

With the diffuse-reflection assumption justified, one more question needs to be answered: How does the directional emissivity, specular reflectivity, and diffuse reflectivity change with position across the missile body? This question is answered by computing the directional emissivity and reflectivities using equations (A.1) and (A.11). As previously defined for bare aluminum, $\varepsilon(\lambda) = 0.11$ and $\rho_{diff}(\lambda) = 0.02$, Figure A.8 shows how the directional emissivity as a function of position across the missile body. Figures A.9 and A.10 show the total diffuse and specular reflectivity as a function of position across the missile body, respectively. All three figures show their respective quantities being very constant across the missile body with the exception occurring at the missile body edges where grazing incident effects dominate. Computing the percent difference in directional emissivity with respect to the directional emissivity at the center position of the missile, the emissivity varies less than 1% across the central 90% of the missile body.

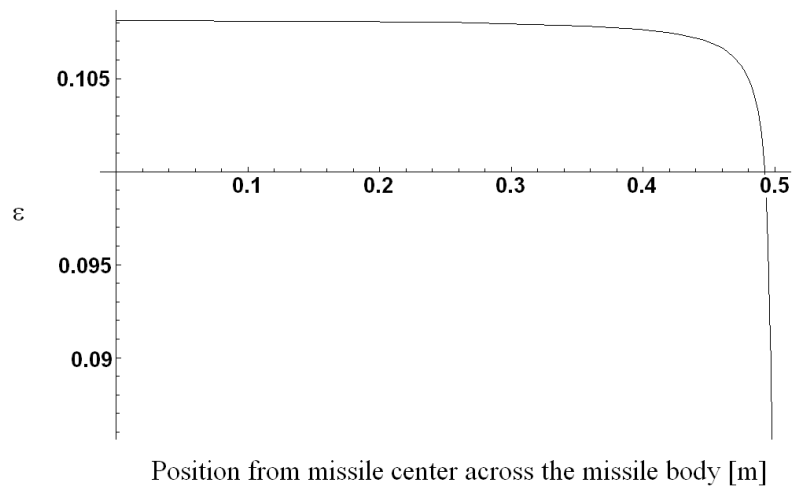


Figure A.8: Directional emissivity as a function of position on the missile body for bare Al.

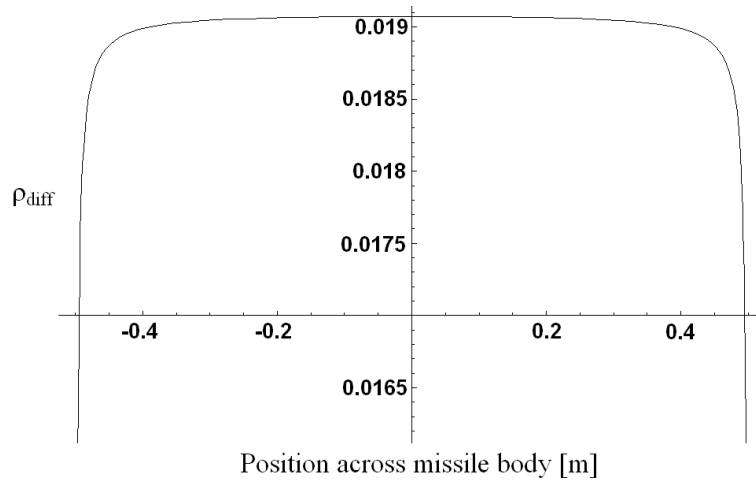


Figure A.9: Directional diffuse reflectivity as a function of position on the missile body for bare Al.

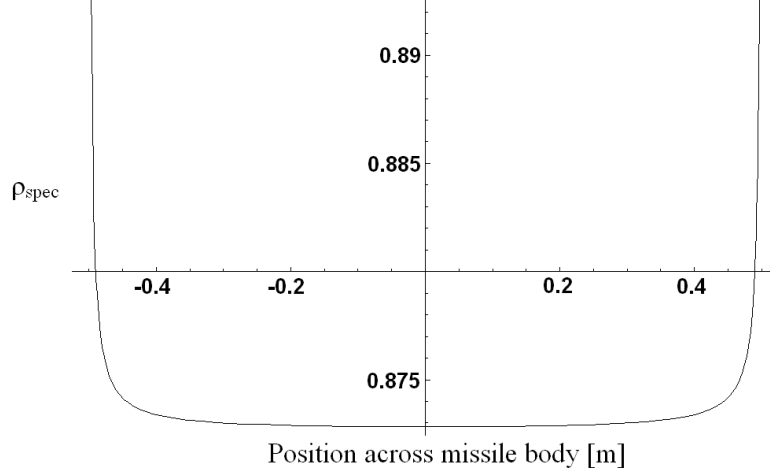


Figure A.10: Directional specular reflectivity as a function of position on the missile body for bare Al.

The same analysis performed on a different surface treatment like gloss white paint, which has a high emissivity and is still specular, yields similar results. The Sandford-Robertson parameters used for this case are $\varepsilon(\lambda) = 0.88$ and $\rho_{diff}(\lambda) = 0.05$, $b = 0.08$, and $e = 0.012$. At the observation angle, the total BRDF is again diffuse, and the directional emissivity varies less than 1% across the central 80% of the missile body.

From this analysis, the following conclusions can be made:

- The missile can be modeled as a Lambertian radiator because the BRDF is clearly diffuse at the 61.6-degree observation angle.
- The deviation from Lambertian occurs at the grazing-incidence angles where use of a Lambertian model could result in an over prediction of the emitted radiation. However, since the projected area of the surface elements at these angles is significantly reduced, it is anticipated that this overprediction will be quite small.
- Fractional specularity is a valid method for modeling the emissivity and specular and diffuse reflectivities for the types of surfaces and observation angles antici-

pated in the DETEC scenario since they stay very constant across a significant portion of the missile body.

Bibliography

1. “Zinc Selenide, Optical Properties”. <http://www.matweb.com/search/SpecificMaterial.asp?bassnum=DSEN71>, 1996-2007. From MatWeb.com, an online material property datasheet source. Accessed website on May 2, 2007.
2. Boreman, Glenn D. *Modulation Transfer Function in Optical and Electro-Optical Systems*. SPIE Press, Bellingham, WA, 2001.
3. Bortle, Jonathan. *A Measurement- and Prediction-Based Validation of the AFIT Large Commercial Aircraft Infrared Trend Analysis Tool*. Master’s thesis, Graduate School of Engineering, Air Force Institute of Technology (AETC), Wright-Patterson AFB OH, March 2006. AFIT/GE/ENP/06-01.
4. Cusumano, Salvatore J. “Delivered Irradiance Assessment Tool: Fiscal Year 2006 End of Year Project Review”, December 2006. Power Point presentation given to DETEC.
5. Dereniak, Eustance L. and Glenn D. Boreman. *Infrared Detectors and Systems*. John Wiley & Sons, Inc., New York, NY, 1996.
6. Driggers, Ronald G., Paul Cox, and Timothy Edwards. *Introduction to Infrared and Electro-Optical Systems*. Artech House, Inc., Norwood, MA, 1999.
7. DRS Infrared Technologies, LP, P.O. Box 740188, Dallas, TX 75374. *DRS’s 480 x 640 Infrared Focal Plane Array (IRFPA) Module*. From datasheet downloaded from <http://www.drs.com>.
8. FLIR Systems, Inc./Indigo Operations, 70 Castilian Dr., Goleta CA 93117. *Mid-wave IR Components: Focal Plane Arrays and Detector Dewar Cooler Assemblies*, 2004. From datasheet downloaded from <http://www.corebyindigo.com>.
9. Goda, Matthew. “OENG 699 Course Notes”, March 2006. From Air Force Institute of Technology independent study course titled “Wave Optics”.
10. Goodman, Joseph W. *Introduction to Fourier Optics*. Roberts & Company Publishers, Greenwood Village, CO, third edition, 2005.
11. IRCAM GmbH, Nürnberger Straße 71, D-91052 Erlangen, Germany. *TAU-RUS 327k SM Pro*, December 2005. From datasheet downloaded from <http://www.ircam.de>.
12. Janesick, James R. *Scientific Charge-Coupled Devices*. SPIE Press, Bellingham, WA, 2001.
13. Klein, Claude A., Bernard diBenedetto, and James Pappis. “ZnS, ZnSe, and ZnS/ZnSe Windows: Their Impact on FLIR System Performance”. *Optical Engineering*, 25(4):519–531, April 1986.

14. L3 Communications/Cincinnati Electronics, 7500 Innovation Way, Mason, Ohio 45040. *NightConqueror II Sensor Modules System Brochure*, September 2005. From datasheet downloaded from <http://www.L-3Com.com/CE>.
15. Lilevjen, Katherine B. *Radiometric Analysis of Daytime Satellite Detection*. Master's thesis, Graduate School of Engineering, Air Force Institute of Technology (AETC), Wright-Patterson AFB OH, March 2006. AFIT/GAP/ENP/06-09.
16. Marciniak, Michael A. "OENG 650 Course Notes", March 2006. From Air Force Institute of Technology course titled "Optical Radiometry and Detection".
17. Marciniak, Michael A. "OENG 780 Course Notes", March 2007. From Air Force Institute of Technology course titled "Infrared Technology".
18. Palik, Edward D. (editor). *Handbook of Optical Constants of Solids*. Academic Press, Inc., Orlando, FL, 1985.
19. Palik, Edward D. (editor). *Handbook of Optical Constants of Solids II*. Academic Press, Inc., San Diego, CA, 1991.
20. Rogalski, A. and K. Chrzanowski. "Infrared Device and Techniques". *Opto-Electronics Review*, 10(2):111–136, 2002.
21. Sandford, Brian P. and David C. Robertson. *Infrared Reflectance Properties of Aircraft Paints*. Technical report ESC-94-1004, Phillips Laboratory, Geophysics Directorate/GPOA, 29 Randolph Rd., Hanscom AFB, MA 01731-3010, August 1994.
22. Santa Barbara Focalplane, 346 Bollay Dr., Goleta, CA 93117. *The SBF Focal Plane Array Family*. From datasheet downloaded from <http://www.sbfpc.com>.
23. Santa Barbara Focalplane, 346 Bollay Dr., Goleta, CA 93117. *WinIR3 Operations Manual*, revision 3.6.0.5 edition, September 2003. From integration time values listed in the "Video Setup" dialog box with the software.
24. Williams, Charles S. and Orville A. Becklund. *Introduction to the Optical Transfer Function*. SPIE Press, Bellingham, WA, 2002.

REPORT DOCUMENTATION PAGE					<i>Form Approved</i> OMB No. 0704-0188	
The public reporting burden for this collection of information is estimated to average 1 hour per response, including the time for reviewing instructions, searching existing data sources, gathering and maintaining the data needed, and completing and reviewing the collection of information. Send comments regarding this burden estimate or any other aspect of this collection of information, including suggestions for reducing this burden to Department of Defense, Washington Headquarters Services, Directorate for Information Operations and Reports (0704-0188), 1215 Jefferson Davis Highway, Suite 1204, Arlington, VA 22202-4302. Respondents should be aware that notwithstanding any other provision of law, no person shall be subject to any penalty for failing to comply with a collection of information if it does not display a currently valid OMB control number. PLEASE DO NOT RETURN YOUR FORM TO THE ABOVE ADDRESS.						
1. REPORT DATE (DD-MM-YYYY) 14-06-2007		2. REPORT TYPE Master's Thesis			3. DATES COVERED (From — To) Jun 2006-Jun 2007	
4. TITLE AND SUBTITLE <div style="text-align: center;">An Infrared Camera Simulation for Estimating Spatial Temperature Profiles and Signal-to-Noise Ratios of an Airborne Laser-Illuminated Target</div>					5a. CONTRACT NUMBER 5b. GRANT NUMBER 5c. PROGRAM ELEMENT NUMBER 	
6. AUTHOR(S) Orth, David F., GS-12					5d. PROJECT NUMBER 07-273 5e. TASK NUMBER 5f. WORK UNIT NUMBER 	
7. PERFORMING ORGANIZATION NAME(S) AND ADDRESS(ES) Air Force Institute of Technology Graduate School of Engineering and Management (AFIT/EN) 2950 Hobson Way Wright-Patterson AFB, OH 45433-7765					8. PERFORMING ORGANIZATION REPORT NUMBER AFIT/GEO/ENP/07-01	
9. SPONSORING / MONITORING AGENCY NAME(S) AND ADDRESS(ES) Directed Energy Test and Evaluation Capability Larry McKee, Ph.D 6200 Uptown Blvd. NE, Suite 300 Albuquerque, NM 87110 Phone: (505) 830-7442					10. SPONSOR/MONITOR'S ACRONYM(S) 11. SPONSOR/MONITOR'S REPORT NUMBER(S) 	
12. DISTRIBUTION / AVAILABILITY STATEMENT APPROVAL FOR PUBLIC RELEASE; DISTRIBUTION UNLIMITED.						
13. SUPPLEMENTARY NOTES 						
14. ABSTRACT Airborne Laser testing and evaluation can be aided by developing a spectrally-based infrared camera simulation to explore how the target surface's specular and diffuse reflectivities affect the observed signal-to-noise ratio (SNR) and how the target's temperature in the laser spot can be estimated. This simulation provides for the observed irradiance, scaled by atmospheric absorption, to consist of the target's self-emission, reflected background emission, and the path emission from the observer to the target. The observed irradiance is scaled and distributed onto a focal plane array by way of a simulated optical system, whose effects are described by modulation transfer functions. The modeled detector response converts the observed irradiance to a current signal from which detector noise quantities are computed. Analyzing the simulated data shows that the observed SNR is dependent upon the target's reflectivity, and leads to a conclusion that the mid-wave infrared band is best choice for observing the thermal emission. For estimating temperature, a least-squares optimization will not work because of the effects of the point spread function.						
15. SUBJECT TERMS Infrared images, radiometry, computerized simulation, temperature measuring instruments, laser weapons						
16. SECURITY CLASSIFICATION OF:			17. LIMITATION OF ABSTRACT		18. NUMBER OF PAGES	
a. REPORT	b. ABSTRACT	c. THIS PAGE	UU		129	
U	U	U	19a. NAME OF RESPONSIBLE PERSON Dr. Michael A. Marciniak, (AFIT/ENP)			
				19b. TELEPHONE NUMBER (include area code) (937) 255-3636, ext 4529; michael.marciniak@afit.edu		